Title
Assessing seasonal snowpack distribution and snow storage over High Mountain Asia

Author
Liu, Yufei

Publication Date
2022

Peer reviewed|Thesis/dissertation

UNIVERSITY OF CALIFORNIA

Los Angeles

Assessing seasonal snowpack distribution and snow storage over High Mountain Asia

A dissertation submitted

in partial satisfaction of the requirements

for the degree Doctor of Philosophy

in Civil Engineering

by

Yufei Liu

2022

ABSTRACT OF THE DISSERTATION

Assessing seasonal snowpack distribution
and snow storage over High Mountain Asia

by

Yufei Liu
Doctor of Philosophy in Civil Engineering
University of California, Los Angeles, 2022
Professor Steven A. Margulis, Chair

Seasonal snowpack is a vital water resource that impacts downstream water availability. However, accurately estimating snow storage and characterizing its spatiotemporal distribution remain challenging, in particular for data-scarce regions such as High Mountain Asia (HMA). In this dissertation, a newly developed snow reanalysis method is used to estimate snow water equivalent (SWE) over the HMA region, assessing its spatiotemporal distribution and quantifying the regional snow storage. The method assimilates fractional snow-covered area (fSCA) from the Landsat and MODIS platforms, over the joint Landsat-MODIS record (Water Year (WY) 2000 – 2017). A fine resolution (16 arc-second, ~480 m) and daily High Mountain Asia snow reanalysis (HMASR) dataset is derived and analyzed in the dissertation.

The key conclusions are summarized as follows: 1) Snowfall precipitation is found underestimated in most precipitation products with sizeable uncertainty when evaluated in sub-domains of HMA.

The research shows the potential of using satellite snow observations as a constraint, to infer biases and uncertainties in snowfall precipitation in remote regions and complex terrain where in-situ stations are very scarce. 2) Through examining the HMASR dataset, the domain-wide peak seasonal snow storage is quantified as 163 km^3 when aggregated across the full HMA domain and averaged across WYs 2000-2017, with notable interannual variations between 114 km^3 and 227 km^3. 3) Existing global snow products over HMA on average underestimate the peak snow storage by 33% ± 52% over the entire HMA, and the uncertainty in peak snow storage estimates is primarily explained by accumulation season snowfall (88%) over HMA, partly due to a wide range (uncertainty) in precipitation (snowfall). Ultimately, the snow storage and its spatiotemporal variations characterized in this work can be used to understand the role of seasonal snowpack in the regional climate and water cycle over this region.

The dissertation of Yufei Liu is approved.

Dennis P. Lettenmaier

William Yeh

Yongkang Xue

Steven A. Margulis, Committee Chair

University of California, Los Angeles

2022

Table of Contents

List of Figures

List of Tables

ACKNOWLEDGEMENT

I would like to express my sincere thanks to my advisor Professor Steve Margulis, for the continuous support in my PhD study. He has encouraged me to explore this field when mentoring my undergraduate research, has provided very patient guidance in my graduate research with his expertise in the area.

I would like to thank my committee members: Professor Dennis Lettenmaier, Professor William Yeh and Professor Yongkang Xue. They provided very insightful comments that help to shape my research.

I would like to thank my parents for their encouragement and endless support throughout my life. My thank also goes to my friends, for being so supportive and helpful all the time.

Vita

EDUCATION:

University of California, Los Angeles — Los Angeles, CA
PhD, Hydrology — 2017- expected June 2022

University of California, Los Angeles — Los Angeles, CA
MS, Hydrology — 2016 – 2017

Hohai University — Nanjing, China
BS, Water Supply & Sewerage Engineering — 2012 – 2016

TEACHING EXPERIENCE

University of California, Los Angeles — Los Angeles, CA

Teaching Associate, Introduction to Hydrology	Fall 2021
Teaching Associate, Introduction to Hydrology	Fall 2020
Teaching Associate, Introduction to Hydrology	Fall 2019
Teaching Assistant, Applied Numerical Computing and Modeling in Civil and Environmental Engineering	Spring 2019
Teaching Assistant, Introduction to Hydrology	Fall 2018
Teaching Assistant, Introduction to Hydrology	Fall 2017

RELATED PUBLICATIONS:

Liu, Y. and Margulis, S. A.*: Deriving Bias and Uncertainty in MERRA-2 Snowfall Precipitation Over High Mountain Asia, Front. Earth Sci., 7, 280, doi:10.3389/feart.2019.00280, 2019.

Margulis, S. A.*, **Liu, Y.** and Baldo, E.: A Joint Landsat- and MODIS-Based Reanalysis Approach for Midlatitude Montane Seasonal Snow Characterization, Front. Earth Sci., 7, 272, doi:10.3389/feart.2019.00272, 2019.

Liu, Y., Fang, Y., and Margulis, S.A.: High Mountain Asia UCLA Daily Snow Reanalysis, Version 1. Boulder, Colorado USA, NASA Snow and Ice Data Center Distributed Active Archive Center, doi:10.5067/HNAUGJQXSCVU, 2021.

Liu, Y., Fang, Y. and Margulis, S. A.: Spatiotemporal distribution of seasonal snow water equivalent in High-Mountain Asia from an 18-year Landsat-MODIS era snow reanalysis dataset, The Cryosphere, 15, 5261–5280, https://doi.org/10.5194/tc-15-5261-2021, 2021.

Liu, Y., Fang, Y. and Margulis, S. A.: Intercomparison of seasonal snow water equivalent estimates over High-Mountain Asia (to be submitted to GRL)

CHAPTER 1

Introduction

1.1 Background and motivation

High Mountain Asia (HMA) consists of the highest mountain ranges (e.g. Tien Shan, Pamir, Kunlun Shan, Karakoram, Hindu-Kush, Himalayas) in Asia and the Tibetan Plateau. It provides sources of water for the largest river basins in Asia (e.g. Indus, Ganges, Brahmaputra, Yangtze, Yellow, etc.), which feeds billions of people living downstream (Immerzeel et al., 2010). The climate of this region is significantly affected by winter westerlies (brings moisture to the northwestern HMA), and the summer monsoons (brings moisture to the southeastern HMA), where the central HMA receives limited precipitation as vapor transport is blocked by the surrounding mountains (Aizen et al., 1997; Bookhagen and Burbank, 2010; Yao et al., 2012).

Melt water from seasonal snowpack and glaciers are an important source of water in the large river basins of HMA (e.g. Bookhagen and Burbank, 2010; Immerzeel et al., 2010; Armstrong et al., 2019; Khanal et al., 2021; Kraaijenbrink et al., 2021). Seasonal snowpack functions as a natural reservoir, which stores winter precipitation and releases it as snowmelt during spring and summer (Immerzeel et al., 2009). The snow-derived water supply is critical to meet the agricultural, industrial and human demands in HMA, in particular during the warm season when precipitation could be is insufficient in some regions (Bookhagen and Burbank, 2010; Kraaijenbrink et al., 2021).

1.2 Challenges in large-scale snow mass estimation

Despite the importance of snow-derived runoff in regional water cycle, our knowledge of the snow water equivalent (SWE) in HMA is poor. The spatiotemporal distribution in SWE and the overall snow storage remains largely uncertain. In fact, accurately estimating SWE at such scales remains

a great challenge worldwide, and it is even more difficult in mountainous regions due to the terrain complexity (Lettenmaier et al., 2015; Dozier et al., 2016; Bormann et al., 2018).

In-situ stations offer direct measurements of snow depth and/or SWE and are considered more reliable sources, often used in model assimilation and validation for snowpack estimation. However, these stations are sparsely located in HMA, usually installed at flat locations, which is less representative of mountain snowpack with complex terrain (Winiger et al., 2005; Palazzi et al., 2013; Kirkham et al., 2019).

Satellite-based platforms offer the potential for space-time continuous measurements of snow properties over large scales. Measurements of snowpack extent are broadly available from spaceborne platforms through the optical sensors (e.g. from Landsat, MODIS), with frequent (up to daily) and fine resolution (e.g. 30 m in Landsat), but are only indirectly related to snow mass. Snow depth and snow mass can be estimated from passive microwave sensors based on brightness temperature, yet such retrieval methods suffer from coarse resolution (e.g. 25 km) and bias (underestimation) in deep snowpacks (Takala et al., 2011; Dozier et al, 2016; Mortimer et al., 2020). The application of active microwave sensors yields the potential of high-resolution and direct measurements in snow depth (e.g. Lievens et al., 2019), but is only available within the recent years and do not always have an unambiguous relationship between snow depth and radar backscatter.

Global atmospheric reanalysis products provide another approach to large-scale SWE estimates as by-products of their land surface schemes. Nevertheless, most reanalysis datasets are not specifically designed for SWE estimation, and not well constrained by snow observations. Currently, there is still a need for large scale SWE datasets, that provide high-resolution and well-constrained snow estimates over a longer period and covering mountainous areas in this region.

1.3 Objective of the dissertation

The objective of this dissertation is to understand and quantify the spatiotemporal distribution in seasonal snow storage over HMA. To fill the spatiotemporal gap in existing SWE datasets and provide more realistic estimation of snow storage over HMA, we developed a novel High Mountain Asia snow reanalysis (HMASR; Liu et al., 2021) dataset. The dataset is derived using a newly developed snow reanalysis method (Margulis et al., 2019) that jointly assimilates fractional snow-covered area (fSCA) from the Landsat and MODIS platforms. SWE estimates are provided at fine resolution (16 arc-second, ~480 m) and daily, over Water Year (WY) 2000 – 2017 where Landsat and MODIS both exist. The snow reanalysis scheme is shown in details in the diagram below:

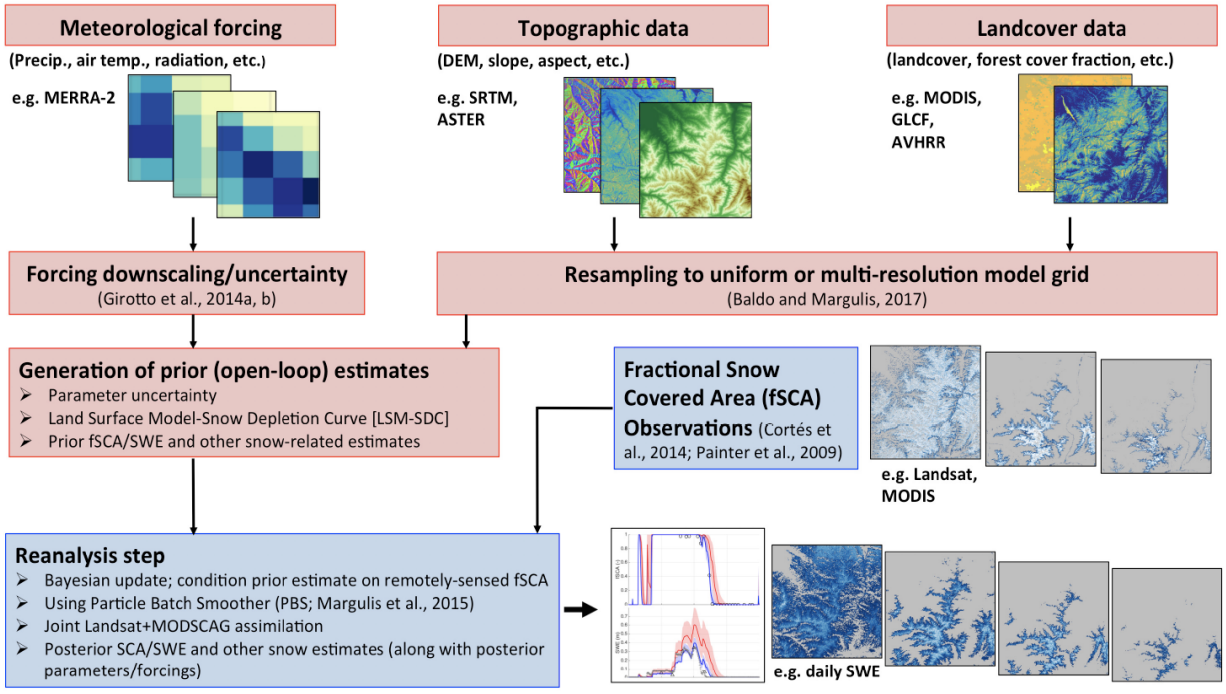

Figure 1.1: Flow chart showing the snow reanalysis scheme that is used to derive the HMASR dataset in this dissertation (Figure from Margulis et al., 2019)

To generate reasonable uncertainty estimates in snowfall precipitation before applying the snow reanalysis over the full HMA, the bias and uncertainty in MERRA-2 snowfall precipitation is characterized at several sub-domains within HMA, with the following research questions addressed:

1) Are the existing gridded snowfall products (e.g. MERRA2) biased over HMA and to what extent?
2) How can the bias and uncertainty in these snowfall precipitation products be parameterized over HMA and its subregions?

The derived uncertainty parameters were then applied in the development of the HMASR dataset over the full HMA domain. Through analyzing the HMASR dataset, the following scientific questions are addressed:

1) How is seasonal snow distributed spatially and temporally across the major watersheds of HMA?
2) What is the seasonal and interannual variability in the amount of snow storage over HMA?
3) How is snow storage distributed across elevation and how does it vary under different climate conditions?

The newly derived HMASR dataset offers the potential for evaluating the errors and uncertainty in SWE estimates from existing global datasets. In particular, the following scientific questions are addressed:

1) What is the uncertainty in peak seasonal snow water storage over HMA and its watersheds?
2) How much of the uncertainty in peak snow storage is explained by accumulation seasonal snowfall and ablation variability, respectively?

1.4 Organization of dissertation

The dissertation is organized into five chapters: Chapter 2 quantifies the bias and uncertainty in snowfall precipitation from existing datasets (e.g. MERRA2), over representative sub-domains in HMA. Chapter 3 presents the spatiotemporal distribution of seasonal snowpack over HMA, derived from the newly developed HMASR dataset, and quantifies the seasonal storage as well as its variations over time. Chapter 4 evaluates the uncertainty in peak seasonal snow storage from a multi-dataset comparison, and examines the fractional variability explained by accumulation season snowfall and ablation. Chapters 2 and 3 have already been published (Liu and Margulis, 2019; Liu et al., 2021), while it is anticipated Chapter 4 will be submitted for publication shortly. A brief summary of the key conclusion from this dissertation and proposed ideas for future work are presented in Chapter 5.

1.5 Bibliography

Aizen, V. B., Aizen, E. M., Melack, J. M., & Dozier, J. (1997). Climatic and Hydrologic Changes in the Tien Shan, Central Asia. *Journal of Climate*, *10*(6), 1393–1404. https://doi.org/10.1175/1520-0442(1997)010<1393:CAHCIT>2.0.CO;2

Armstrong, R. L., Rittger, K., Brodzik, M. J., Racoviteanu, A., Barrett, A. P., Khalsa, S.-J. S., Raup, B., Hill, A. F., Khan, A. L., Wilson, A. M., Kayastha, R. B., Fetterer, F., & Armstrong, B. (2019). Runoff from glacier ice and seasonal snow in High Asia: Separating melt water sources in river flow. *Regional Environmental Change*, *19*(5), 1249–1261. https://doi.org/10.1007/s10113-018-1429-0

Bookhagen, B., & Burbank, D. W. (2010). Toward a complete Himalayan hydrological budget: Spatiotemporal distribution of snowmelt and rainfall and their impact on river discharge.

Journal of Geophysical Research: Earth Surface, *115*(F3). https://doi.org/10.1029/2009JF001426

Bormann, K. J., Brown, R. D., Derksen, C., & Painter, T. H. (2018). Estimating snow-cover trends from space. *Nature Climate Change*, *8*(11), 924–928. https://doi.org/10.1038/s41558-018-0318-3

Dozier, J., Bair, E. H., & Davis, R. E. (2016). Estimating the spatial distribution of snow water equivalent in the world's mountains. *WIREs Water*, *3*(3), 461–474. https://doi.org/10.1002/wat2.1140

Immerzeel, W. W., Droogers, P., de Jong, S. M., & Bierkens, M. F. P. (2009). Large-scale monitoring of snow cover and runoff simulation in Himalayan river basins using remote sensing. *Remote Sensing of Environment*, *113*(1), 40–49. https://doi.org/10.1016/j.rse.2008.08.010

Immerzeel, W. W., van Beek, L. P. H., & Bierkens, M. F. P. (2010). Climate Change Will Affect the Asian Water Towers. *Science*, *328*(5984), 1382. https://doi.org/10.1126/science.1183188

Khanal, S., Lutz, A. F., Kraaijenbrink, P. D. A., van den Hurk, B., Yao, T., & Immerzeel, W. W. (2021). Variable 21st Century Climate Change Response for Rivers in High Mountain Asia at Seasonal to Decadal Time Scales. *Water Resources Research*, *57*(5), e2020WR029266. https://doi.org/10.1029/2020WR029266

Kirkham, J. D., Koch, I., Saloranta, T. M., Litt, M., Stigter, E. E., Møen, K., Thapa, A., Melvold, K., & Immerzeel, W. W. (2019). Near Real-Time Measurement of Snow Water Equivalent in the Nepal Himalayas. *Frontiers in Earth Science*, *7*, 177. https://doi.org/10.3389/feart.2019.00177

Kraaijenbrink, P. D. A., Stigter, E. E., Yao, T., & Immerzeel, W. W. (2021). Climate change decisive for Asia's snow meltwater supply. *Nature Climate Change*, *11*(7), 591–597. https://doi.org/10.1038/s41558-021-01074-x

Lettenmaier, D. P., Alsdorf, D., Dozier, J., Huffman, G. J., Pan, M., & Wood, E. F. (2015). Inroads of remote sensing into hydrologic science during the WRR era. *Water Resources Research*, *51*(9), 7309–7342. https://doi.org/10.1002/2015WR017616

Lievens, H., Demuzere, M., Marshall, H.-P., Reichle, R. H., Brucker, L., Brangers, I., de Rosnay, P., Dumont, M., Girotto, M., Immerzeel, W. W., Jonas, T., Kim, E. J., Koch, I., Marty, C., Saloranta, T., Schöber, J., & De Lannoy, G. J. M. (2019). Snow depth variability in the Northern Hemisphere mountains observed from space. *Nature Communications*, *10*(1), 4629. https://doi.org/10.1038/s41467-019-12566-y

Liu, Y., & Margulis, S. A. (2019). Deriving Bias and Uncertainty in MERRA-2 Snowfall Precipitation Over High Mountain Asia. *Frontiers in Earth Science*, *7*, 280. https://doi.org/10.3389/feart.2019.00280

Liu, Y., Fang, Y., & Margulis, S. A. (2021). High Mountain Asia UCLA Daily Snow Reanalysis, Version 1. Boulder, Colorado USA. NASA National Snow and Ice Data Center Distributed Active Archive Center. doi: https://doi.org/10.5067/HNAUGJQXSCVU.

Liu, Y., Fang, Y., & Margulis, S. A. (2021). Spatiotemporal distribution of seasonal snow water equivalent in High Mountain Asia from an 18-year \hack\break Landsat–MODIS era snow reanalysis dataset. *The Cryosphere*, *15*(11), 5261–5280. https://doi.org/10.5194/tc-15-5261-2021

Margulis, S. A., Liu, Y., & Baldo, E. (2019). A Joint Landsat- and MODIS-Based Reanalysis Approach for Midlatitude Montane Seasonal Snow Characterization. *Frontiers in Earth Science*, *7*, 272. https://doi.org/10.3389/feart.2019.00272

Mortimer, C., Mudryk, L., Derksen, C., Luojus, K., Brown, R., Kelly, R., & Tedesco, M. (2020). Evaluation of long-term Northern Hemisphere snow water equivalent products. *The Cryosphere*, *14*(5), 1579–1594. https://doi.org/10.5194/tc-14-1579-2020

Palazzi, E., von Hardenberg, J., & Provenzale, A. (2013). Precipitation in the Hindu-Kush Karakoram Himalaya: Observations and future scenarios. *Journal of Geophysical Research: Atmospheres*, *118*(1), 85–100. https://doi.org/10.1029/2012JD018697

Takala, M., Luojus, K., Pulliainen, J., Derksen, C., Lemmetyinen, J., Kärnä, J.-P., Koskinen, J., & Bojkov, B. (2011). Estimating northern hemisphere snow water equivalent for climate research through assimilation of space-borne radiometer data and ground-based measurements. *Remote Sensing of Environment*, *115*(12), 3517–3529. https://doi.org/10.1016/j.rse.2011.08.014

Winiger, M., Gumpert, M., & Yamout, H. (2005). Karakorum–Hindukush–western Himalaya: Assessing high-altitude water resources. *Hydrological Processes*, *19*(12), 2329–2338. https://doi.org/10.1002/hyp.5887

Yao, T., Thompson, L., Yang, W., Yu, W., Gao, Y., Guo, X., Yang, X., Duan, K., Zhao, H., Xu, B., Pu, J., Lu, A., Xiang, Y., Kattel, D. B., & Joswiak, D. (2012). Different glacier status with atmospheric circulations in Tibetan Plateau and surroundings. *Nature Climate Change*, *2*(9), 663–667. https://doi.org/10.1038/nclimate1580

CHAPTER 2

Deriving Bias and Uncertainty in MERRA-2 Snowfall Precipitation over High Mountain Asia

A Bayesian approach to estimate bias and uncertainty in snowfall precipitation from MERRA-2 and other precipitation products was applied over High Mountain Asia (HMA), using a newly developed snow reanalysis method. Starting from an 'uninformed' prior probability distribution, a posterior scaling factor applied to MERRA-2 snowfall was derived by constraining model-based estimates of seasonal snow accumulation and ablation over the water year (WY) with fractional snow covered area (fSCA) measurements derived from Landsat and MODIS (MODSCAG). Several sub-domains (nine representative 1° by 1° tiles) across HMA were examined over the period WYs 2001-2015 and compiled into an uncertainty parameterization where a lognormal distribution was fitted to the empirical posterior distribution with a mean of 1.54 (median of 1.19) and coefficient of variation of 0.83, indicating that MERRA-2 underestimates snowfall on average by ~54% with sizeable uncertainty. For reference, the uncertainties in snowfall precipitation from the ERA5 and APHRODITE-2 precipitation produces were also evaluated, and these products were found to underestimate snowfall, on average by a factor around 1.78 and 3.34 (with median scaling factors of 1.42 and 2.51) respectively. The results indicate that snowfall precipitation at high-elevations dominated by snowfall is underestimated in most existing products, especially in the gauge-based APHRODITE-2 product, where the biases were also found to exhibit geographical variations with the largest underestimation in monsoon-influenced high-elevation tiles. The derived MERRA-2 uncertainty model is being used to develop a full domain-wide HMA snow

reanalysis, which will shed further light onto the space-time variations in snowfall biases in these products.

2.1 Introduction

Accurate snowfall information is vital for hydrological modeling in snow-dominated regions, as it directly affects the estimation of snow water equivalent (SWE), and also influences streamflow prediction fed by snowmelt. This is especially important in High Mountain Asia (HMA), where a significant amount of precipitation falls as snow, resulting in large contributions of snowmelt to streamflow in many of its river basins (Bookhagen and Burbank, 2010).

Snowfall is highly uncertain in HMA due to the large spatial variability in precipitation, limited ground observations and uncertainty in satellite measured precipitation (Andermann et al., 2011; Bolch et al., 2012; Palazzi et al., 2013; Maussion et al., 2014). Meteorological stations are sparsely located in this region, generally located at lower elevations, and therefore data from these stations can lack representativeness of precipitation at unmonitored locations, most notably higher elevations (Winiger et al., 2005; Palazzi et al., 2013). Satellite observations such as TRMM (Tropical Rainfall Measuring Mission; Huffman et al., 2007) can provide spatially continuous precipitation estimates, but have been found to be uncertain and potentially biased in the HMA region (Anders et al., 2006; Bookhagen and Burbank, 2006; Andermann et al., 2011; Hussain et al., 2017; Khan et al., 2018). In addition, both remote sensing and in situ data sources generally perform worse at characterizing snowfall compared to rainfall, often with significant underestimates of snowfall rates, because their instruments are mainly designed to measure liquid rainfall rather than snow or ice (Anders et al., 2006; Viste and Sorteberg, 2015).

Precipitation can also be obtained from gridded datasets over the HMA region, including those derived from atmospheric reanalyses such as MERRA-2 (Modern-Era Retrospective analysis for

Research and Applications, version 2; Gelaro et al., 2017), and those that leverage interpolated rain-gauge data such as APHRODITE (Asian Precipitation Highly Resolved Observational Data Integration Towards Evaluation; Yatagai et al., 2012). Due to their coarse resolution, these gridded datasets often do not fully capture orographic precipitation in complex terrain (Palazzi et al., 2013) and those reliant on interpolated gauge data will suffer from the same representativeness issues at high elevations. Previous studies have investigated the uncertainty and bias in precipitation datasets, where significant variability among precipitation products was found over the Hindu-Kush Karakoram Himalayas region, in both total precipitation (Andermann et al., 2011; Palazzi et al., 2013) and snowfall estimates (Viste and Sorteberg, 2015).

Recent studies, using a variety of methods, suggest that most gridded precipitation datasets underestimate high-altitude precipitation in HMA. Tahir et al. (2011) found total annual precipitation estimates in APHRODITE to be lower than precipitation observed in high-altitude stations in the Hunza River Basin over the Karakoram range. Immerzeel et al. (2015) showed, by inversely inferring precipitation from glacier mass balance, that high-elevation precipitation in the upper Indus basin is underestimated in APHRODITE, ERA-Interim and TRMM, where ERA-Interim is a global atmospheric reanalysis from the European Centre for Medium-Range Weather Forecasts (ECMWF; Dee et al., 2011). Similarly, through evaluating runoff from glacio-hydrological modeling against observations, Wortmann et al. (2018) showed APHRODITE underestimates precipitation by a factor of 1.5-4.4 in Tarim headwater catchments. The information gleaned from these previous studies generally provides bulk bias estimates through inferring precipitation from spatially integrated variables like streamflow or glacier mass balance. Moreover, most of the studies to date have focused on the upper Indus basin or other small-scale

catchments and on total precipitation, but provide less information over the broad HMA domain, and have not quantified the biases in snowfall.

In this work, we used a Bayesian approach to estimate biases and uncertainties in MERRA-2 snowfall precipitation using a newly developed snow reanalysis method (Margulis et al., 2019) that can indirectly infer precipitation estimates, by constraining prior model estimates with remotely sensed fSCA images over the HMA region. The specific motivation for this study is to generate reasonable uncertainty estimates for snowfall precipitation in order to apply the same Bayesian approach over the full HMA domain as part of the NASA High Mountain Asia project. However, the goal of providing an accurate accounting of precipitation uncertainty is relevant to any hydrologic modeling study in the region and therefore should be of interest beyond generating a new snow reanalysis dataset. Herein we aim to primarily characterize the uncertainty in MERRA-2 snowfall precipitation at several sub-domains within HMA. Based on that characterization and inter-comparison with other products (e.g. APHRODITE-2 and ERA5) we address the following questions:

1) Is MERRA-2 snowfall biased over HMA and how can its bias and uncertainty be parameterized?
2) Is snowfall biased in other gridded precipitation products and to what extent?
3) How do the snowfall biases vary spatially for these products and what is the spatial-temporal distribution of snowfall?

2.2 Method and Dataset

2.2.1 Test Tiles and Years

The goal of this research is to characterize the uncertainty (including bias) in snowfall precipitation over HMA, which is critical for snow modeling in this region. We selected 9 representative tiles (1° longitude by 1° latitude) in our study domain to perform the analysis (Figure 2.1). These 9 test tiles were chosen to sample across variations in physiography and climate in the HMA region in order to assess the snowfall bias in different regimes. Four tiles are located in the western part of the domain, three tiles are located in southern part of the domain, and two tiles are located in the central/northeastern part of the domain (Figure 2.1). The expectation is that the precipitation regime of the first four tiles are dominated by winter westerlies, the southern three are influenced heavily by the Indian summer monsoon, and the remaining two are relatively dry locations forced by a mix of these and other synoptic drivers. Most of the selected tiles have a mean elevation above 3000 meters, with limited glacier and forest cover (Table 2.1). The test years were chosen as water years (WYs) 2001 to 2015, where both Landsat and MODIS observations are used in the reanalysis method described below. The WY spans October 1st through September 30th of the following year, where the WY label corresponds to the calendar year in which the WY ends.

Table 2.1: Glaciation, climatological, and physiographic characteristics for the 9 test tiles. The tile coordinates in the table refer to the lower left corner of each tile. Annual temperature (Ta) and precipitation (Precip.) are based on MERRA-2 data.

Tile Coordinates	Sub-domain	Mountain Range	Mean Elevation (km)	Glacial Coverage (%)	Mean Forest Fraction (%)	Annual Precip. (mm)	Mean Annual Ta (°C)
$(41°N, 77°E)$	Syr Darya	Tien Shan	3.8	13.3	1.1	719	-5.5
$(38°N, 70°E)$	Amu Darya	Pamirs	2.6	1.0	2.8	1223	5.6
$(34°N, 66°E)$	Hindu Kush	Hindu Kush	3.1	0.0	0.0	486	3.9
$(34°N, 75°E)$	Indus	Karakorum	4.1	4.2	3.8	1542	-0.8
$(29°N, 82°E)$	Ganges/ Brahmaputra	Himalayas	4.2	8.9	11.1	3376	-0.2
$(27°N, 90°E)$	Ganges/ Brahmaputra	Himalayas	3.2	1.0	49.4	5566	7.7
$(29°N, 97°E)$	Salween	Hengduan	4.5	5.0	7.1	1183	-0.1
$(36°N, 85°E)$	Tarim	Kunlun	4.9	0.5	0.0	387	-6.9
$(38°N, 98°E)$	Yellow	Qilian	4.1	1.1	1.5	723	-4.6

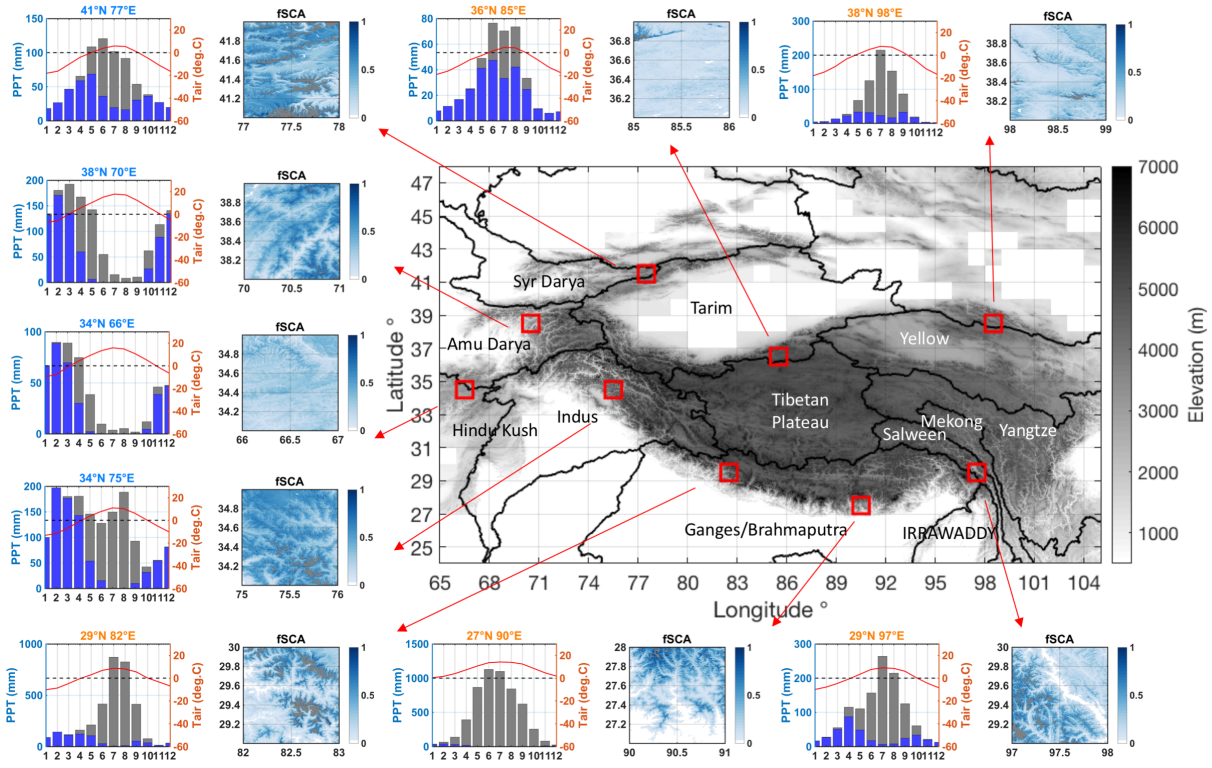

Figure 2.1: Elevation map of the HMA domain (middle) with locations of test tiles marked with red boxes. Major watersheds are delineated and labeled on the map, using the watershed boundaries from HydroSHEDS (Lehner et al., 2006). Corresponding to each test tile, the left panel shows the monthly climatology of precipitation (grey bars), snowfall (blue bars) and air temperature (red line), diagnosed by MERRA-2 data; the right panel shows the climatological mean fractional snow covered area (fSCA) map.

2.2.2 Deriving the Bias and Uncertainty in MERRA-2 Snowfall Precipitation

In this paper, we used the ensemble-based snow reanalysis method (Margulis et al., 2019) as a tool for estimating unknown precipitation biases and general uncertainty. The method is designed to acknowledge the typically large prior uncertainty in precipitation in high mountain regions and use a data assimilation approach to derive a posterior estimate that is constrained by the remotely sensed fSCA depletion time series. Specifically, a scaling factor *b* for precipitation is employed

for representing the prior uncertainty associated with the nominal precipitation estimate and its downscaling:

$$P_j(x_r, t) = b_{j,nom}(x_r) * P_{nom}(x_{nom}, t), \text{ for } j = 1, \ldots, N \quad (1)$$

where *j* is the replicate (individual realization) index and *N* is the total number of replicates in the ensemble. $P_j(x_r, t)$ is the snow reanalysis precipitation in replicate *j* at snow reanalysis pixel x_r and time *t*. In this application, the model resolution (x_r) is ~480 m (16 arcseconds). $P_{nom}(x_{nom}, t)$ is the nominal precipitation input from any precipitation data (e.g. MERRA-2 used in this study) at the nominal precipitation pixel x_{nom} and time *t*. $b_{j,nom}(x_r)$ is the scaling factor in replicate *j* at snow reanalysis pixel x_r, with respect to the nominal precipitation input P_{nom}. Typically, a specific distribution for *b* has been used in previous snow reanalysis applications (e.g. Durand et al., 2008; Girotto et al., 2014a; 2014b; Margulis et al., 2015; 2016; Cortés et al., 2016a; 2016b) with variations across different domains and/or with different precipitation products. For example, in the Sierra Nevada range in California (U.S.), *b* was postulated as lognormally distributed with a mean of 2.25 and coefficient of variation (CV) of 0.25 when applied with NLDAS-2 (Xia et al., 2012) precipitation (Margulis et al., 2015; 2016). While in the Andes range in Central Chile, *b* was postulated as lognormally distributed with a mean of 1.75 and CV of 0.95 when used with MERRA (Rienecker et al., 2011) precipitation (Cortés et al., 2016a; 2016b). The *b* distributional parameters can be derived from in-situ observation data (where available), and provide a mechanism for performing precipitation downscaling, first-order bias correction and prior uncertainty perturbation, where the snow reanalysis framework provides posterior estimates for these parameters through conditioning (a Bayesian update) on fSCA measurements.

In data scarce domains like HMA, there may be insufficient data to even postulate a prior uncertainty model for precipitation. Hence, in contrast to previous applications, herein we take the approach that we know almost nothing about the prior uncertainty in MERRA-2 precipitation (and how it should be downscaled) beyond a range of values seen in the literature. In this 'uninformed' approach, the prior *b* distribution is specified as uniformly distributed (i.e. with equal probability) between 0.1 and 5 to reflect the wide range of biases seen in the literature as well as the potential for sub-grid heterogeneity in precipitation. Using such a distribution allows for the prior ensemble to reflect both under- and overestimation by the nominal precipitation dataset (i.e. MERRA-2), where those realizations that are most consistent with independent (fSCA) data will be determined by the Bayesian update. We used 50 replicates for the ensemble size in this study, which was deemed sufficient based on preliminary sensitivity tests.

Characterization of the uncertainty in snowfall precipitation from MERRA-2 (including bias) is derived via the reanalysis step in the Particle Batch Smoother (PBS) approach (Margulis et al., 2019), which is achieved through the conditioning of the prior ensemble of *b* on independent fSCA observations to derive a posterior distribution. A schematic illustration of the method used for updating the *b* distribution at a particular modeling pixel in a particular water year is presented in Figure 2.2, which is elaborated on below.

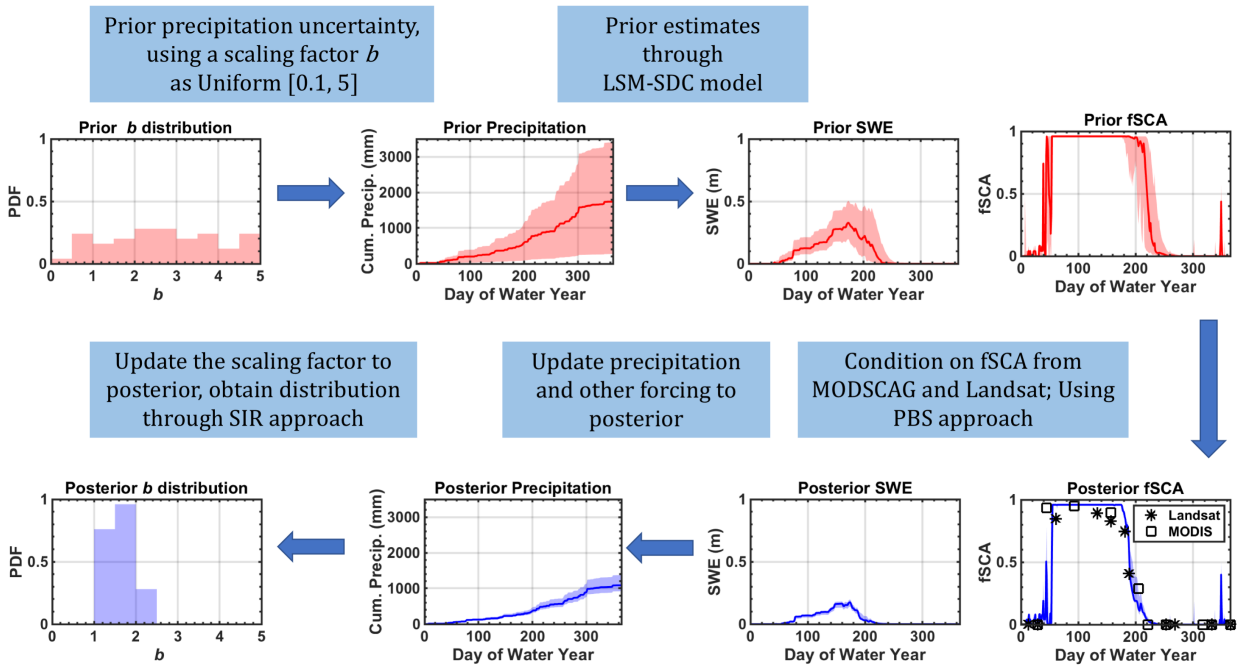

Figure 2.2: Flow chart highlighting how the reanalysis framework method is used to estimate uncertainty in snowfall precipitation at a particular modeling pixel in a particular water year, with red indicating prior and blue indicating posterior. In the time series plots, the shaded area shows the ensemble spread (inter-quartile range) and the solid line shows the ensemble median. Satellite retrieved fSCA from Landsat and MODSCAG are displayed in the posterior fSCA plot, and serve as the constraint that is used to infer snowfall precipitation.

In the PBS approach, all replicates in the ensemble are initialized with equal prior weights, where the weights are interpreted as the discrete probability for b and other variables in the corresponding replicate:

$$Prior: b_{j,nom}^{-}(x_r), \text{ with } w_j^{-}(x_r) = \frac{1}{N} \quad (2)$$

where $b_{j,nom}^{-}(x_r)$ is the prior scaling factor with respect to P_{nom} and $w_j^{-}(x_r)$ is the prior weight in replicate j at snow reanalysis pixel x_r. In this application a uniform distribution (between 0.1 and

5) is used to draw random prior samples of $b^-_{j,nom}$ (Figure 2.2). The uncertainty in b is propagated to prior predictions of fSCA ($fSCA^-_{pred,j}$) via the ensemble LSM-SDC modeling framework (Margulis et al., 2019). Modeling variables are updated through conditioning on the collection of satellite observed fSCA over the WY ($fSCA_{meas}$):

$$Posterior: b^+_{j,nom}(x_r) = b^-_{j,nom}(x_r),$$

$$\text{with } w^+_j(x_r) = \frac{c_0}{N} p_V\left[(fSCA_{meas}(x_r) - fSCA^-_{pred,j}(x_r)), C_V\right] \quad (3)$$

where $b^+_{j,nom}(x_r)$ is the posterior scaling factor with respect to P_{nom} and $w^+_j(x_r)$ is the posterior weight in replicate j at snow reanalysis pixel x_r, and p_v is the likelihood function of measurement error (with specified covariance C_V), and c_0 is a normalization constant through which the posterior weights sum up to one (Margulis et al., 2019).

Through conditioning on fSCA observations using the PBS approach, the modeling results are preserved in each replicate, but their corresponding weights are changed. Replicates with modeled fSCA closer to observations are assigned higher weights, and vice versa. The distribution of modeled variables (e.g. SWE, fSCA, etc.) and the b distribution at each pixel are therefore implicitly updated, due to the update in their posterior weights (Figure 2.2). It should be noted that, while the b scaling factor is applied to the total precipitation, since its posterior distribution is based on fSCA depletion, we would expect the posterior estimates should be most valid in snow-dominated pixels, i.e. where a sufficient fraction of annual precipitation falls as snow such that there is a clear seasonal snowpack with fSCA depletion that can be captured by the Landsat and MODSCAG measurements. It is also possible that in some instances the b scaling factor is correcting for the fact that some storms through the year were misclassified as rain or snow based

on the air temperature. This would be expected to occur in transition zones where air temperature is near-freezing during snowfall events.

In order to better interpret the posterior b distribution in terms of its probability rather than its posterior weights, we used a sequential importance resampling (SIR) algorithm (Zhou et al., 2006) to resample the b values, where we obtained a set of b values with the same posterior distribution but with equal weights. At each pixel, N samples (where N is the total number of replicates) are randomly drawn from the discrete (posterior) b distribution through a Monte-Carlo method, with the posterior weight $w_j^+(x_r)$ interpreted as the discrete probability to obtain the corresponding $b_{j,nom}^+(x_r)$. This generates a new sample set $\{b_{j,nom}^R(x_r) \,|j = 1, \dots, N\}$ (where the superscript R indicates "resampled") at each pixel with N samples, and assign equal weights ($w_j^R(x_r) = \frac{1}{N}$) to each sample. This intermediate step is done for convenience in order to merge individual pixel distributions together to derive the distribution across the tile(s) as described below.

We grouped the resampled scaling factor ensemble $b_{j,nom}^R(x_r)$ from all N samples and from all the pixels within each (1° by 1°) test tile into an ensemble $b_{tile,nom}^R$ to assess its tile-specific distribution, and also merged the $b_{tile,nom}^R$ samples from all the test tiles into a larger ensemble $b_{global,nom}^R$ to assess its 'global' distribution over the HMA region, with respect to the nominal precipitation P_{nom}. Furthermore, both $b_{tile,nom}^R$ and $b_{global,nom}^R$ are fitted with a lognormal probability function so as to parameterize the distributions. It should be noted that MERRA-2 is used as the nominal precipitation herein, such that the reanalysis application yields $b_{nom} = b_{MERRA2}$.

When merging the $b_{j,nom}^R$ from different pixels into a large sample such as $b_{tile,nom}^R$ and $b_{global,nom}^R$, careful screening is performed so as to exclude the non-updated pixels from

contaminating the distribution. Three types of pixels are excluded from the large sample, namely pixels with water bodies, pixels that are non-snowy at low elevations, and pixels with glaciers or persistent snow at high elevations. The water bodies are identified from the land cover types, and the non-snowy pixels are identified when there is insignificant change in the posterior weights from the prior. The glaciers or persistent snow pixels are identified when there is significant carry-over-snow that do not fully melt out in the melting season. Specifically, if, for a given pixel and year, the minimum SWE exceeds 1% of the maximum SWE, that pixel is considered to have significant carry-over-snow in that year, and that pixel-year is excluded in the large sample. It should be acknowledged that we found the posterior b distribution to be somewhat sensitive to the screening, especially for the carry-over-snow pixels at the high elevations (i.e. glacier pixels), hence the screening is meant to conservatively focus on seasonal snow pixels for the posterior b estimation.

2.2.3 Other Gridded Precipitation Datasets

To put the characterized MERRA-2 uncertainty results in larger context, we chose to also investigate the implicit uncertainty in two other gridded precipitation products, namely ERA5 (the fifth generation of ECMWF reanalysis product) and APHRODITE-2 (Asian Precipitation Highly Resolved Observational Data Integration Towards Evaluation; Yatagai et al., 2012).

ERA5 is the latest reanalysis dataset produced by ECMWF, which provides global estimates of atmosphere, land and ocean variables. The dataset is currently available from 1979 to present at an hourly step, gridded to a spatial resolution of 0.25°. We used its hourly total precipitation from Copernicus Climate Change Service (C3S, 2017; https://cds.climate.copernicus.eu/cdsapp#!/home) to obtain surface precipitation estimates. APHRODITE-2 is produced by the Research Institute for Humanity and Nature (RIHN) and the Meteorological Research Institute of Japan Metrological

Agency (MRI/JMA) and provides daily precipitation estimates regionally over Asia based on a dense gauge network, gridded to spatial resolutions of 0.25° and 0.5°. We used the latest version APHRO_MA V1801_R1 Monsoon Asia Area Daily precipitation (http://aphrodite.st.hirosaki-u.ac.jp/download/), which covers the period from 1950 to 2015.

Similar to MERRA-2, ERA5 is a reanalysis product that assimilates both ground and satellite observations, while APHRODITE-2 is a station-based product that derives its estimate by interpolating precipitation gauges. These datasets are recently released, but their previous versions (e.g. ERA-Interim and APHRODITE) have been commonly used in studies over HMA, and many studies have assessed their performance of precipitation estimates in this region (e.g. Palazzi et al., 2013; Immerzeel et al., 2015; Song et al., 2016; Hussian et al., 2017). Therefore, they are representative of an additional reanalysis product and gauge-based product respectively.

We used 0.25 ° gridded resolution for ERA5 and 0.5 ° for APHRODITE-2, so as to best approximate the MERRA-2 resolution. The period chosen for analysis was WYs 2001-2015, which was the shared common period across all three precipitation products and MODIS snow products. The annual precipitation climatology maps (over WYs 2001-2015) are shown in Figure 2.3. While some of the large scale precipitation features are similar, it is evident there are, in some cases, large differences between products.

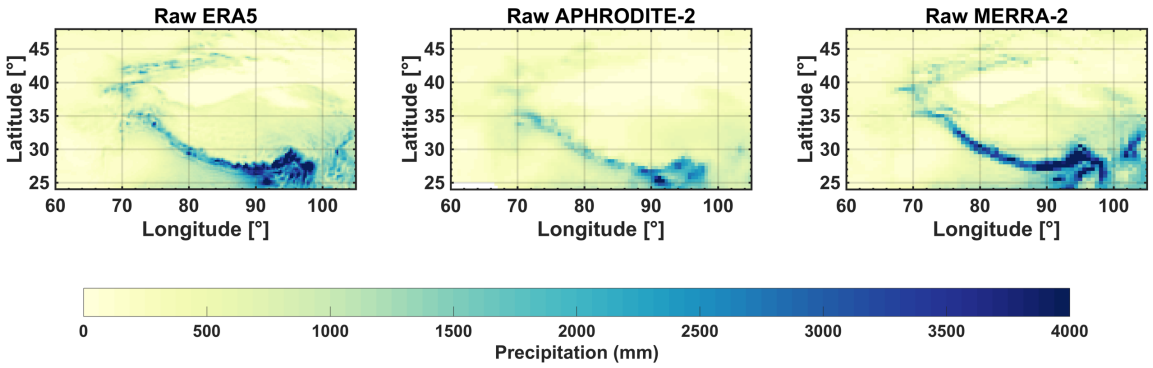

Figure 2.3: Annual total precipitation (in mm) climatology (WYs 2001-2015) for raw ERA5, raw APHRODITE-2 and raw MERRA-2 over the HMA region.

2.2.4 Deriving the Bias and Uncertainty in Snowfall Precipitation from Other Products

The primary goal of this paper is the derivation of bias and uncertainty estimates for the MERRA-2 product, which is accomplished by performing the snow reanalysis using the methodology described above. For context, bias and uncertainty estimates for the other gridded products were obtained by comparing them to the reanalysis estimates, i.e. whereby the posterior reanalysis estimates derived from MERRA-2 provide the reference. Specifically, note that the scaling factor b_{nom} that is derived for each WY using the nominal MERRA-2 precipitation inputs (i.e. b_{MERRA2}), can be thought of as follows by rearranging Equation (1):

$$b^R_{j,MERRA2}(x_r) = \frac{\bar{P}^R_j(x_r)}{\bar{P}_{MERRA2}(x_r)} = \frac{\overline{SP}^R_j(x_r)}{\overline{SP}_{MERRA2}(x_r)} \tag{4}$$

where $\bar{P}^R_j$ represents the cumulative annual snow reanalysis precipitation for replicate j and $\bar{P}_{MERRA2}$ represents the cumulative annual MERRA-2 precipitation. Since the scaling factor $b^R_{j,MERRA2}$ is particularly applied over snowfall precipitation (SP) that is conditioned on fSCA observations, $b^R_{j,MERRA2}$ is essentially the ratio between cumulative annual snowfall precipitation from the snow reanalysis ($\overline{SP}^R_j$) for replicate j and that from MERRA2 ($\overline{SP}_{MERRA2}$).

Using the same notion we can derive scaling parameters for the other products, i.e.:

$$b^R_{j,ERA5}(x_r) = \frac{\overline{SP}^R_j(x_r)}{\overline{SP}_{ERA5}(x_r)} \quad (5)$$

$$b^R_{j,APHRODITE2}(x_r) = \frac{\overline{SP}^R_j(x_r)}{\overline{SP}_{APHRODITE2}(x_r)} \quad (6)$$

To avoid large scaling factors due to very small cumulative snowfall values in the denominator of Equations (5) and (6), any cases with less than 5 cm of cumulative annual snowfall were excluded from the analysis. Given the derived scaling factors for each product at the pixel scale, they were then aggregated to tile-based and global distributions in the same manner as described above for comparison with MERRA-2 and the snow reanalysis.

In addition to precipitation itself, snowfall is dependent on air temperature. In the HMA snow reanalysis with MERRA-2 as the nominal forcing input, air temperature uncertainty is characterized with a normal distribution of N(-0.9℃, 1.2℃) based on the comparison to in-situ observations (Margulis et al., 2019). This means that the raw MERRA-2 air temperature was found to be 0.9℃ higher than in-situ on average, and this warm bias is corrected before performing the snow reanalysis. Similar bias-correction should also be performed in the ERA5 and APHRODITE-2 air temperature before computing snowfall, so as to eliminate the effect of air temperature biases in the scaling factors. For consistency, we choose to commonly apply the snow reanalysis air temperature over all three products to obtain their snowfall estimates, which is essentially derived from the bias-corrected MERRA-2 air temperature. A threshold of 2℃ daily mean air temperature is applied to classify snowfall vs. rain over the daily precipitation, where daily precipitation is still obtained from their original product. The obtained snowfall in ERA5 and APHRODITE-2 is further used in Equation (5)-(6) to derive the snowfall bias estimates.

It should be noted that snowfall biases in ERA5 and APHRODITE-2 are obtained herein by comparing to snowfall estimates from the snow reanalysis (i.e. “bias-corrected” MERRA-2 data).

This necessarily ties the baseline most closely to MERRA-2 rather than the other products, although the posterior corrects the raw MERRA-2 to values that are most consistent with the independent fSCA observations. This choice was made primarily because 1) the focus of this paper is on deriving an uncertainty parameterization for MERRA-2 and 2) due to the higher computational expense of running the reanalysis with each precipitation product. We leave a more thorough multi-product reanalysis for future work, and herein use the methods described above to provide a first-order comparison of the MERRA-2 biases relative to those from ERA5 and APHRODITE-2. Potential additional uncertainties introduced using our simplified comparison method come primarily from the diagnosis of MERRA-2 snowfall (i.e. using the 2 ℃ air temperature threshold) at the hourly time step, while for ERA5 and APHRODITE-2 we diagnose snowfall using the same threshold but at the daily time scale.

2.3 Results and Discussion

The snow reanalysis framework provides posterior pixel-wise estimates of the scaling factor b_{MERRA2} and the resulting seasonal precipitation time series. In the sections below, for each of the test tiles we present the resulting spatial distributions of climatological posterior precipitation and MERRA-2 tile-specific distributions for the scaling factor $b^R_{tile,MERRA2}$, and the distribution across all of the tiles examined herein as $b^R_{global,MERRA2}$. We then compare the derived snowfall uncertainty relative to the other precipitation products examined and compare how the posterior snowfall distribution varies with time and elevation in comparison to MERRA-2 and the other products.

2.3.1 Snowfall Biases and Uncertainties in MERRA-2

The climatology (i.e. average over WYs 2001-2015) maps of the interpolated MERRA-2 precipitation, the downscaled MERRA-2 snowfall, the posterior snowfall from the snow reanalysis

(hereafter referred to as "snow reanalysis snowfall") and the posterior b from the snow reanalysis at each of the test tiles are shown in Figure 2.4 (along with the respective elevation maps for reference). The snow reanalysis derived maps (posterior snowfall and posterior b) represent the climatology of the ensemble median fields. It should be noted that the conditioning of posterior b is most effective in seasonally snow-covered regions, so non-snowy or glacierized regions are masked out in Figure 2.4 and all results that follow. In terms of the spatial distribution, the MERRA-2 precipitation is bilinearly interpolated to the model grid (this is what the prior model uses as nominal input), but still retains the characteristics of the raw fields, and shows a smooth (coarse) representation of the precipitation field within a given 1 degree tile. The same smoothness is propagated to the downscaled MERRA-2 snowfall, which shows a mixed pattern of precipitation gradients and terrain variation, where the latter is due to the dependence on air temperature (which is downscaled to the model resolution). In contrast, the snow reanalysis effectively downscales the coarse-scale MERRA-2 by leveraging information in the set of higher-resolution (~480 m) fSCA images over each WY and in other model-based fields (i.e. terrain). For example, the $34°N$ $66°E$ tile in the Hindu Kush (Figure 2.4, third row) is characterized by a general elevation gradient from southwest to northeast, with the highest mountains in the northeast and lower lying valleys elsewhere. Due to its coarse resolution in the raw MERRA-2 fields, the spatial pattern of the interpolated MERRA-2 precipitation is nearly uniform in this tile (~500 mm/year) and clearly does not reflect the expected heterogeneity for such complex terrain. The downscaled MERRA-2 snowfall also has a smooth field (where the heteoregeneity is introduced through air temperature dependence on elevation), with snowfall ranging between 200 mm to 500 mm in this tile. The snow reanalysis snowfall is significantly more heterogeneous, without preserving the continuous and smooth features from precipitation or elevation as in the downscaled MERRA-2 data. It also

exhibits high snowfall estimates at high elevations in the mountains and low snowfall in the valleys, but with more dramatic gradients across elevation. The snow reanalysis snowfall is greatly enhanced in the highest elevation mountain chain on its windward side, where the orographic precipitation would be expected, and it is greatly reduced in the northeasternmost valley on its leeward side, where a rainshadow would be expected. Similar heterogeneity in the snow reanalysis snowfall is seen across the other test tiles (Figure 2.4, fourth column), which are attributed to the heterogeneity in the fSCA data and the effects of topography on snowfall. Beyond the heterogeneity (downscaling), the snow reanalysis snowfall also contains bias correction, where most tiles (fourth column) show tile-average differences with the MERRA-2 data (third column).

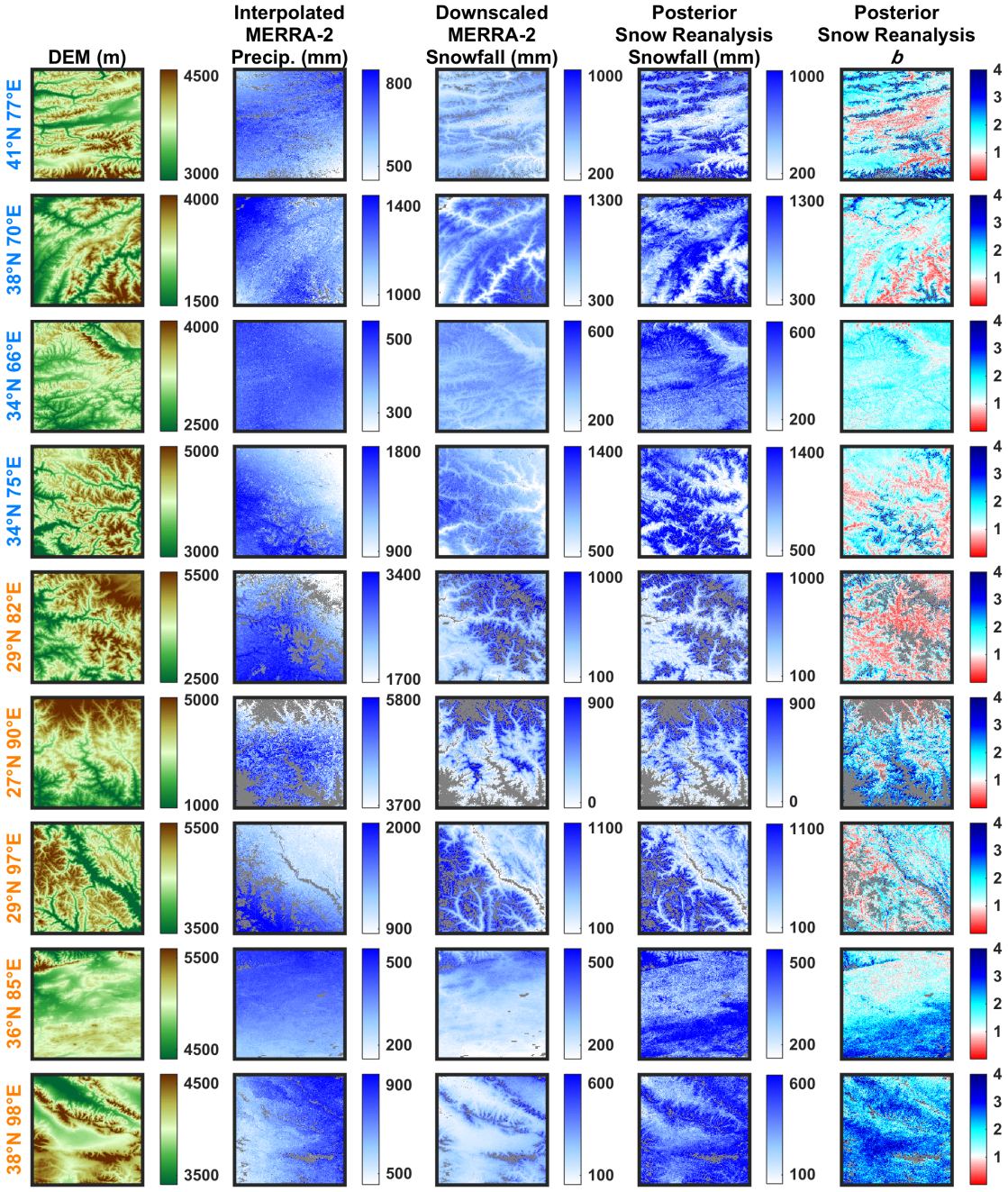

Figure 2.4: (first column) DEM, and climatology (WY 2001-2015) for the: (second column) interpolated MERRA-2 precipitation, (third column) downscaled MERRA-2 snowfall, (fourth column) posterior snow reanalysis snowfall (ensemble median), and (fifth column) posterior snow reanalyis *b* (ensemble median) in each of the test tiles. Tile labels in blue and orange text represent their locations in the western domain or central-eastern domain respectively.

The spatial distribution of snow reanalysis snowfall (Figure 2.4, column 4) is a function of the spatial patterns in the posterior b maps (Figure 2.4, column 5), i.e. Equation (1), which are conditioned on fSCA data. The posterior b estimates are expected to be most robust in regions where there is a strong seasonal cycle in snow accumulation and ablation that is captured by the fSCA data. It shows complex patterns that reflect the combined effect of two possible corrections to the coarse scale MERRA-2 data: i) downscaling of MERRA-2 data that is accurate in a tile-averaged sense but does not reflect the high-resolution patterns due to orography and other factors and ii) bias-correction of large-scale errors in MERRA-2 data. For example, in tile $38°N\ 70°E$, the posterior b (ensemble median) is generally between 1.0 and 2.0, indicating that the MERRA-2 snowfall is underestimated, and the snow reanalysis performs a bias-correction that effectively increases snowfall in this tile. However, the posterior b is also lower (and below 1.0) in certain pixels corresponding to the valleys in this tile, indicative of snowfall being overestimated in the downscaled MERRA-2 at those locations. Similar patterns are observed in other tiles, where the ensemble median of the posterior b is generally found to be between 1.0 and 2.0, but also exhibits values below 1.0 mostly in the valleys. Furthermore, the posterior median b is also found above 2.0 at a few locations in these tiles, and are most apparent in tiles $27°N\ 90°E$, $36°N\ 85°E$, and $38°N\ 98°E$. We hypothesize that the higher posterior b observed in $36°N\ 85°E$ (over the southern side mountains) is primarily due to capturing orographically enhanced precipitation, while that observed in tile $27°N\ 90°E$ (at the foot of the mountain on the southern side) is primarily due to the misclassification of snow as rain. For tile $38°N\ 98°E$ where the posterior b is found highest in the valleys, we hypothesize that it is primarily due to the non-effective updates in the intermittent snow. This tile is characterized by more intermittent snow that in some cases lasts only for several days at a time, where the accumulation or ablation of snow is more difficult to capture in the fSCA

measurement time series. As discussed earlier, the update in posterior b is most effective for seasonal snow pixels, which feature a distinct snow accumulation and ablation cycle that is reflected in fSCA observations.

To provide a bulk assessment of the uncertainties, the posterior b distribution climatology across each tile ($b^R_{tile,MERRA2}$) is shown in Figure 2.5 (blue bars). Note for reference that the prior distribution was uniform (dashed line) across the range so that the posterior distribution reflects the update in knowledge based on the assimilated fSCA measurements. The common feature seen in the empirical $b^R_{tile,MERRA2}$ distributions is that they all are skewed to the right, and most tiles are distinctly unimodal. To parameterize the empirical distributions, we chose to use a lognormal distribution. The lognormal distribution is commonly used in the literature to characterize the uncertainty distribution in precipitation, because it ensures non-negative precipitation, and the logarithm is suitable to characterize the extremely high precipitation amounts occurring at a low frequency. The fitted lognormal functions (using maximum likelihood estimation) are shown in Figure 2.5 (red curves), which match the empirical distributions well in most of the tiles (with the exception of $38°N\ 98°E$). For example, in tile $38°N\ 70°E$, the posterior $b^R_{tile,MERRA2}$ is highly right skewed with a mean of ~1.3 with most samples falling within a range of 0 to 2.5. In terms of the reanalysis procedure, this is indicative that replicates with values above 2.5 essentially have zero posterior weight and those near the mode have higher weights than the equal weights implicit in the prior uniform distribution. The other tiles in the western part of the domain ($41°N\ 77°E$, $34°N\ 66°E$, $34°N\ 75°E$), those in the south and east ($29°N\ 82°E$, $27°N\ 90°E$, $29°N\ 97°E$) and one in the northern Tibetan Plateau ($36°N\ 85°E$) similarly show unimodal skewed distributions with mean values ranging from 1.0 – 1.9 and coefficient of variations ranging from 0.5 - 1.2. The tile in the northeastern Tibetan Plateau ($38°N\ 98°E$, Figure 2.1) is an exception in that, while right

skewed, the peak is not as distinctive and has much heavier tails on the right. As a result, it has a higher mean value of ~2.5. From the empirical distribution it is clear that many of the higher prior values remain in the posterior distribution with non-negligible weights, where we hypothesize that the posterior b update may not be as effective in this tile due to intermittent snow, so that the $b^R_{tile,MERRA2}$ distribution still retains some of the features of the prior uniform distribution.

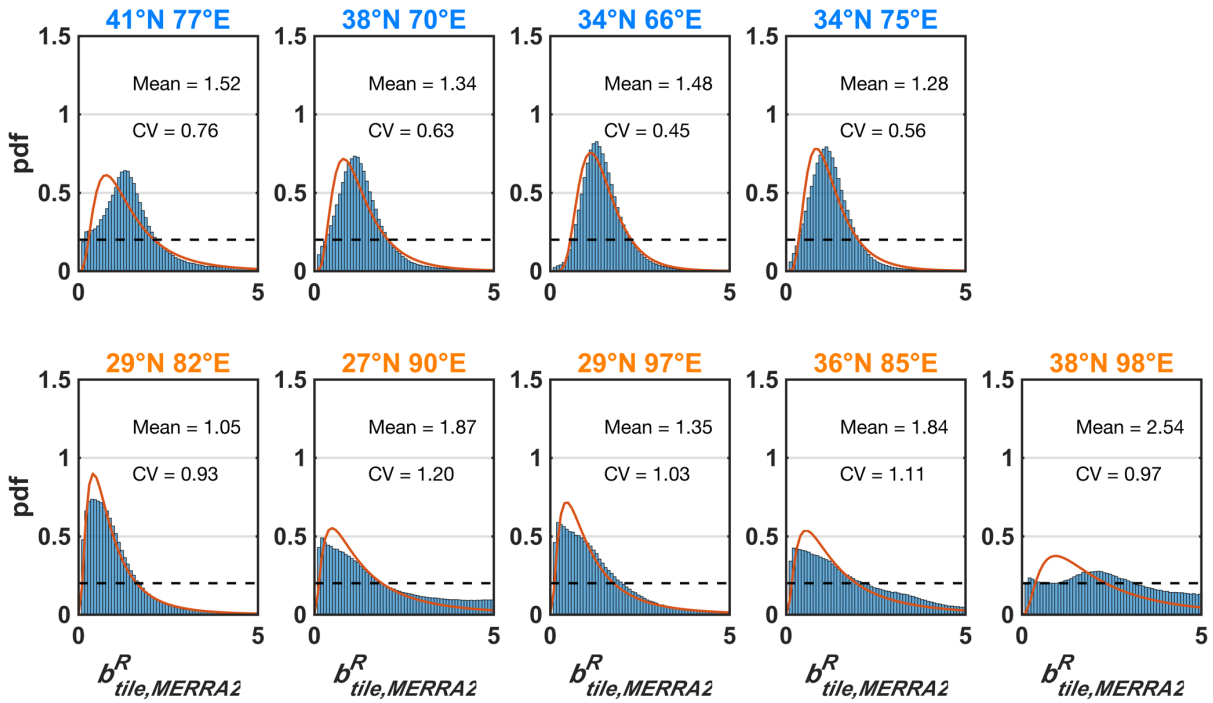

Figure 2.5: Distribution of $b^R_{tile,MERRA2}$ obtained from the snow reanalysis. The blue bars represent the empirical (posterior) distribution, the solid line is the fitted lognormal distribution, and the dashed line shows the prior uniform distribution for reference. The fitted lognormal parameters are displayed in each panel. Tile labels in blue and orange text represent their locations in the western domain or central-eastern domain respectively.

For the purposes of applying the snow reanalysis (or for other modeling applications) over the full HMA domain, it is useful to derive a single "global" distribution for b that could serve as a prior estimate of uncertainty in MERRA-2 precipitation (snowfall). The global distribution of MERRA-

2, i.e. $b^R_{global,MERRA2}$, is presented in Figure 2.6 (left). It is the composite of the tile-specific distributions and therefore is also highly right skewed with a single mode around 1, with most of the values between 0.1 and 3. We again fit a lognormal function to the empirical global distribution, where it fits reasonably well but with a slightly higher and narrower peak than the empirical distribution (mostly due to the one tile described above). The lognormal distribution exhibits a mean value of 1.54 (median value of 1.19) and CV of 0.83 for the $b^R_{global,MERRA2}$ distribution. This implies that, on average, the magnitude of raw MERRA-2 snowfall is 54% too low compared to the snowfall diagnosed from the snow reanalysis over the HMA region. Moreover, the CV implies that there is significant uncertainty that should be considered when using MERRA-2 data for snow modeling in HMA. In other words, using MERRA-2 deterministically in snow modeling over HMA is likely to underestimate the snowfall distribution in terms of both the mean and its uncertainty. This global distribution is currently being used as the prior uncertainty model for precipitation inputs in applying the snow reanalysis over the full HMA domain shown in Figure 2.1. The posterior estimates from that application will ultimately yield additional insight into the snowfall distribution over HMA that could be used to derive a more robust estimate of snowfall uncertainty and how it depends on physiographic, climatological, or other factors.

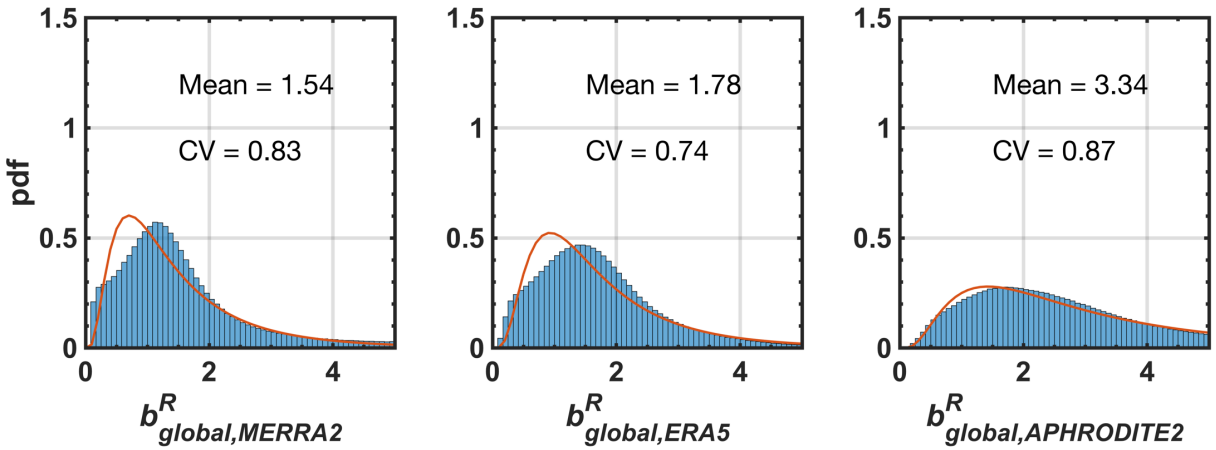

Figure 2.6: Derived distributions of the global precipitation scaling factor for MERRA-2 ($b^R_{global,MERRA2}$, left), ERA5 ($b^R_{global,ERA5}$, middle), and APHRODITE-2 ($b^R_{global,APHRODITE2}$, right). The blue bars represent the empirical (posterior) distribution, the solid line is the fitted lognormal distribution, and the dashed line shows the prior uniform distribution for reference. The fitted lognormal parameters are displayed in each panel. (Note the Bayesian approach is only used to derive the scaling factors in MERRA-2 precipitation, while those in ERA5 and APHRODITE-2 are derived through comparing to posterior snow reanalysis results).

2.3.2 Snowfall Biases and Uncertainties in other Gridded Precipitation Products

The posterior snowfall biases and uncertainties provide a mechanism (i.e. reference baseline) to also provide a first-order characterization of uncertainty in other gridded precipitation products (ERA5 and APHRODITE-2) using Equations (5)-(6). For clarity it should be noted that posterior *b* values represent a bias-correction relative to the nominal product such that *b* values larger than 1.0 represent a negative bias (underestimate) by the product and vice versa. The equivalent global uncertainty (i.e. resampled across all nine tiles) in snowfall precipitation in the other gridded products is shown in Figure 2.6 (middle and right). Based on the fitted lognormal distributions, we found that ERA5 has a comparable mean value of ~1.78 (median of 1.42), while APHRODITE-2

has a much higher mean value of ~3.34 (median of 2.51). This indicates that ERA5 is ~80% too low compared to the snowfall from the snow reanalysis, while APHRODITE-2 underestimates snowfall precipitation by more than a factor of 3. The CV values across all three products are comparable (~0.74-0.87), but the higher mean values in APHRODITE-2 imply a larger range of uncertainty. The large mean value for APHRODITE-2 is influenced in part by geographic differences across the domain. In particular, in the tiles east of $82°E$ (i.e. those most influenced by the Indian monsoon), the biases are generally above 4. Previous studies have pointed out that MERRA-2 snowfall is much greater than CRU TS (Climatic Research Unit Time series; Harris et al., 2014), TRMM and APHRODITE snowfall in the HMA region (Viste and Sorteberg, 2015), which is therefore consistent with larger underestimates in APHRODITE-2 compared to MERRA-2. The underestimation of snowfall in the gauge-based APHRODITE-2 product, may be caused by not only the interpolation of gauges at lower elevations, but also the undercatch of snow and ice by traditional instruments in those gauges (Palazzi et al., 2013; Viste and Sorteberg, 2015). It should be noted that the analysis herein, by construct focuses on snowfall (not rainfall) by selecting high-elevation/snow-covered pixels, so that biases in APHRODITE-2 precipitation in lower elevation/rain-dominated (i.e. monsoon influenced) regions might be substantially lower.

The geographic variation in the (tile-specific) biases across products is illustrated in Figure 2.7, where the biases are generally greater than 1 across all tiles in all datasets. It is apparent that the implied snowfall bias corrections in all datasets are smallest (less than ~2) in the three western tiles ($38°N\ 70°E$, $34°N\ 66°E$, $34°N\ 75°E$) and the southwestern tile ($29°N\ 82°E$) of the domain. The snowfall biases in all datasets are relatively larger (greater than ~2) in the northwestern tile ($41°N\ 77°E$) and the northeastern tile ($38°N\ 98°E$). For the remaining three tiles in the southern ($27°N\ 90°E$, $29°N\ 97°E$) and central-northern ($36°N\ 85°E$) part of the domain, it is only

APHRODITE-2 that show significantly large biases greater than 3. In contrast, the snowfall biases in MERRA-2 and ERA5 are relatively small (less than 2) in these tiles and are comparable to the other tiles. For the one tile ($38°N$ $98°E$) with more intermittent snow, where we hypothesize this leads to less robust posterior estimates, the biases are generally largest across products as shown in Figure 2.7. Whether these high biases are meaningful still needs further investigation. However, larger bias correction factors in areas like these tiles, where snowfall is very low, may not be as impactful as in other areas where snowfall is large.

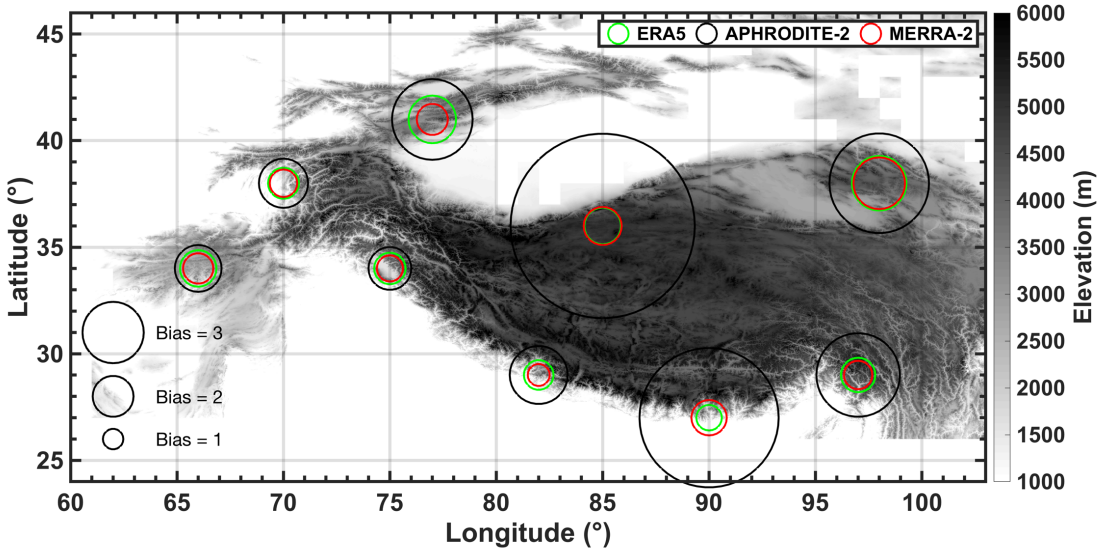

Figure 2.7: Geographic distribution of the snowfall bias correction (mean of b^R_{tile}) at each tile location across all precipitation datasets, including ERA5 ($b^R_{tile,ERA5}$, green), APHRODITE-2 ($b^R_{tile,APHRODITE2}$, black), and MERRA-2 ($b^R_{tile,MERRA2}$, red). The size of the circle is proportional to the value of the bias correction in each dataset, where a larger circle means greater bias (snowfall is more heavily underestimated in that dataset) and vice versa.

In summary, when compared to the posterior snow reanalysis, the MERRA-2 is less biased than the other products in most tiles (7 out of 9 tiles) followed by ERA5 (2 out of 9 tiles) (Figure 2.7).

In contrast, APHRODITE-2 shows the highest bias in all of the tiles, which is consistent with the global distributions shown in Figure 2.6. The magnitudes of snowfall biases in all three products are more consistent in the western part of the domain, but less consistent in the central and eastern part of the domain. The most obvious differences are seen in the central part of the domain ($36°N$ $85°E$, $27°N$ $90°E$), where the snowfall biases from MERRA-2 and ERA5 are comparable and lower, while the snowfall biases from APHRODITE-2 are higher.

2.3.3 Annual Snowfall Time Series among Different Products

The posterior snowfall in the snow reanalysis was compared to the other precipitation products over the period of WYs 2001-2015 at each test tile (Figure 2.8). We found that the overall snowfall magnitude in the downscaled MERRA-2 is lower than that in snow reanalysis estimates at most tiles. Taking the tile $34°N$ $66°E$ as an example, the snow reanalysis (blue line) snowfall is generally between 300-600 mm, while the MERRA-2 snowfall (red line) is between 200-500 mm and around 100 mm lower than the snow reanalysis. Similar patterns between MERRA-2 and the snow reanalysis snowfall can be observed in the other tiles, where MERRA-2 is generally lower than reanalysis snowfall in overall magnitude, which is consistent with the tile-specific and global distributions discussed above. The differences in snowfall between MERRA-2 and snow reanalysis is smallest in the two southern tiles ($29°N$ $82°E$, $27°N$ $90°E$), where MERRA-2 shows a comparable magnitude of snowfall relative to the snow reanalysis. The largest differences are observed in the northeastern tile ($38°N$ $98°E$), where snowfall in MERRA-2 is around 200 mm smaller than that in snow reanalysis. Since we hypothesize the posterior estimates are less robust in this $38°N$ $98°E$ tile with more intermittent snow, the posterior snowfall from snow reanalysis may be less reliable in this tile, explaining the large discrepancy between snow reanalysis and MERRA-2 in this tile.

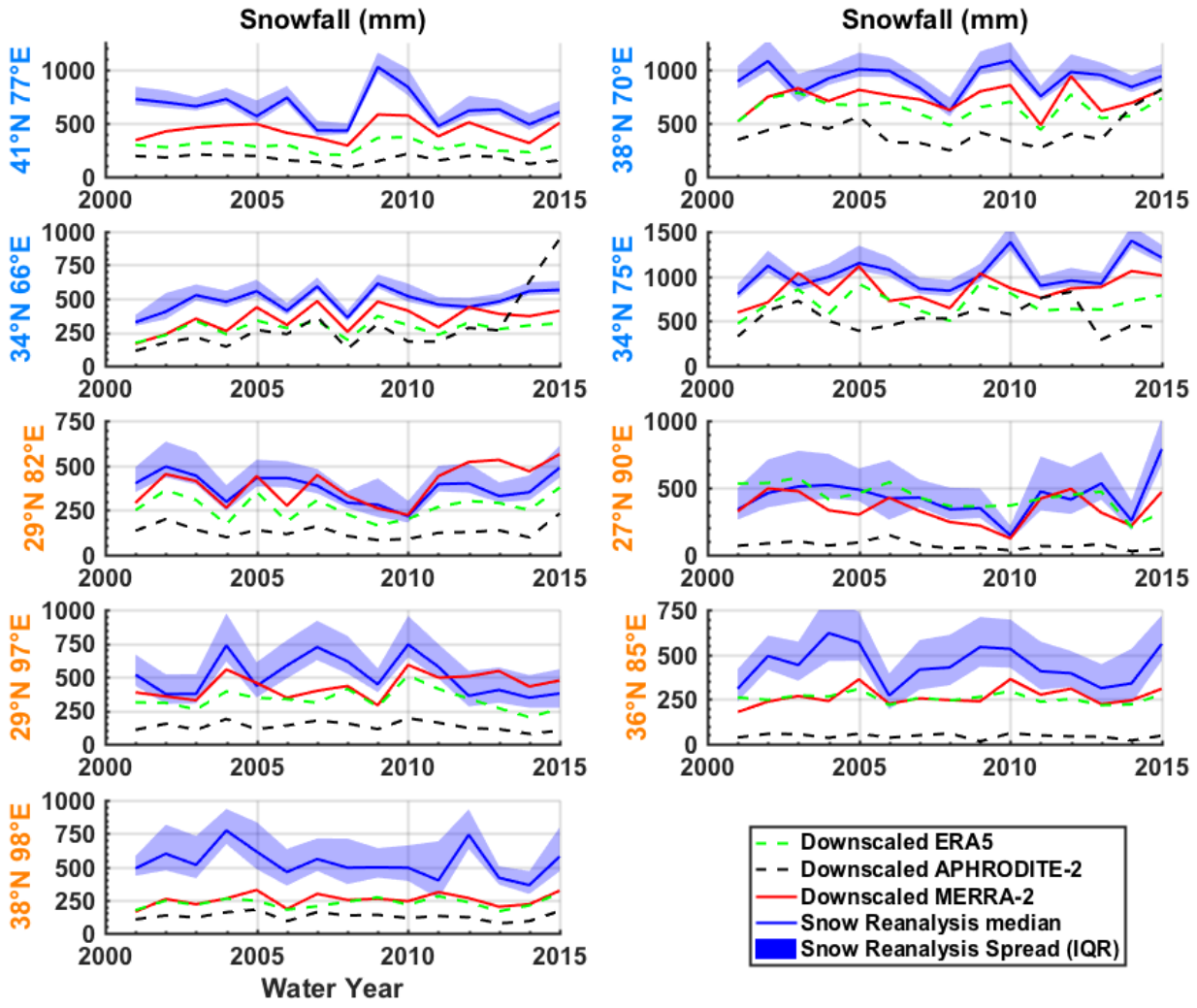

Figure 2.8: Tile-averaged annual total snowfall time series from downscaled ERA5, downscaled APHRODITE-2, and downscaled MERRA-2 vs. the snow reanalysis (ensemble median and interquartile range). Tile labels in blue and orange text represent their locations in the western domain or central-eastern domain respectively.

Snowfall time series estimates from other gridded products (ERA5 and APHRODITE-2) are also generally lower than the snow reanalysis. The magnitude of snowfall in ERA5 is comparable and slightly lower than MERRA-2, while that in APHRODITE-2 is significantly lower than all the

products, which is consistent with the snowfall biases discussed above (Figure 2.6). ERA5 snowfall is lower than both MERRA-2 and snow reanalysis in the western tiles, while in the central-eastern domain it is sometimes comparable to MERRA-2 but lower than snow reanalysis ($36°N$ $85°E$ and $38°N$ $98°E$), or comparable to the snow reanalysis ($27°N$ $90°E$) and higher than MERRA-2. APHRODITE-2 shows the minimum snowfall across all products, and the differences between APHRODITE-2 and other products are most apparent in the two southern tiles ($27°N$ $90°E$, $29°N$ $97°E$) and one central-northern tile ($36°N$ $85°E$), which is also consistent with the tile specific snowfall biases shown in Figure 2.7. Our results suggest that snowfall at these high-altitude tiles is generally underestimated in the gauge-based products over HMA, which is consistent with Immerzeel et al. (2015) and Wortmann et al. (2018), where high-altitude precipitation was found to be underestimated in many existing products. Since the gauge-based products derive their estimates primarily by interpolating rain-gauges located at lower elevations, it is possible that those gauges undercatch precipitation and do not capture orographic effects, which consequently underestimates snowfall.

The ensemble uncertainty in snowfall estimated from the snow reanalysis varies across the tiles (Figure 2.8). In general, the ensemble spread is relatively low in the western tiles, corresponding to the lower CV values in the $b^R_{tile,MERRA2}$ (~0.4-0.8 in Figure 2.5), and relatively high in the central and eastern tiles, corresponding to the higher CV values in the $b^R_{tile,MERRA2}$ (~0.9-1.2 in Figure 2.5). As discussed earlier, the conditioning of the posterior *b* is most effective for seasonal snow. The western tiles are dominated by westerlies, and therefore receive most snowfall in winter when precipitation occurs; while the central-eastern tiles are more affected by monsoons, and receive less snowfall in winter but more in spring or summer (Figure 2.1). As a result, there is a strong seasonal cycle in the fSCA observations over the western tiles, resulting in better conditioning of

the posterior b and lower uncertainties in snowfall. In the central-eastern tiles, the fSCA observations are less seasonal, resulting in less effective conditioning of the posterior b and higher uncertainties in snowfall.

In terms of the temporal correlations, snowfall in the gridded precipitation products are almost all positively correlated with snowfall from the snow reanalysis (Table 2.2). One exception is the correlation between APHRODITE-2 and the snow reanalysis, where a negative correlation coefficient of -0.13 exist in tile ($34°N$ $75°E$). Looking at individual tiles, the highest correlation coefficient averaged across all products is 0.76 for tile $34°N$ $66°E$. The lowest average correlation coefficient is 0.31 for tile $34°N$ $75°E$, mainly due to the negative coefficient from APHRODITE-2. On average, the correlation coefficient with the snow reanalysis annual time series is highest for ERA5 (0.63), followed by MERRA-2 (0.57), and APHRODITE-2 (0.42). These averaged coefficient values, indicate that snowfall variability from the reanalysis is not fully explained by snowfall from the input products. This is not surprising, and not necessarily a drawback, because the reanalysis snowfall is conditioned on independent fSCA observations; therefore its variations should reflect the temporal variation in fSCA, which are more directly connected to snow dynamics than any of the precipitation products.

Table 2.2: Correlation coefficient of annual total snowfall between the snow reanalysis snowfall (ensemble median) and snowfall from other precipitation products (ERA5, APHRODITE-2 and MERRA-2). The tile coordinates in the table refer to the lower left corner of each tile.

Tile Coordinates	ERA5	APHRODITE-2	MERRA-2	Average
$(41°N, 77°E)$	0.87	0.45	0.71	0.68
$(38°N, 70°E)$	0.59	0.20	0.52	0.44
$(34°N, 66°E)$	0.87	0.55	0.84	0.76
$(34°N, 75°E)$	0.54	-0.13	0.51	0.31
$(29°N, 82°E)$	0.76	0.80	0.58	0.71
$(27°N, 90°E)$	0.18	0.28	0.69	0.38
$(29°N, 97°E)$	0.73	0.86	0.33	0.64
$(36°N, 85°E)$	0.75	0.21	0.54	0.50
$(38°N, 98°E)$	0.35	0.59	0.37	0.43
Average	0.63	0.42	0.57	0.54

2.3.4 Snowfall Distribution with Elevation

Finally, we investigated the snowfall distribution with elevation in each tile. All the coarse gridded precipitation products (MERRA-2, ERA5 and APHRODITE-2) were bilinearly interpolated to the reanalysis model grid, and downscaled with the reanalysis-derived air temperature to obtain snowfall estimates in each elevation bin (Figure 2.9). The solid lines represent the snowfall distribution from the downscaled MERRA-2 (red) and snow reanalysis (ensemble median, blue) respectively, and the two dashed lines represent the snowfall distribution from the downscaled ERA5 (green) and APHRODITE-2 (black). It should be acknowledged that none of the coarse products are expected to accurately resolve elevational snowfall distributions (beyond large-scale precipitation variations resolved by the coarse grids); the comparison herein is mainly to identify differences in localized elevational snowfall gradients within a tile.

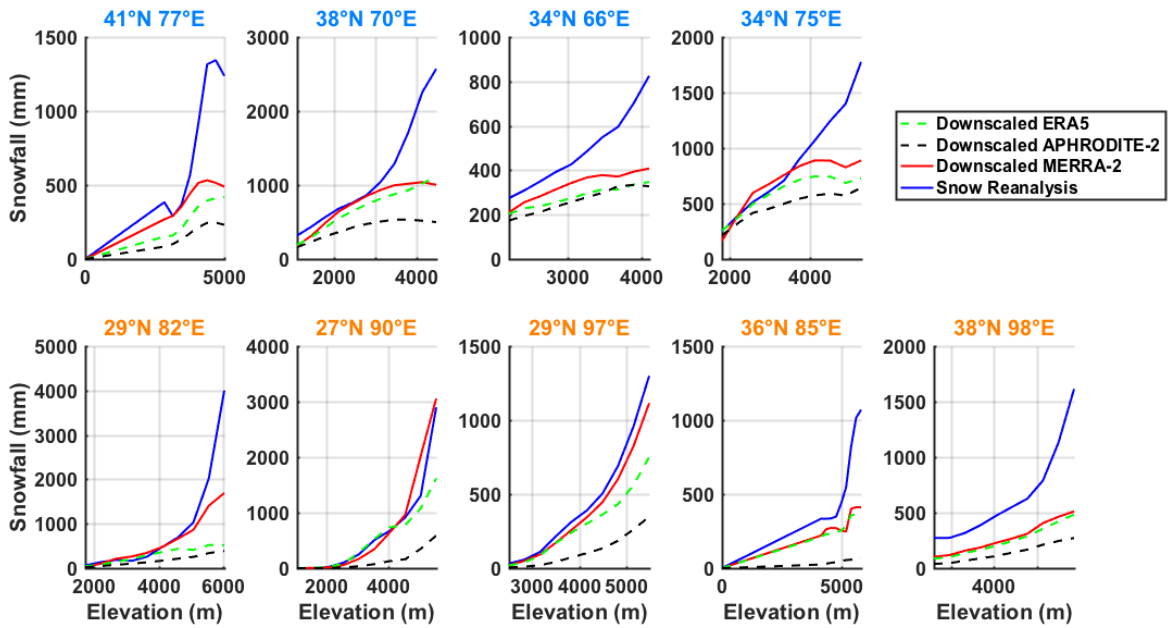

Figure 2.9: Elevational distribution of annual total snowfall climatology (WY 2001-2015) from downscaled ERA5, downscaled APHRODITE-2, and downscaled MERRA-2 vs. the snow reanalysis (ensemble median). Tile labels in blue and orange text represent their locations in the western domain or central-eastern domain respectively.

As expected, the snowfall exhibits positive elevational gradients across all products, where the gradient is highest for the snow reanalysis compared to other products (Figure 2.9). Taking tile $41°N\ 77°E$ as an example, snowfall from the snow reanalysis is 0 mm at the lowest elevations, but rapidly increased to around 1300 mm at the highest elevations (5000 m). For the other products in the same tile, while starting from 0 mm at the lowest elevations, snowfall at the highest elevations only ends up around 500 mm for MERRA-2, 400 mm for ERA5 and 250 mm for APHRODITE-2. The most notable differences in snowfall is observed in the elevation range between 4000 m and 5000 m, where the magnitude of snowfall is comparable at 4000 m, but almost 2~3 times higher in the snow reanalysis than other products at 5000 m. A similar feature is observed in other tiles, where the snow reanalysis shows the largest amount of snowfall in most elevation bins, followed

by MERRA-2, ERA5 and APHRODITE-2. The magnitude of snowfall across all products are comparable at low-mid elevations, but diverge at high elevations, with a mild slope observed in MERRA-2, ERA5 and APHRODITE-2, with a steeper slope observed in the snow reanalysis. Exceptions are two southern tiles ($27°N$ $90°E$, $29°N$ $97°E$) that snowfall estimates are consistent among snow reanalysis, MERRA-2 and ERA5 across all elevation bins, and a steep slope is also observed in the latter two products at the highest elevation ranges. This indicates the potential of bias-correction in snowfall from the snow reanalysis especially at high elevations, where fSCA information exist, but precipitation gauges do not.

Fitted with a linear regression (Table 2.3), the gradient of snowfall against elevation is highest in the snow reanalysis (451 mm/km), followed by MERRA-2 (252 mm/km), ERA5 (174 mm/km) and APHRODITE-2 (91 mm/km) on average. Overall, the snowfall gradients are highest (>300 mm/km) in one western tile ($38°N$ $70°E$), two southern tiles ($29°N$ $82°E, 27°N$ $90°E$), and one north-eastern tile ($38°N$ $98°E$). Specifically, the two southern tiles are strongly affected by the Indian monsoon thereby receiving significant amounts of precipitation in the summer. The phase of summer precipitation is therefore more sensitive to elevation, as lower elevations receive more rainfall and higher elevations receive more snowfall. In the other tiles that are affected by winter westerlies, the phase of winter precipitation may not be as dependent on elevation because of colder winter temperatures. In addition, the magnitude of precipitation brought by the Indian monsoon is much greater than the westerlies (Figure 2.3). Therefore, the southern tiles may still receive significant amounts of snowfall even in summer at the very high elevations, which accounts for the large snowfall gradients in these tiles.

Table 2.3: Snowfall gradients with elevation (mm/km) from the snow reanalysis (ensemble median) and other precipitation products (ERA5, APHRODITE-2 and MERRA-2) fitted with a linear regression. The tile coordinates in the table refer to the lower left corner of each tile.

Tile Coordinates	ERA5	APHRODITE-2	MERRA-2	Snow Reanalysis	Average
(41°N, 77°E)	92	54	112	284	136
(38°N, 70°E)	268	106	258	637	317
(34°N, 66°E)	75	91	98	272	134
(34°N, 75°E)	131	109	186	412	210
(29°N, 82°E)	120	84	363	692	315
(27°N, 90°E)	340	108	587	506	385
(29°N, 97°E)	231	109	342	394	269
(36°N, 85°E)	61	11	67	156	74
(38°N, 98°E)	244	150	259	709	340
Average	174	91	252	451	242

2.4 Conclusions

Using an 'uninformed' prior estimate in a Bayesian snow reanalysis method, we parameterized the snowfall biases and uncertainties in MERRA-2 precipitation over the HMA region. The method was applied over 9 test tiles and spanned the WYs 2001-2015. The posterior scaling factor associated with using MERRA-2 as the nominal precipitation input ($b^{R}_{tile,MERRA2}$) is effectively updated (from the prior uniform distribution) in most tiles featuring seasonal snow, which yields unimodal skewed uncertainty distributions that when fitted using lognormal distributions, exhibited tile-specific mean values ranging from 1.0 – 1.9 and tile-specific CV values ranging from 0.5 - 1.2. One tile in the northeastern Tibetan Plateau is an exception with mean values around 2.5, which is likely indicative of a less robust parameterization due to the fact that intermittent snow plays a more significant role in that tile. By merging the results across tiles, we were able to quantify a global uncertainty model in snowfall using a lognormal distribution with a mean of 1.54 (median of 1.19) and a CV of 0.83. The parameterized distribution indicates that MERRA-2

underestimates snowfall precipitation by ~54% on average (when compared to the posterior reanalysis estimates) with significant uncertainty.

Estimates of the biases and uncertainty in snowfall from other gridded products (ERA5 and APHRODITE-2) were also derived in this study. Compared to the reanalysis snowfall, we found ERA5 and APHRODITE-2 generally, on average, underestimate snowfall by a factor of ~1.78 (with a median scaling factor of 1.42) and ~3.34 (with a median scaling factor of 2.51) respectively over the HMA domain. The snowfall biases in MERRA-2 and ERA5 have similar magnitudes (where ERA5 is slightly larger), while that in APHRODITE-2 are much larger than the other two products, especially in the monsoon-influenced tiles. The biases in all datasets are generally lower in the western tiles compared to those in the central and eastern part of the domain.

In addition to the biases and uncertainties in *b*, we also examined the spatial-temporal distribution of snowfall in the snow reanalysis and other products used in this study. Significant heterogeneity is observed in the snow reanalysis snowfall compared to the downscaled MERRA-2, showing the snow reanalysis effectively downscales the coarse MERRA-2 by leveraging information in the higher-resolution fSCA data observed in each WY and in other model-based fields (i.e. terrain). In terms of annual snowfall time series, snowfall from the snow reanalysis is generally greater than that from MERRA-2, where ERA5 shows similar magnitudes as MERRA-2 and APHRODITE-2 significantly smaller than other products. The temporal correlation of snowfall between snow reanalysis and other products are mostly positive, and the averaged correlation coefficient across all tiles are between 0.42-0.63 for these products. The fact that the correlation is not higher is likely indicative of the impact of other factors (i.e. fSCA measurements) in the temporal variations in the posterior reanalysis estimates. Based on examination of the elevational distribution of snowfall,

we found the snowfall gradients largest in the snow reanalysis followed by MERRA-2, ERA5 and APHRODITE-2.

Overall, this study shows the potential for using satellite snow observations as a constraint on models to infer biases and uncertainties in snowfall precipitation in remote regions and complex terrain where in-situ stations are very scarce. The results indicate that snowfall precipitation is underestimated in most precipitation products, and the biases are higher in the gauge-based precipitation product. One limitation in this study is that the method relies on the seasonal cycle of snow accumulation and ablation captured by fSCA observations to condition snowfall. Therefore, it is expected that the Bayesian update will be more effective in snow-dominated regions that feature a clear seasonal signal, but less effective in regions with intermittent snow. The approach is best suited to estimating high elevation precipitation where snowfall dominates, but likely not very informative of low elevation precipitation where rainfall dominates. In this sense, this effort is complementary to gauge-based estimates, which are expected to perform best in lower elevations where the gauges reside, but may have difficulty extrapolating precipitation information to higher elevations. Results from this work are being used in the development of a snow reanalysis dataset over the full HMA domain. That effort should lead to a more complete picture of snowfall biases and space-time variations across the domain and could be used to further inter-compare products more broadly. Additionally, while this work focused on using MERRA-2 as the baseline input to the snow reanalysis scheme, future work could examine the usage of ERA5 and/or products in combination to more thoroughly represent the uncertainty in precipitation in such domains.

2.5 Bibliography

Andermann, C., Bonnet, S., & Gloaguen, R. (2011). Evaluation of precipitation data sets along the Himalayan front. *Geochemistry, Geophysics, Geosystems*, *12*(7), n/a–n/a. http://doi.org/10.1029/2011GC003513

Anders, A. M., Roe, G. H., Hallet, B., Montgomery, D. R., Finnegan, N. J., & Putkonen, J. (2006). Spatial patterns of precipitation and topography in the Himalaya. *Special Paper of the Geological Society of America*, *398*, 39-53. https://doi.org/10.1130/2006.2398(03)

Bolch, T., Kulkarni, A., Kaab, A., Huggel, C., Paul, F., Cogley, J. G., et al. (2012). The State and Fate of Himalayan Glaciers. *Science*, *336*(6079), 310–314. http://doi.org/10.1126/science.1215828

Bookhagen, B., & Burbank, D. W. (2006). Topography, relief, and TRMM-derived rainfall variations along the Himalaya. *Geophysical Research Letters*, *33*(8), 21. http://doi.org/10.1029/2006GL026037

Bookhagen, B., & Burbank, D. W. (2010). Toward a complete Himalayan hydrological budget: Spatiotemporal distribution of snowmelt and rainfall and their impact on river discharge. *Journal of Geophysical Research*, *115*(F3), 39. http://doi.org/10.1029/2009JF001426

Copernicus Climate Change Service (C3S) (2017): ERA5: Fifth generation of ECMWF atmospheric reanalyses of the global climate . Copernicus Climate Change Service Climate Data Store (CDS), *date of access*. https://cds.climate.copernicus.eu/cdsapp#!/home

Cortés, G., Girotto, M., & Margulis, S. (2016). Snow process estimation over the extratropical Andes using a data assimilation framework integrating MERRA data and Landsat imagery. *Water Resources Research*, *52*(4), 2582–2600. http://doi.org/10.1002/2015WR018376

Cortés, G., & Margulis, S. (2017). Impacts of El Niño and La Niña on interannual snow accumulation in the Andes: Results from a high-resolution 31 year reanalysis. *Geophysical Research Letters*, *44*(13), 6859–6867. http://doi.org/10.1002/2017GL073826

Dee, D. P., Uppala, S. M., Simmons, A. J., Berrisford, P., Poli, P., Kobayashi, S., et al. (2011). The ERA-Interim reanalysis: configuration and performance of the data assimilation system. *Quarterly Journal of the Royal Meteorological Society*, *137*(656), 553–597. http://doi.org/10.1002/qj.828

Durand, M., Molotch, N. P., & Margulis, S. A. (2008). A Bayesian approach to snow water equivalent reconstruction. *Journal of Geophysical Research*, *113*(D20), 872. http://doi.org/10.1029/2008JD009894

Gelaro, R., McCarty, W., Suárez, M. J., Todling, R., Molod, A., Takacs, L., et al. (2017). The Modern-Era Retrospective Analysis for Research and Applications, Version 2 (MERRA-2). *Journal of Climate*, *30*(14), 5419–5454. http://doi.org/10.1175/JCLI-D-16-0758.1

Girotto, M., Margulis, S. A., & Durand, M. (2013). Probabilistic SWE reanalysis as a generalization of deterministic SWE reconstruction techniques. *Hydrological Processes*, *28*(12), 3875–3895. http://doi.org/10.1002/hyp.9887

Girotto, M., Cortés, G., Margulis, S. A., & Durand, M. (2014). Examining spatial and temporal variability in snow water equivalent using a 27 year reanalysis: Kern River watershed, Sierra Nevada. *Water Resources Research*, *50*(8), 6713–6734. http://doi.org/10.1002/2014WR015346

Harris, I., Jones, P. D., Osborn, T. J., & Lister, D. H. (2014). Updated high-resolution grids of monthly climatic observations - the CRU TS3.10 Dataset. *International Journal of Climatology*, *34*(3), 623–642. http://doi.org/10.1002/joc.3711

Huffman, G. J., Bolvin, D. T., Nelkin, E. J., Wolff, D. B., Adler, R. F., Gu, G., et al. (2007). The TRMM Multisatellite Precipitation Analysis (TMPA): Quasi-Global, Multiyear, Combined-Sensor Precipitation Estimates at Fine Scales. *Journal of Hydrometeorology*, *8*(1), 38–55. http://doi.org/10.1175/JHM560.1

Hussain, S., Song, X., Ren, G., Hussain, I., Han, D., & Zaman, M. H. (2017). Evaluation of gridded precipitation data in the Hindu Kush–Karakoram–Himalaya mountainous area. *Hydrological Sciences Journal*, *62*(14), 2393–2405. http://doi.org/10.1080/02626667.2017.1384548

Immerzeel, W. W., Wanders, N., Lutz, A. F., Shea, J. M., & Bierkens, M. F. P. (2015). Reconciling high-altitude precipitation in the upper Indus basin with glacier mass balances and runoff. *Hydrology and Earth System Sciences*, *19*(11), 4673–4687. https://doi.org/10.5194/hess-19-4673-2015

Khan, A., & Koch, M. (2018). Correction and Informed Regionalization of Precipitation Data in a High Mountainous Region (Upper Indus Basin) and Its Effect on SWAT-Modelled Discharge. *Water*, *10*(11), 1557–23. http://doi.org/10.3390/w10111557

Khan, A., Koch, M., & Chinchilla, K. (2018). Evaluation of Gridded Multi-Satellite Precipitation Estimation (TRMM-3B42-V7) Performance in the Upper Indus Basin (UIB). *Climate*, *6*(3), 76–17. http://doi.org/10.3390/cli6030076

Lehner, B., Verdin, K., Jarvis, A. (2006): HydroSHEDS Technical Documentation. World Wildlife Fund US, Washington, DC. Available at http://hydrosheds.cr.usgs.gov.

Margulis, S. A., Girotto, M., Cortés, G., & Durand, M. (2015). A Particle Batch Smoother Approach to Snow Water Equivalent Estimation. *Journal of Hydrometeorology*, *16*(4), 1752–1772. http://doi.org/10.1175/JHM-D-14-0177.1

Margulis, S. A., Cortés, G., Girotto, M., & Durand, M. (2016). A Landsat-Era Sierra Nevada Snow Reanalysis (1985–2015). *Journal of Hydrometeorology*, *17*(4), 1203–1221. http://doi.org/10.1175/JHM-D-15-0177.1

Maussion, F., Scherer, D., Mölg, T., Collier, E., Curio, J., & Finkelnburg, R. (2014). Precipitation Seasonality and Variability over the Tibetan Plateau as Resolved by the High Asia Reanalysis*. *Journal of Climate*, *27*(5), 1910–1927. http://doi.org/10.1175/JCLI-D-13-00282.1

Palazzi, E., Hardenberg, von, J., & Provenzale, A. (2013). Precipitation in the Hindu-Kush Karakoram Himalaya: Observations and future scenarios. *Journal of Geophysical Research: Atmospheres*, *118*(1), 85–100. http://doi.org/10.1029/2012JD018697

Rienecker, M. M., Suárez, M. J., Gelaro, R., Todling, R., Bacmeister, J., Liu, E., et al. (2011). MERRA: NASA's Modern-Era Retrospective Analysis for Research and Applications. *Journal of Climate*, *24*(14), 3624–3648. http://doi.org/10.1175/JCLI-D-11-00015.1

Song, C., Huang, B., Ke, L., & Ye, Q. (2016). Precipitation variability in High Mountain Asia from multiple datasets and implication for water balance analysis in large lake basins. *Global and Planetary Change*, *145*, 20–29.

Tahir, A. A., Chevallier, P., Arnaud, Y., & Ahmad, B. (2011). Snow cover dynamics and hydrological regime of the Hunza River basin, Karakoram Range, Northern Pakistan. *Hydrology and Earth System Sciences*, *15*(7), 2275–2290.

Viste, E., & Sorteberg, A. (2015). Snowfall in the Himalayas: an uncertain future from a little-known past. *The Cryosphere*, *9*(3), 1147–1167.

Winiger, M., Gumpert, M., & Yamout, H. (2005). Karakorum-Hindukush-western Himalaya: assessing high-altitude water resources. *Hydrological Processes*, *19*(12), 2329–2338. http://doi.org/10.1002/hyp.5887

Wortmann, M., Bolch, T., Menz, C., Tong, J., & Krysanova, V. (2018). Comparison and Correction of High-Mountain Precipitation Data Based on Glacio-Hydrological Modeling in the Tarim River Headwaters (High Asia). *Journal of Hydrometeorology*, *19*(5), 777–801. http://doi.org/10.1175/JHM-D-17-0106.1

Xia, Y., Mitchell, K., Ek, M., Sheffield, J., Cosgrove, B., Wood, E., et al. (2012). Continental-scale water and energy flux analysis and validation for the North American Land Data Assimilation System project phase 2 (NLDAS-2): 1. Intercomparison and application of model products. *Journal of Geophysical Research*, *117*(D3). http://doi.org/10.1029/2011JD016048

Yatagai, A., Kamiguchi, K., Arakawa, O., Hamada, A., Yasutomi, N., & Kitoh, A. (2012). APHRODITE: Constructing a Long-Term Daily Gridded Precipitation Dataset for Asia Based on a Dense Network of Rain Gauges. *Bulletin of the American Meteorological Society*, *93*(9), 1401–1415. http://doi.org/10.1175/BAMS-D-11-00122.1

Zhou, Y., McLaughlin, D., & Entekhabi, D. (2006). Assessing the Performance of the Ensemble Kalman Filter for Land Surface Data Assimilation. *Mon. Wea. Rev.*, *134*(8), 2128–2142. http://doi.org/10.1175/MWR3153.1

CHAPTER 3

Spatiotemporal distribution of seasonal snow water equivalent in High-Mountain Asia from an 18-year Landsat-MODIS era snow reanalysis dataset

Seasonal snowpack is an essential component in the hydrological cycle and plays a significant role in supplying water resources to downstream users. Yet the snow water equivalent (SWE) in seasonal snowpacks, and its space-time variation, remains highly uncertain, especially over mountainous areas with complex terrain and sparse observations, such as in High-Mountain Asia (HMA). In this work, we assessed the spatiotemporal distribution of seasonal SWE, obtained from a new 18-year HMA Snow Reanalysis (HMASR) dataset, as part of the recent NASA High-Mountain Asia Team (HiMAT) effort. A Bayesian snow reanalysis scheme previously developed to assimilate satellite derived fractional snow-covered area (fSCA) products from Landsat and MODIS platforms has been applied to develop the HMASR dataset (at a spatial resolution of 16 arc-second (~500 m) and daily temporal resolution) over the joint Landsat-MODIS period covering Water Years (WYs) 2000-2017.

Based on the results, the HMA-wide total SWE volume is found to be around 163 km^3 on average and ranges from 114 km^3 (WY2001) to 227 km^3 (WY2005) when assessed over 18 WYs. The most abundant snowpacks are found in the northwestern basins (e.g. Indus, Syr Darya and Amu Darya) that are mainly affected by the westerlies, accounting for around 66% of total seasonal SWE volume. Seasonal snowpack in HMA is depicted by snow accumulating through October to March and April, typically peaking around April and depleting in July-October, with variations across basins and WYs. When examining the elevational distribution over the HMA domain,

seasonal SWE volume peaks at mid-elevations (around 3500 m), with over 50% of the volume stored above 3500 m. Above-average amounts of precipitation causes significant overall increase in SWE volumes across all elevations; while an increase in air temperature (~ 1.5 K) from cooler to normal conditions leads to an redistribution in snow storage from lower elevations to mid elevations.

This work brings new insight into understanding the climatology and variability of seasonal snowpack over HMA, with the regional snow reanalysis constrained by remote sensing data, providing a new reference dataset for future studies of seasonal snow and how it contributes to the water cycle and climate over the HMA region.

3.1 Introduction

The High-Mountain Asia (HMA) region consists of the major mountain ranges and headwaters of the largest rivers in Asia. It features extremely high elevation, complex topography and significant glacier and snow cover. In HMA, glacier melt and snowmelt are vital to the hydrological cycle and water supply, as they feed the major regional rivers with over one billion people living downstream (Barnett et al., 2005; Bookhagen and Burbank, 2010; Immerzeel et al., 2010; Immerzeel and Bierkens, 2012; Lutz et al., 2014; Armstrong et al., 2019; Scott et al., 2019; Immerzeel et al., 2020).

Even though both seasonal snow and glaciers are crucial to hydrology and water availability, seasonal snow has arguably received less attention than glaciers in the HMA region. Many studies have addressed the status and changes in glaciers over HMA (e.g. Bolch et al., 2012; Kääb et al., 2012; Sorg et al., 2012; Yao et al., 2012; Lutz et al., 2014; Bolch et al., 2019; Rounce et al., 2020; Shean et al, 2020). For seasonal snow, previous studies have examined the snow extent (e.g. Dahe et al., 2006; Pu et al., 2007; Immerzeel et al., 2009; Tahir et al., 2011; Basang et al., 2017; Wang

et al., 2017; Notarnicola 2020), or snow mass and snow depth (e.g. Dahe et al., 2006; Che et al., 2008; Terzago et al., 2014; Dai et al., 2017; Stigter et al., 2017; Smith and Bookhagen, 2018. 2020; Ahmad et al., 2019; Kirkham et al., 2019; Xue et al., 2019; Bair et al., 2018, 2020, 2021). In the current literature involving seasonal snow, most of the studies have focused on snow covered area (or extent, which is readily available from satellite-borne remote sensing) instead of snow mass, or have been applied at relatively localized scales (e.g. individual small to moderate sized basins) or coarse scales (e.g. above 1 km) over larger scales. The seasonal snow water storage and its spatiotemporal distribution across HMA are highly uncertain, primarily due to the lack of in situ observations and fine-scale (e.g. < 1 km) snow water equivalent (SWE) datasets over this large domain (Takala et al., 2011; Kirkham et al., 2019). In fact, accurately estimating SWE at such scales remains a great challenge worldwide, and it is even more difficult in mountainous regions due to the terrain complexity (Lettenmaier et al., 2015; Dozier et al., 2016; Bormann et al., 2018). In situ measurements are usually expensive and difficult to install and maintain in HMA and are mostly located in low-lying valleys, thus resulting in a sparse and potentially nonrepresentative network (Winiger et al., 2005; Palazzi et al., 2013; Dozier et al., 2016; Kirkham et al., 2019). In recent decades, satellite observations can provide large-scale estimates of some snowpack properties. However, most of these measured properties, such as snow-covered area (SCA) based on visible and near infrared bands (e.g. Dozier, 1989, Hall et al., 2002, Painter et al., 2009), are only indirectly related to snow mass. While SWE and snow depth can be directly estimated from passive microwave sensors (using retrieval algorithms based on the brightness temperature; e.g. Chang et al., 1987), these estimates are at coarse spatial resolution (e.g. 25 km), and are generally negatively biased in deep snowpacks (Takala et al., 2011; Dozier et al, 2016). Recent applications

of C-band synthetic aperture radar (SAR) techniques show promise for snow depth retrieval (Lievens et al., 2019) but are available only over recent years and do not directly provide SWE.

Global atmospheric reanalysis products provide another approach to large-scale SWE estimates as by-products of their land surface schemes. Examples include the Global Land Data Assimilation System (GLDAS, Rodell et al., 2004), Modern-Era Retrospective analysis for Research and Applications (MERRA, Rienecker et al., 2011; MERRA-2, Gelaro et al., 2017), European Centre for Medium-Range Weather Forecasts (ECMWF) Re-Analysis products (ERA-Interim, Dee et al., 2011; ERA5, Hersbach et al., 2020), High Asia Refined analysis (HAR, Maussion et al., 2011; 2014), Japanese 55-year Reanalysis (JRA-55; Kobayashi et al., 2015), and others. SWE estimates in these datasets are found to be generally consistent in their interannual and seasonal variations, but can differ significantly in their magnitudes when evaluated over different regions (Mudryk et al., 2015; Wrzesien et al., 2019), where the uncertainties come from different land surface models and meteorological inputs (Mudryk et al., 2015; Mortimer et al., 2020; Kim et al., 2021). In addition, most reanalysis datasets are not specifically designed for SWE estimation, and only a few of them (e.g. ERA5 and JRA55) assimilate snow observations (including in-situ and remote sensing) in HMA. Bian et al. (2019) found many reanalysis datasets overestimate SWE compared to ground observations in the Tibetan Plateau, although part of the differences may come from inconsistent spatial resolution and elevations between in situ and gridded datasets. The performance of these large-scale reanalysis datasets over the full HMA domain has not been fully assessed due to the sparse and uneven in situ station network.

Recent works have contributed to the development of SWE (or snow depth) estimates covering the HMA region based on passive microwave (e.g. Talaka et al., 2011; Smith and Bookhagen, 2016; Dai et al., 2017; Pulliainen et al., 2020) or active microwave measurements (Lievens et al.,

2019), with machine learning approaches employed to improve the accuracy in SWE estimation (e.g. Ahmad et al., 2019). Alternatively, satellite observed snow covered area products can also provide valuable information in SWE estimation. For example, fractional snow-covered area (fSCA) products are used in SWE reconstruction methods to improve the estimates of SWE over Indus and Amu Darya, by calculating snowmelt backward from melt-out to peak SWE timing using satellite-observed snow disappearance rates (Bair et al. 2018; 2020). In addition, data assimilation (DA) approaches that explicitly merged snow observations with modeling are effective in providing more realistic SWE estimates and reducing SWE uncertainties especially over the mountains (Xue et al. 2019; Largeron et al., 2020): both JRA-55 and ERA5 products assimilate ground snow depth and satellite retrieved snow cover observations; GlobSnow (Talaka et al., 2011; Pulliainen et al., 2020) products assimilate passive microwave retrieved SWE along with ground snow depth observations to provide SWE and snow extent estimates, while mountain areas with high terrain complexity are masked out. These are promising approaches to improve the accuracy in SWE estimates over HMA, yet currently there is still a need for large scale SWE datasets at higher resolution, over a longer period and covering mountainous areas in this region.

To better understand the spatiotemporal pattern and variability in seasonal snowpack over HMA, the so-called High-Mountain Asia Snow Reanalysis (HMASR; Liu et al., 2021) dataset is used herein to characterize the seasonal snow climatology and variability over HMA. The dataset covers the joint Landsat-MODIS era between Water Years (WYs) 2000 to 2017 (which will be extended to present in later versions) and was developed as part of the NASA High-Mountain Asia Team (HiMAT) activities. HiMAT is a multi-investigator effort in developing new datasets to understand cryosphere variability over HMA (Osmanoglu et al., 2017). The HMASR dataset provides daily estimates of SWE, fSCA and other snow variables, at a 16 arc-second (~500 m) resolution. SWE

estimates are derived by assimilating fSCA from Landsat and MODIS platforms using a previously developed snow reanalysis framework (Margulis et al., 2019), where the method has been shown in previous applications to provide realistic SWE estimates over mountainous domains in the Sierra Nevada (Margulis et al., 2016) and Andes (Cortés and Margulis, 2017). The HMASR aims to fill the spatiotemporal gaps in existing SWE datasets and allow for better characterization of the distribution and changes in seasonal snow storage, and provide insights into the hydrologic cycle and water availability over HMA. Using this dataset, the spatial distribution of SWE climatology is examined at annual and seasonal scales over the HMA region, covering the highest mountain ranges and the Tibetan Plateau in Asia. Integrated SWE volumes over the full HMA domain and over the major river basins (e.g., Syr Darya, Amu Darya, Indus, Ganges-Brahmaputra, Yangtze, Yellow), and their variation with elevation, are also quantified in this work. The following scientific questions are addressed herein:

1) How is seasonal snow distributed spatially across the major watersheds of HMA?
2) What is the seasonal and interannual variability in amount of snow storage over HMA?
3) How is the amount of snow distributed across elevation, and how does it vary under different climate conditions?

3.2 Data and method

This section describes the data and methods used in this study. Section 3.2.1 introduces the study domain, including the major river basins and mountain ranges in the region. Section 3.2.2 and 3.2.3 provide a brief description of the reanalysis method, input data and models used in the development of the HMASR. Finally, a non-seasonal snow and ice mask applied to mask out semi-permanent snow and ice for the assessment of seasonal snow is explained in Section 3.2.4.

3.2.1 HMA domain

The HMA domain used in this work is bounded from 27° N to 45° N, and from 60° E to 105° E (Figure 3.1), covering the highest mountain ranges and plateaus (Tien Shan, Pamir, Hindu Kush, Karakoram, Himalayas, and Tibetan Plateau), as well as the headwaters of the main river basins (Syr Darya, Amu Darya, Indus, Ganges-Brahmaputra, Yangtze, and Yellow). Winter westerlies and the summer monsoon are the major moisture sources in this region, significantly influencing the spatiotemporal patterns in snowfall and glacier mass balance. More specifically, the northern and western HMA is dominated by westerlies and receives abundant winter snowfall, while the southern and eastern HMA is dominated by the Indian monsoon from June to September and receives a considerable amount of summer snowfall; the eastern edges of HMA are affected by the East Asia monsoon but with limited impact (Bookhagen and Burbank 2010; Yao et al., 2012; Bolch et al., 2019). Note that in HMASR, outputs are provided for each regular 1° by 1° latitude-longitude tile (within which a regular computational grid of 16 arc-second is used), and tiles with a tile-averaged elevation above 1500 m were selected and processed in the dataset (Figure 3.1). This tile-average threshold (1500 m) was chosen conservatively to capture the vast majority of seasonal mountain snow over HMA, avoid running a large number of tiles with negligible snow, and reduce the computational load in product development. We acknowledge this threshold might exclude snow in some areas of the domain (e.g. northern HMA) and anticipate this threshold to be relaxed or removed in future versions of this product.

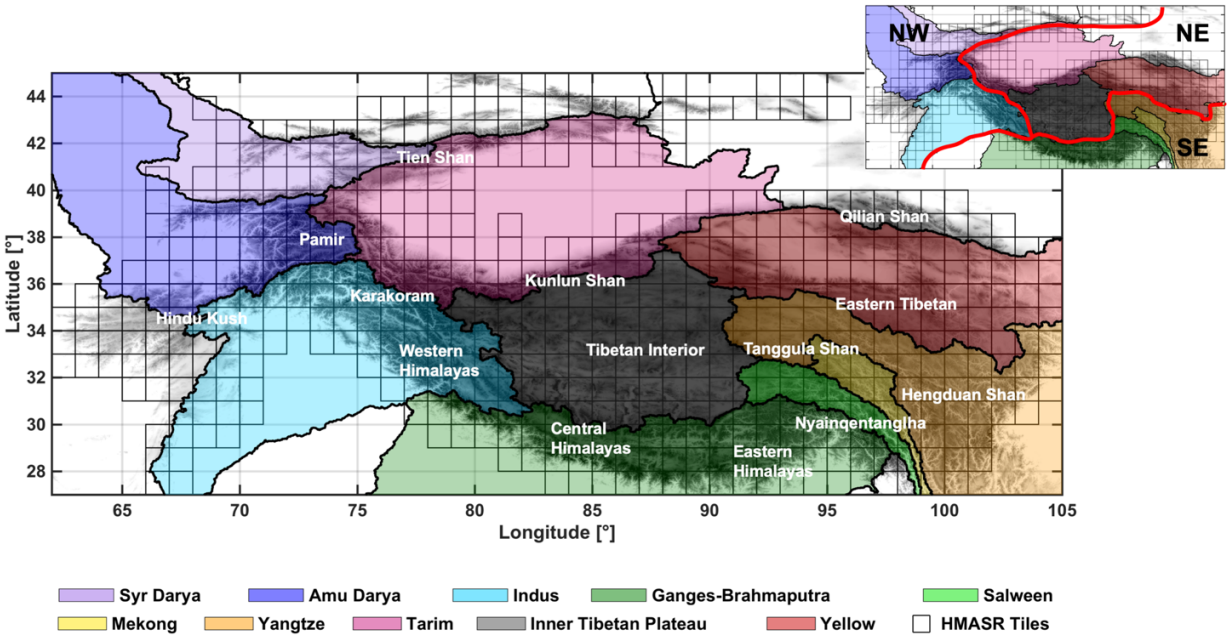

Figure 3.1: Map of HMA domain with HMASR tiles marked with black boxes. Major watersheds are delineated and colored on the map based on HydroSHEDS (Lehner et al., 2008). Major mountain ranges are labeled with reference to Bolch et al. (2019). A division of the HMA domain into Northwestern (NW), Northeastern (NE) and Southeastern (SE) sub-regions, which are used for descriptive purposes in this study, is shown in the inset.

For convenience in presenting results herein, the HMA domain was divided into three large subregions, namely the Northwestern (NW), Southeastern (SE) and Northeastern (NE) subregions (Figure 3.1). Major river basins are identified in each subregion, namely those located in NW (Syr Darya, Amu Darya and Indus), in SE (Ganges-Brahmaputra, Salween, Mekong and Yangtze), and in NE (Tarim, Inner Tibetan Plateau and Yellow). Similarly, the major mountain ranges are also identified in each subregion, namely those located in the NW (e.g. Tien Shan, Pamir, Hindu Kush, Karakoram, western Himalayas), SE (e.g. central and eastern Himalayas, Nyainqentanglha, Tanggula Shan and Hengduan Shan), and NE (e.g. Kunlun Shan, Tibetan Interior, Eastern Tibetan and Qilian Shan), and are labelled in Figure 3.1.

3.2.2 Snow reanalysis scheme

A previously developed snow reanalysis methodology (Margulis et al., 2019) is employed in deriving the HMASR. For brevity, only the key details are repeated here. Prior model estimates are obtained via the coupled Simplified Simple Biosphere model, version 3 (SSiB3; Sun and Xue, 2001; Xue et al., 2003) and the Liston (2004) snow depletion curve (SDC). The SSiB3 model is used as the land surface model (LSM) in this work, which has three snow layers with vegetation canopy and soil representations. It requires hourly inputs of forcing data (e.g. precipitation, air temperature, radiation, wind speed, humidity and pressure) and static inputs (e.g. topography, land cover, vegetation and soil type), with more details clarified in Section 3.2.3.1. The SSiB3 model provides the basic mass and energy fluxes for the snowpack based on meteorological inputs and physiographic characteristics. These fluxes are used with the Liston SDC to derive estimates of grid-averaged SWE and fSCA. Specifically, the Liston SDC assumes that the subgrid distribution of SWE follows a lognormal distribution, and is a function of grid-averaged SWE, melt, and a parameter of subgrid coefficient of variation. The SDC yields the prediction of fSCA that is compared with satellite observed fSCA and serves as the constraint in the data assimilation.

As done in many data assimilation methods, an ensemble approach is used in the snow reanalysis scheme, whereby the model generates prior estimates of snow states (i.e. SWE, snow depth, fSCA, etc.) with postulated uncertainties. Meteorological forcing inputs are bias-corrected, downscaled to the modeling grid (16 arc-second) and perturbed with uncertainty in the ensemble approach, using the methods described in Durand et al. (2008) and Girotto et al. (2014). To constrain the prior snow estimates on the remotely sensed fSCA observations, a Bayesian update is performed using the Particle Batch Smoother (PBS; Margulis et al., 2015; Margulis et al., 2019) approach. Posterior snow estimates are obtained in this update step, by more heavily weighting ensemble

members that are more consistent with the batch of observed fSCA in a given water year using a Bayesian likelihood function that accounts for model-measurement misfit and measurement error. It is worthwhile to note that, the posterior ensemble mean, median and spread (or other statistics) can be obtained via the Bayesian update step. Herein, the posterior ensemble median values of SWE are described when assessing the SWE over HMA. Details of the PBS methods are described in Margulis et al. (2015; 2019), and more details on fSCA observations are provided in Section 3.2.3.2.

The lack of in situ SWE data over HMA prevents a thorough verification of the HMASR. However, previous applications of the snow reanalysis method in similarly complex terrain in the Sierra Nevada of the Western U.S. and the South American central Andes thoroughly compared reanalysis estimates vs. in situ and airborne-derived SWE data. Performance in both domains were positive relative to in situ data with values of mean error, root-mean-squared error and correlation coefficients of: ~ 3 cm, 13 cm and 0.95 for the Sierra Nevada (Margulis et al., 2016) and ~ 1 cm, 29 cm and 0.73 for the Andes (Cortés and Margulis, 2017), respectively. In Margulis et al. (2019), comparison with the Airborne Snow Observatory (ASO) SWE data in Tuolumne in the Sierra Nevada yielded similar results (mean error, root-mean-squared error, and correlation coefficients of ~ 5 cm, 23 cm, and 0.84). Here we provide the caveat that performance of the method may be degraded in parts of the HMA region due to the frequent cloud obscuring issues (see more details in Section 3.2.3.2), compared to previous work in the Sierra Nevada or Andes.

3.2.3 Input data acquisition and processing

3.2.3.1 Meteorological, topographic and land cover data

In HMASR, the prior surface meteorological inputs were obtained from MERRA-2 at its raw resolution (0.5° by 0.625° latitude–longitude), including precipitation, air temperature, solar

radiation, specific humidity, surface pressure and wind speed. The uncertainty models and their parameters used to perform bias-correction and uncertainty perturbation are specified in Margulis et al. (2019) for the HMA region, except that prior ensemble precipitation is perturbed by a lognormal distribution with mean of 1.54 and coefficient of variation (CV) of 0.83 based on the results from Liu and Margulis (2019).

Digital elevation model (DEM) data were obtained from the Shuttle Radar Topography Mission (SRTM, http://www2.jpl.nasa.gov/srtm/) 1 arc-second product, and aggregated to 16 arc-second (~500 m) resolution. Gaps in DEM data were filled by the Advanced Spaceborne Thermal Emission and Reflection Radiometer (ASTER) Global Digital Elevation Model (GDEM, version 2) 1 arc-second product (https://asterweb.jpl.nasa.gov/). Land cover data were obtained from the AVHRR global land cover classification dataset (Hansen et al., 2000). Forest cover information was obtained from the Tree Canopy Cover (TCC) product containing the Landsat Vegetation Continuous Fields (https://lcluc.umd.edu/metadata/global-30m-landsat-tree-canopy-version-4; Sexton et al., 2013).

3.2.3.2 fSCA data

The fSCA observations used to condition prior snow estimates were retrieved from Landsat and MODIS platforms, for their joint period of WYs 2000 to 2017 (e.g. where WY2000 corresponds to October 1, 1999 - September 30, 2000). The (nadir-viewing) Landsat-based fSCA data were obtained from Landsat 5, 7 and 8 satellites, retrieved using a spectral unmixing algorithm (Painter et al., 2003; Cortés et al., 2014), available at 30 m and every 16 days (excluding cloudy days). The (nadir- and off-nadir-viewing) MODIS-based fSCA data were obtained from the MODIS Snow Covered Area and Grain size (MODSCAG) product (Painter et al., 2009), available daily at 500

m, with a viewing angle between 0° and 55°. Jointly assimilating fSCA from both platforms provides more measurements to compensate for cloud contamination in HMA.

Cloud screening and viewing angle screening were performed as illustrated in Margulis et al. (2019), and here we only clarify the key steps for brevity. Specifically, for Landsat, any image with a diagnosed cloud cover fraction of greater than 40% is excluded entirely. For MODSCAG, only 'near-nadir' pixels within an image are included and, of those, any image with a diagnosed cloud cover fraction of greater than 10% is excluded entirely. This subset of Landsat and MODSCAG images for inclusion therefore uses a conservative screening meant to exclude significantly cloud-contaminated tiles. This does not prevent errors of omission/commission in cloud/snow identification, but is meant to mitigate cloud impacts by not including those deemed significantly cloudy. It should also be noted that the snow reanalysis method used herein is less susceptible to errors of omission/commission when compared to SWE reconstruction methods (e.g. Bair et al., 2020) that interpolate between fSCA measurements to estimate ablation rates. Instead, the snow reanalysis fitting of fSCA measurements is more akin to a least-squares type fit where measurement errors are accounted for in the framework. This mitigates the propagation of errors of omission/commission compared to SWE reconstruction techniques. For images that passed through the cloud/viewing angle screening, cloudy pixels within each image were further excluded through internal cloud masks. After screening, both Landsat and MODSCAG images were aggregated to the same modeling resolution (16 arc-second).

No large systematic differences were seen when examining fSCA across different Landsat sensors, while substantial differences were found in same-day fSCA images between Landsat and MODSCAG (after screening and aggregation). To reconcile the inconsistency between products, a cumulative distribution function (CDF)-matching method was applied pixel-wise to statistically

match MODSCAG images with Landsat images. Based on the analysis in Margulis et al. (2019), we specify a measurement error standard deviation (10% of Landsat fSCA; 15% of CDF-matched MODSCAG fSCA) in the reanalysis to represent retrieval error/uncertainty.

It is worthwhile to note that the fSCA data availability is significantly affected by cloud contamination in some areas of HMA region, especially during the monsoon season (June-September) where fSCA measurements are limited over regions such as the Himalayas (Figure 3.2). The lack of abundant fSCA data can be a potential limitation in assimilating fSCA observations for these monsoon-affected regions, and therefore leads to higher uncertainty and less constrained posterior SWE estimates (i.e. where in the limit of no available observations, the posterior will, by construct, equal the prior estimate).

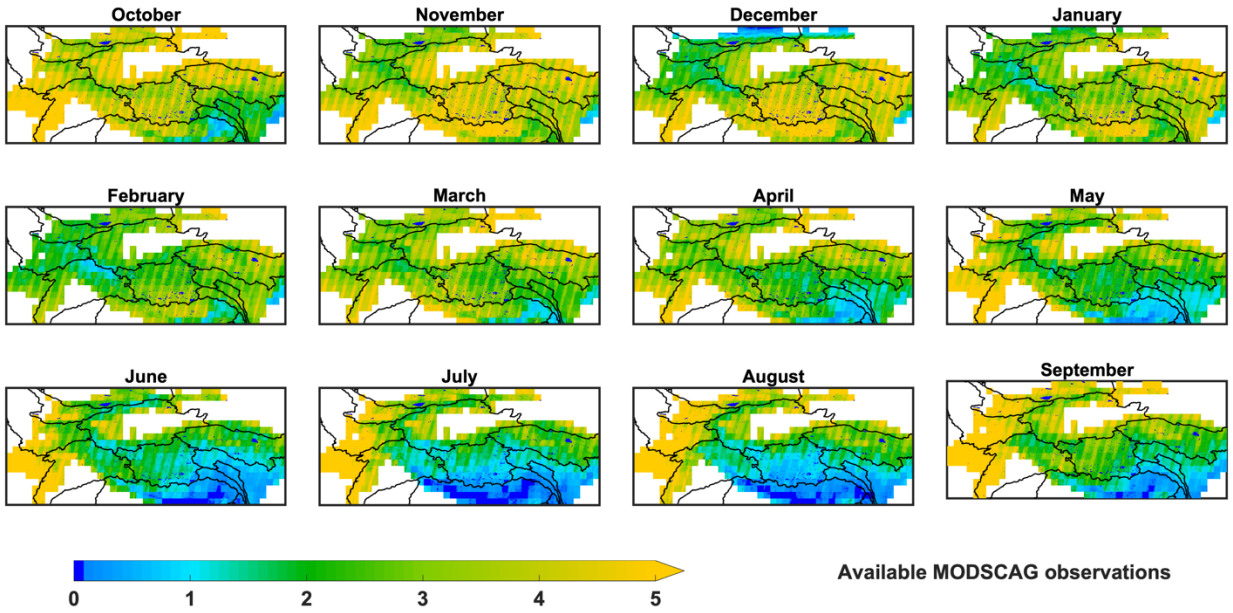

Figure 3.2: Monthly total number of available (near-nadir) MODSCAG measurements averaged over 18 years, with cloud and viewing angle screening. Landsat measurements supplement these MODIS-derived measurements. The dark blue color is used to distinguish pixels with zero MODSCAG measurements.

3.2.4 Non-seasonal snow and ice mask

A significant fraction of HMA is covered by glacier or semi-permanent snow owing to its extremely high elevation. Thus, it is important to distinguish seasonal vs. non-seasonal snow over land or glacier surfaces. In particular, the reanalysis method used in the development of the HMASR is best suited for seasonal snow characterization, because it relies on the signal between fSCA depletion time series and SWE via the LSM-SDC model. Hence, those pixels where there is not a full melt-out of snow are expected to be potentially erroneous. So, while estimates are generated at all pixels in the domain, the aim to focus on seasonal snow requires masking out semi-permanent snow and ice. Glacier inventories from the Global Land Ice Measurements from Space (GLIMS; Raup et al., 2007) and the Randolph Glacier Inventory (RGI; Pfeffer et al., 2014; RGI Consortium, 2017) have been employed in previous studies to exclude glaciers from snow modeling domains (e.g. Wrzesien et al, 2019, Smith and Bookhagen et al., 2018). Other studies such as Mudryk et al. (2015) and Mortimer et al. (2020) excluded glaciers based on estimates from the MERRA land fraction mask. Armstrong et al. (2019) applied the MODIS Persistent Ice (MODICE; Painter et al., 2012) algorithm to derive a minimum snow and ice mask based on the MODSCAG product, and used it to distinguish seasonal snow from glaciers or persistent snow.

Herein a combination method was used to exclude the non-seasonal snow and ice pixels in HMASR, based on: 1) a glacier mask derived from GLIMS to identify glacierized pixels and 2) a persistent snow mask derived from the HMASR dataset itself. We acknowledge that RGI dataset may be more appropriate to use than GLIMS, as it obtains glacier outlines around 2000 while GLIMS obtains those from a larger date range. To be more specific on the second mask, pixels with a significant amount of persistent snow were identified, by comparing the annual minimum SWE at a particular pixel to its annual maximum SWE in each year. If the minimum SWE exceeds

10% of the maximum SWE for more than once out of the 18 years, the pixel is considered to be a persistent snow pixel to be masked out in the computation of seasonal snow estimates. The derived glacier and persistent snow masks are combined into a non-seasonal snow and ice mask, which is applied when presenting the spatiotemporal patterns of seasonal SWE in the following section.

3.3 Results and discussion

The HMASR dataset is designed to provide a reliable and consistent SWE product that can be used for assessing the spatiotemporal distribution of seasonal SWE over the recent remote sensing record. To present an overall assessment of seasonal snowpack variability in the HMA region using the HMASR dataset, the results are organized as follows: 1) the spatial distribution of seasonal snowpack climatology, at annual peak and seasonal scales; 2) the temporal distribution of seasonal snowpack volume at basin and domain-wide scales; 3) the elevational distribution of seasonal snowpack storage at HMA-wide and basin scales.

3.3.1 Spatial distribution of seasonal SWE climatology

The spatial distribution of SWE is valuable in assessing the regional water storage. Given the strong seasonal signature of snowpack processes over much of the domain, the pixel-wise peak SWE is a useful metric to quantify the distribution of the maximum amount of snow water mass held in the seasonal snowpack within a given water year. Hence, the spatial distribution of peak SWE (Section 3.3.1.1) and the associated timing (Section 3.3.1.2) are examined in this section, with seasonal evolution of SWE averaged over fall, winter, spring and summer also assessed (Section 3.3.1.3).

3.3.1.1 Peak seasonal SWE climatology

The climatology (18-year average) of pixel-wise peak SWE over the HMA region is depicted in Figure 3.3, where Figure 3.3a presents only the results for seasonal snow pixels (where non-

seasonal snow and ice pixels have been masked out). Figure 3.3b presents the results for all pixels for illustration (where significantly higher amounts of SWE shows up in non-seasonal snow and ice mask pixels, corresponding to glaciers or permanent snow), where the non-seasonal snow mask covers ~4.7% of the domain area. The non-seasonal SWE values (Figure 3.3b) are expected to be unreliable because the initial conditions for SWE at those locations at the beginning of the dataset are unknown and the lack of full melt-out makes the relationship between fSCA depletion and peak SWE much less direct.

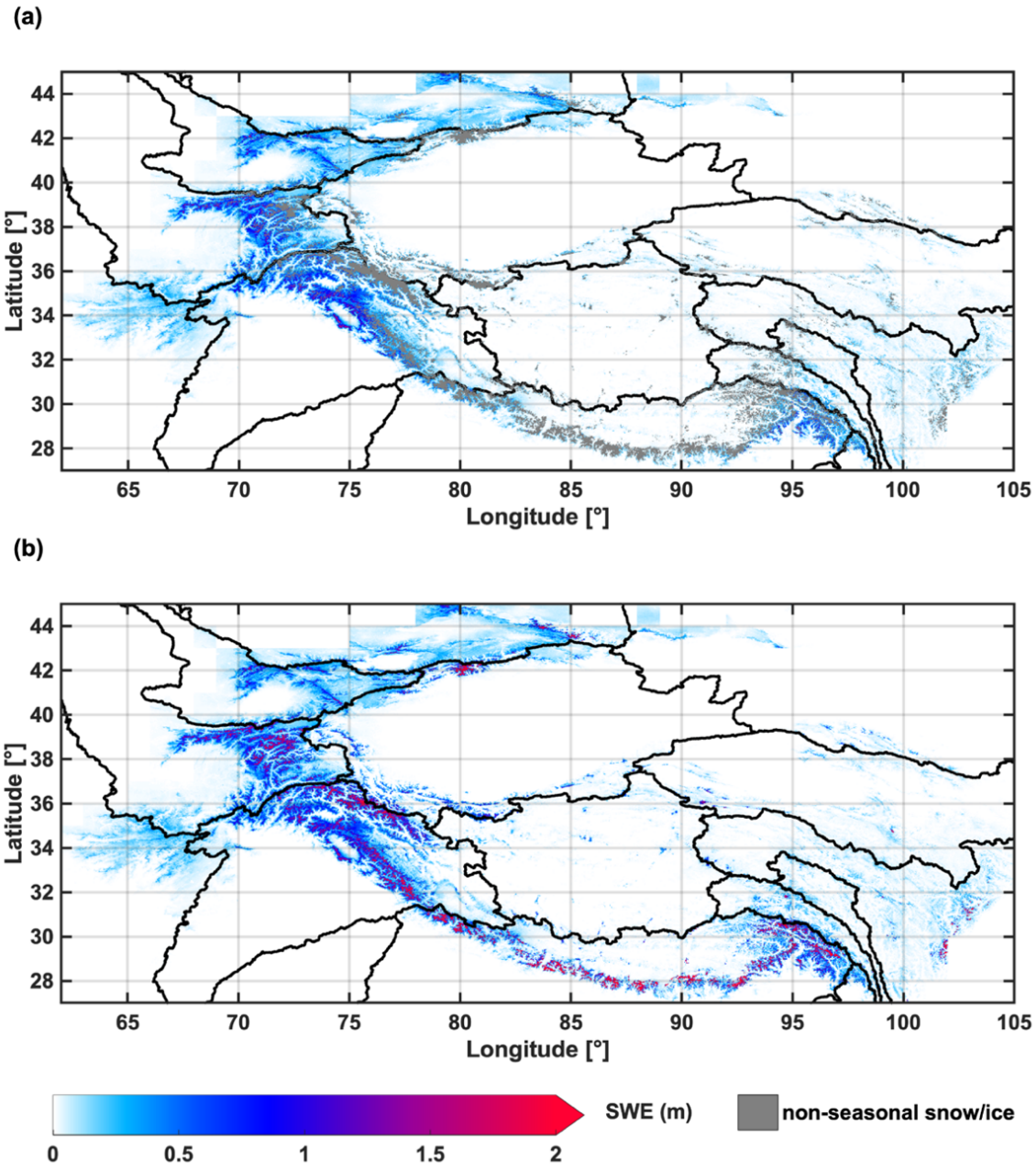

Figure 3.3: (a): Map of pixel-wise peak seasonal SWE climatology, with non-seasonal snow and ice pixels masked out (grey). (b): Map of pixel-wise peak seasonal SWE climatology, without masking of non-seasonal snow and ice pixels for reference.

In general, seasonal snow is most abundant in the NW region that is directly exposed to westerlies (Figure 3.3a). Among the northwestern mountain ranges, the highest climatological peak SWE values are found in Pamir, Karakoram and the western Himalayas, with more than 1 m of peak SWE estimated. A significant amount of peak SWE is also estimated in Tien Shan and Hindu Kush, showing peak SWE values of 1 m or less in Tien Shan, and 0.5 m or less in Hindu Kush in general (Figure 3.3a). The estimates of peak SWE values in Hindu Kush are consistent with measurements and SWE reconstruction estimates from Salang Pass in Afghanistan (35N, 69E, elevation 3366 m) that has records of snow (Bair et al., 2018). The non-seasonal snow and ice is most notable in Karakoram but also evident in a few locations over the Pamir, Tien Shan and western Himalayas (Figure 3.3b).

In contrast, seasonal snowpack is less abundant in the SE HMA (Figure 3.3a), in part because it receives much of its precipitation in summer from the Indian and East-Asia monsoons, while the winter westerlies have minimum impact. Shallow snowpack exists over the Hengduan Shan and Tanggula Shan, with low values of SWE estimated (less than 0.2 m). For the Himalayas and Nyainqentanglha mountain ranges (Figure 3.1), which exhibit extremely high elevation and receive significant summer precipitation from the monsoons, high values of SWE are estimated in some locations (Figure 3.3b). However, those locations are largely masked out herein through the non-seasonal snow and ice mask (Figure 3.3a), because the fSCA observations are persistently high throughout the year (no observed melt-out), show irregular temporal patterns without a clear accumulation-depletion cycle (non-seasonal), or are obscured by clouds between June-Sept. (insufficient measurements), any of which can contribute to estimates of SWE that are less constrained due to cloud screening with potential errors of omission or commission in fSCA estimation.

The least abundant seasonal snowpack is estimated in the NE (Figure 3.3a), where SWE is only notable over a few mountain ranges such as the Qilian Shan, Kunlun Shan and Eastern Tibetan mountains. Despite their high elevations, most of the NE areas are snow-free or only have shallow and intermittent snow as a result of being further away from the primary atmospheric moisture sources.

Previous studies have also examined the spatiotemporal distribution in seasonal snowpack, regarding SCA (e.g. Pu et al., 2007; Basang et al., 2017), snow depth and SWE (e.g. Terzago et al., 2014; Bian et al., 2019; Orsolini et al., 2019), and the overall finding is that most existing datasets present consistent spatial patterns at large scales (e.g. regional) but differ greatly in the magnitudes of SWE and snow depth, which implies large uncertainties in snow mass estimates over this data scarce region. Similarly, HMASR exhibits coherent spatial patterns compared to these previous efforts, yet the magnitudes of SWE still show significant variability. A more comprehensive analysis of HMA SWE between multiple products will be addressed in an upcoming intercomparison paper using HMASR.

3.3.1.2 Peak seasonal SWE timing

The timing of peak seasonal SWE occurrence is associated with climatological (e.g. precipitation) and topographic (e.g. elevation) factors, and therefore shows significant heterogeneity over HMA. Figure 3.4 depicts the pixel-wise peak SWE day of water year (DOWY) climatology map. Highly intermittent snow pixels were excluded, as well as permanent snow and ice pixels via the non-seasonal snow and ice mask. Peak SWE generally occurs between DOWY 100 and DOWY 250 for seasonal snow. Specifically, the date of peak SWE timing is characterized spatially by a median of DOWY 169 (March 18th) and an interdecile range between DOWY133 (February 10th) and DOWY 217 (May 5th), as shown in Figure 3.4. However, the peak SWE DOWY shows a bimodal

distribution (Figure 3.4, inset) with the earlier peak centered on DOWY 145 and the later peak centered on DOWY 192.

For those mountain ranges in the NW, the northern and western mountain slopes of Tien Shan, the western foothills of Pamir, the entire Hindu Kush, as well as the foothills of the western Himalayas, all have relatively early peak SWE occurrences between February 10th and March 18th (Figure 3.4). In contrast, the southern mountain slopes of Tien Shan, the majority of the Pamir, Karakoram, and western Himalaya, show a relatively late peak SWE occurrence between March 18th and May 5th (Figure 3.4). For those mountain ranges in the SE and NE, the peak SWE occurrence dates are more diverse (Figure 3.4). In the SE, the central and eastern Himalayas, Nyainqentanglha, and Hengduan mountains generally have later peak SWE occurrences (between March 18th and May 5th), except in the southern foothills, where peak SWE tends to occur earlier (between February 10th and March 18th). In the NE, the eastern Tibetan mountains show the earliest peak SWE occurrence dates (before February 10th), while the Qilian Shan and Kunlun Shan show the latest peak SWE occurrences (after May 5th).

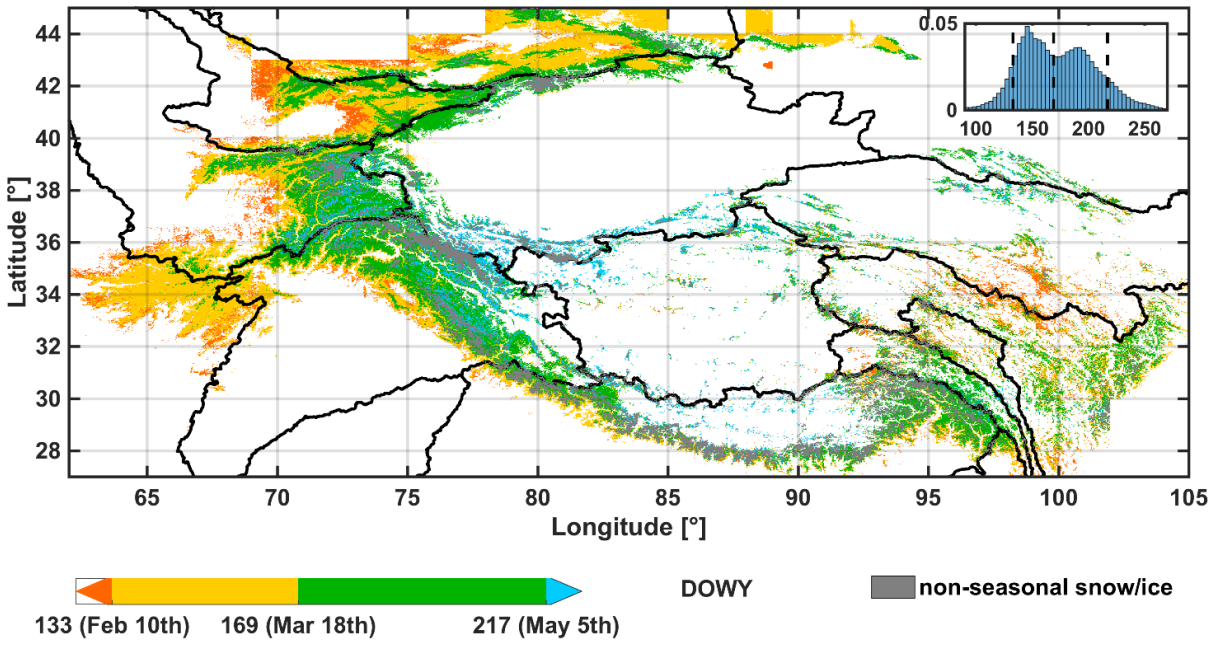

Figure 3.4: Map of pixel-wise peak seasonal SWE DOWY climatology, with non-seasonal snow and ice pixels masked out (grey). The inset figure is the histogram of peak SWE DOWY. The three dates labeled in the colorbar (DOWY 133, DOWY 169 and DOWY 217) correspond to the 10th, 50th and 90th percentile in the DOWY distribution, and are marked with vertical dashed lines in the inset histogram.

3.3.1.3 Seasonal SWE evolution

The spatial patterns of seasonal evolution of SWE, averaged over SON (September, October, November), DJF (December, January, February), MAM (March, April, May), JJA (June, July, August), are shown in Figure 3.5. As expected, higher SWE amounts are generally found in winter (DJF) and spring (MAM), while lower SWE amounts are found in summer (JJA) and fall (SON). Throughout the year, mountains in NW hold the maximum amount of SWE compared to other regions. In SON, the entire HMA region exhibits minimal SWE magnitudes (0.1 m or below) and most regions are snow free (Figure 3.5). During this period, SWE starts accumulating in the Tien

Shan, Pamir and western Himalayas that are directly facing the westerlies. SWE is also evident in Nyainqentanglha and Hengduan Shan that are associated with the summer monsoons. In DJF, both the overall magnitude and extent of SWE grow significantly, with mean SWE values up to 0.5 m found in Tien Shan, Pamir and western Himalayas (Figure 3.5). The magnitude of SWE grows even larger in MAM, with up to 1 m SWE values estimated in the western HMA mountains, and up to 0.5 m SWE values estimated in Nyainqentanglha and the eastern Himalayas. Meanwhile, the extent of SWE shrinks significantly during MAM in the Hindu Kush and Tien Shan due to the weakened westerlies in spring. In JJA, both the magnitude and extent of SWE drop dramatically over most of the domain, with some exceptions of more persistent snowpack (with up to 0.3 m SWE) still evident in the Pamir, Karakoram and Nyainqentanglha, where snow melts out slower than the surrounding regions.

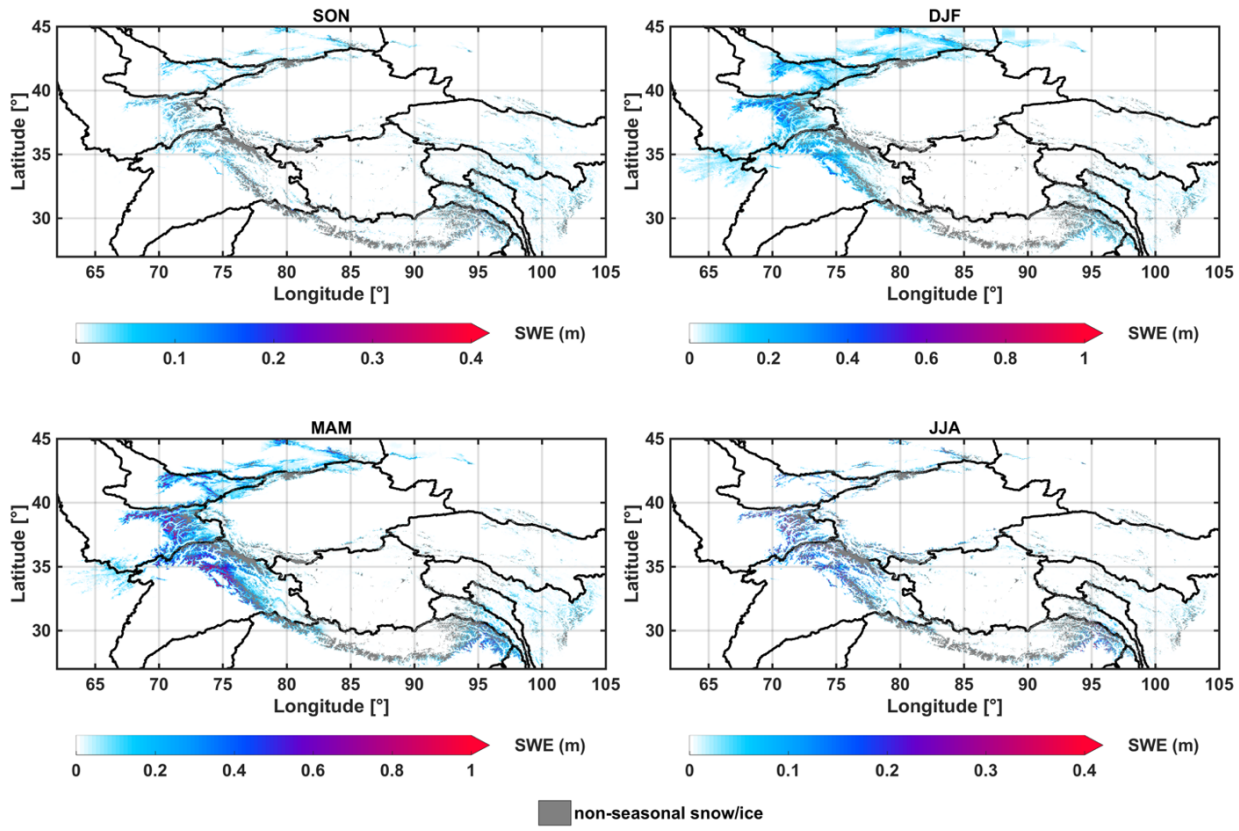

Figure 3.5: Map of mean seasonal SWE climatology in SON (September, October, November), DJF (December, January, February), MAM (March, April, May) and JJA (June, July, August), with non-seasonal snow and ice pixels masked out (grey).

3.3.2 Temporal distribution of seasonal SWE

Despite the significant literature on seasonal snowpack in this region, quantification of the regional scale SWE volume is more difficult to obtain, partly due to the large uncertainties in SWE estimation over this region. In this section, the temporal variations in integrated seasonal SWE volumes across the major river basins are quantified, with the climatology presented in Section 3.3.2.1, and the interannual variations illustrated in Section 3.3.2.2.

3.3.2.1 Climatology of seasonal SWE

The climatology of the seasonal cycle in SWE volumes that are integrated across HMA and its major river basins are quantified and presented in Figure 3.6, with the key statistics of annual peak SWE volumes (peak of the annual time-series) summarized for the entire HMA region and each basin in Table 3.1. Note again that the non-seasonal snow and ice mask has been applied when calculating the aggregated SWE volumes.

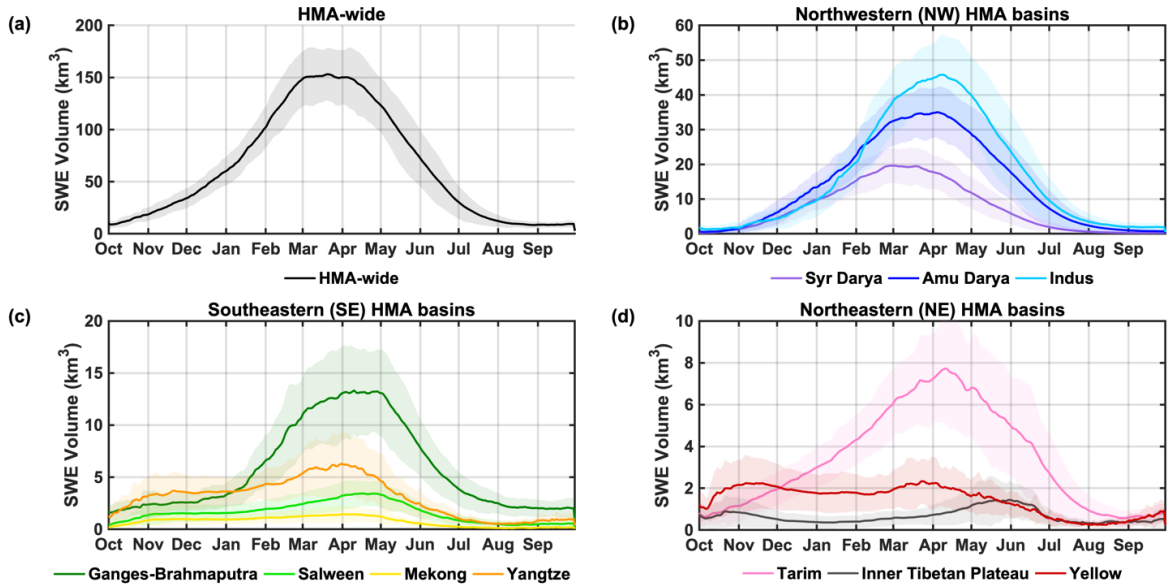

Figure 3.6: Climatological (18-year average; solid line) daily time-series of seasonal SWE volumes, aggregated to a) HMA-wide, and basins in the (b) Northwestern (NW), (c) Southeastern (SE), and (d) Northeastern (NE) subregions. The shaded area represents +/- 1 standard deviation around the climatological mean (i.e. representing a metric of interannual variation about the mean).

Table 3.1: Summary statistics for HMA-wide and basin-scale annual peak SWE volume (peak of annual time-series) assessed from the 18-year HMASR.

Region	Basin name	Peak SWE volume (peak of annual time-series)							
		Climatology		Interannual Variability					
		Mean (km^3)	Total of sub-regional mean (km^3)	Standard deviation (km^3)	Coeffi-cient of variation	Max (km^3)	Min (km^3)	Max year	Min year
HMA-wide	HMA-wide	**162.57**	**162.57 (100%)**	**26.53**	**0.16**	**227.12**	**114.10**	**2005**	**2001**
Northwestern (NW) basins	Syr Darya	21.16	**107.42 (66%)**	5.19	0.25	29.88	13.61	2010	2000
	Amu Darya	37.31		7.10	0.19	48.31	25.92	2017	2008
	Indus	48.95		10.27	0.21	63.97	23.71	2009	2001
Southeastern (SE) basins	Ganges-Brahmaputra	15.59	**29.49 (18%)**	3.84	0.25	25.40	10.69	2005	2009
	Salween	3.97		1.23	0.31	6.71	2.21	2005	2002
	Mekong	1.92		0.77	0.40	3.56	1.02	2000	2004
	Yangtze	8.02		2.97	0.37	14.79	3.32	2005	2015
Northeastern (NE) basins	Tarim	8.78	**14.78 (9%)**	2.45	0.28	12.92	4.81	2017	2007
	Inner Tibetan Plateau	2.35		0.99	0.42	4.98	0.57	2013	2004
	Yellow	3.65		1.25	0.34	6.10	1.76	2005	2004

The HMA-wide SWE volume is presented in Figure 3.6a, and the 18-year average of annual peak SWE volume is found to be 162.57 km3 (note this is higher than the peak value in Figure 3.6a, as it is the direct average of 18-year maxima rather than averaged across DOWY). The climatological peak SWE volume was further assessed in each subregion (i.e. within NW, NE and SE), and compared against that over the entire HMA (Table 3.1). The results show the highest peak SWE volume occurs in NW basins (107.42 km3, ~ 66% of domain-wide total), followed by SE basins (29.49 km3, ~18%), and NE basins (14.78 km3, ~ 9%), which is coherent with the spatial pattern shown in Figure 3.3a. Note that around ~7% of HMA-wide SWE volume falls in the regions

outside of the watersheds examined (mainly in the northmost regions shown in Figure 3.1), which is why these basin-scale quantities do not sum up to 100% of the HMA-wide totals.

For the NW basins, the maximum amount of SWE volume is found in the Indus basin, followed by Amu Darya and Syr Darya (Figure 3.6b). The seasonality of basin-scale SWE in NW displays similar features to the HMA-wide SWE, with snow accumulating from October to March/April and depleting until the end of the WY. Meanwhile, the peak SWE volume is found to occur earlier and disappear faster in the Syr Darya basin, followed by Amu Darya and Indus. This is potentially attributed to their geographic locations, where Syr Darya is located further north and only affected by the winter westerlies; Indus is located further south and is partially affected by the summer monsoons.

For the SE basins, higher SWE volumes are found in Ganges-Brahmaputra, followed by Yangtze, Salween and Mekong (Figure 3.6c). It is worthwhile to note that Ganges-Brahmaputra has an average peak SWE volume of 15.59 km3, with an average carry-over SWE volume of around 2 km3 at the end of the WY (Figure 3.6c). This amount of carry-over SWE volume in Ganges-Brahmaputra is a result of the facts that 1) its mountain ranges (Himalayas) have higher elevation than those in other basins, and 2) based on the non-seasonal snow and ice criterion (Section 3.2.4), a carry-over SWE within 10% of the maximum SWE in each year is allowed. Meanwhile, the seasonality in basin-scale SWE over SE is distinct across basins, e.g. the Ganges-Brahmaputra and Salween shows more unimodal features (with obvious peaking in April-May), while Yangtze and Mekong shows more bimodal/uniform features, which are likely to be associated with the intermittent snowpack and summer monsoons.

For the NE basins over HMA, the overall magnitude of SWE volumes is smallest (Figure 3.6d). These basins all have relatively large areas, but are mostly snow-free or covered by shallow snow

as depicted in Figure 3.3a. Distinct seasonal features are also observed in these basins, e.g. a unimodal seasonal cycle of SWE is found in Tarim with an obvious peak in mid-April, while the Inner Tibetan Plateau and Yellow show more uniform features that are potentially attributed to the intermittent snow, as they are further away from the moisture sources (limited influence by westerlies and monsoons).

3.3.2.2 Interannual variations in SWE and timing

In addition to the 18-year climatology of SWE volumes in Section 3.3.2.1, the interannual variations in HMA-wide and basin-scale peak SWE and its timing are further illustrated in Figure 3.7- Figure 3.9 and Table 3.1. The aggregated seasonal SWE volume across HMA-wide or basin-scales are visualized in the 18-year time-series (Figure 3.7), which illustrates a strong seasonal cycle and significant interannual variations in peak SWE. Over the record examined, the HMA-wide annual peak SWE volume (Table 3.1; Figure 3.7) is found to be largest in WY2005 with a value of 227.12 km^3, smallest in WY2001 with a value of 114.10 km^3, and has a standard deviation of 26.53 km^3 (i.e. a coefficient of variation of 16%). Basin-scale annual peak SWE volumes also exhibit significant variations, with their standard deviations ranging from 0.77 km^3 (coefficient of variation of 40%) in Mekong to 10.27 km^3 (coefficient of variation of 21%) in Indus. Moreover, different maximum/minimum years of peak SWE are found in each basin, and are not always synchronous with the maximum/minimum years found in HMA-wide SWE (Table 3.1; Figure 3.7).

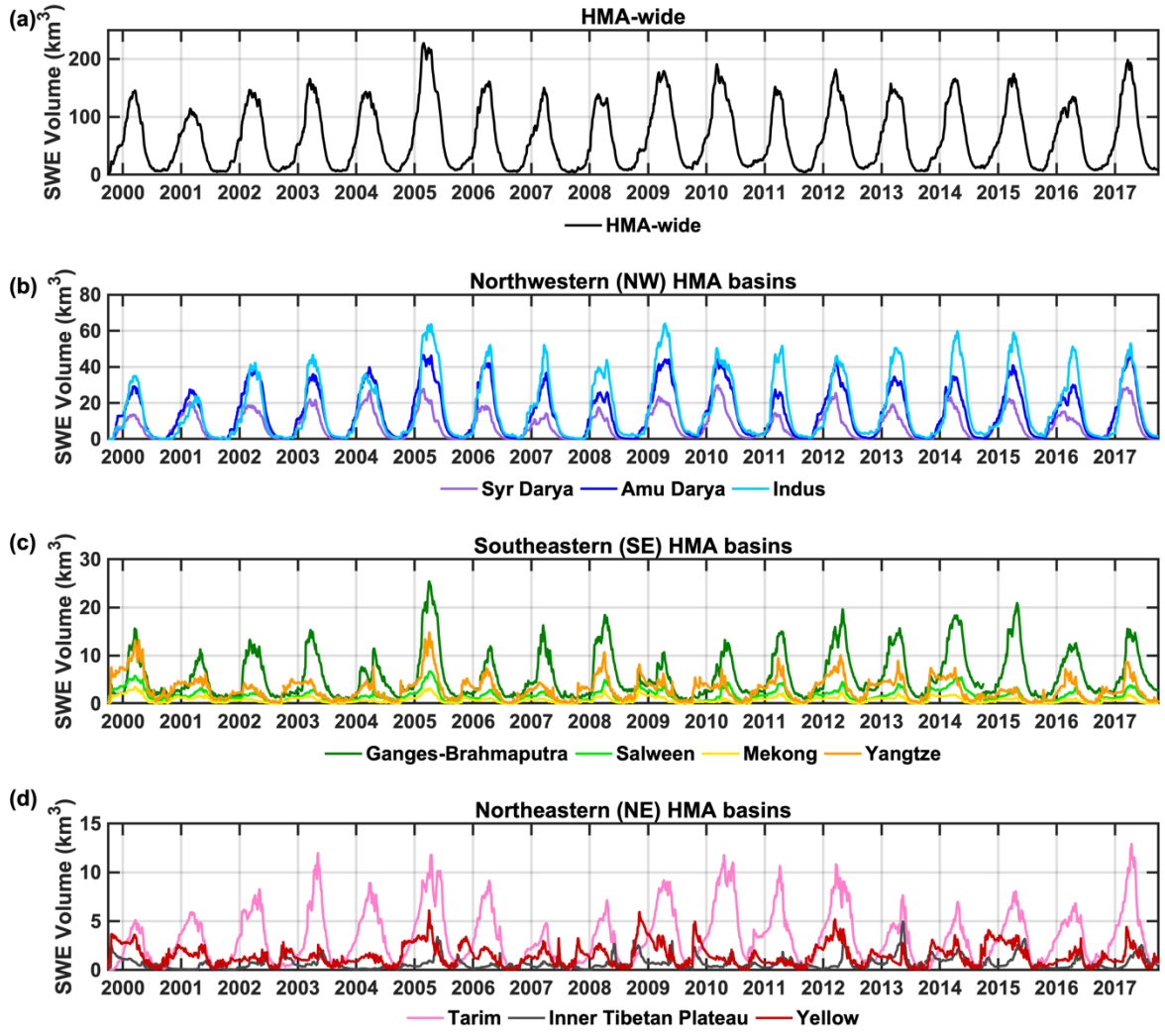

Figure 3.7: Daily time-series of seasonal SWE volumes aggregated to (a) HMA-wide, (b) Northwestern (NW), (c) Southeastern (SE), and (d) Northeastern (NE) basin totals.

When focusing on the HMA-wide seasonal cycle across different WYs (Figure 3.8), it is found that snowpack quickly accumulates to over 10 km^3 in SWE volume during October, approaching ~50% of its peak SWE volume in January for most WYs, reaching a peak SWE volume within March and April, with an averaged timing of DOWY 168 (March 17th) when averaged over 18 WYs. After peaking, the seasonal snowpack starts depleting and declines back to ~50% of its peak volume in May and June for most WYs. Snowpack depletes to under 10 km^3 in SWE volume

between July and September, except in WYs 2009, 2010 and 2014 that have persistent snow across the entire year. The interannual variations across WYs are evident in: 1) the variation in peak SWE volume and the peak dates, which range from 114 km^3 to 227 km^3 in volume and from late February (DOWY 146) to mid-April (DOWY 195); 2) the variation in the temporal window where the snow storage is more than 50% of the peak SWE, that span between 3.5 months (WY2003) to 5.5 months (WY2016); 3) the variation in timing when snowpack depletes to under 10 km^3 in SWE volume, which ranges between July and October.

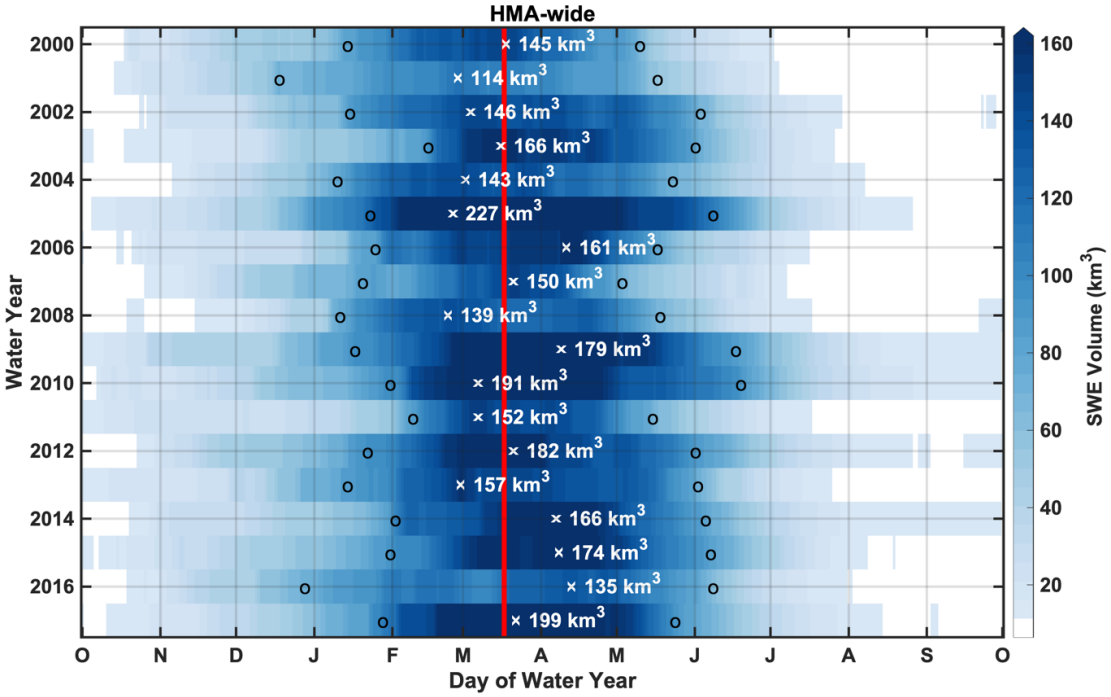

Figure 3.8: Daily time-series of HMA-wide SWE volumes displayed as functions of DOWY and WY. The symbol 'x' is used to mark the date of peak SWE volume occurrence, with the corresponding peak SWE volume labeled in each WY. The symbol 'o' is used to mark the dates when 50% of the peak SWE volume is reached in each WY. The vertical red line is used to indicate the 18-year average timing of HMA-wide peak SWE volume.

The basin-scale results (Figure 3.9) show more variation compared to the HMA-wide results, with divergent peak SWE dates across basins and across WYs. The seasonal cycle observed in NW and many other basins (Syr Darya, Amu Darya, Indus, Ganges-Brahmaputra, Tarim), are clearly influenced by winter westerlies, with SWE typically peaking around April and depleting in July – October, and that seasonality is consistent when examined across different WYs. The interannual variations in these basins are mainly reflected by 1) the overall magnitude of SWE volumes, 2) timing of snowpack occurrences/disappearances, while the peak SWE dates are closely centered around the climatological mean dates (~April). However, different seasonal cycles are observed in the other basins (Mekong, Yangtze, Inner Tibetan Plateau and Yellow) that are more influenced by the summer monsoons, when examined across different WYs. For example, peak SWE may occur as early as October and as late as July within the same basin. The persistence of snow also varies across basins and WYs, with SWE being either persistently high across several months, or intermittent over a short period of time. These factors explain the bimodal or uniform features in the SWE time-series and its climatology (Figure 3.6- Figure 3.7).

It is also worthwhile to note that the average peak SWE dates are in March and April for most basins, while it is not necessarily representative for some basins (e.g. Inner Tibetan Plateau and Yellow) that have highly varying dates across years. Moreover, the average dates in many basins appear to be later than the HMA-wide average peak SWE date (March 17th), mainly because a portion of the HMA-wide SWE falls in the northmost regions that is outside of the watersheds examined (above Syr Darya), and those regions are most influenced by the winter westerlies and reach peak SWE very early (before March 19th; Figure 3.4).

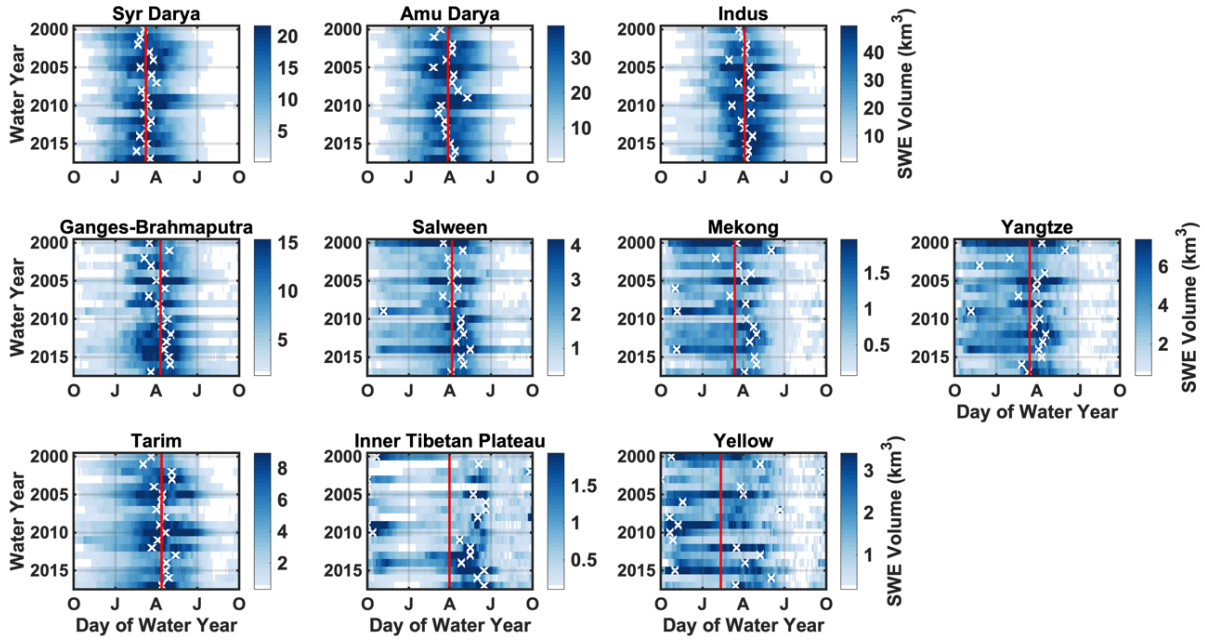

Figure 3.9: Daily time-series of basin-scale SWE volumes displayed as functions of DOWY and WY. The symbol 'x' is used to mark the date of basin-scale peak SWE volume occurrence in each WY. The vertical red line is used to indicate the 18-year average timing of basin-scale peak SWE volume.

3.3.3 Elevational distribution of seasonal SWE

The pixel-wise peak SWE distribution vs. elevation was assessed, both in terms of its 18-year averaged climatology (Section 3.3.3.1) and its variations under different climate conditions (Section 3.3.3.2). The HMA-wide domain and each basin were divided into 5-percentile elevation bins, so that the aggregated SWE volumes are calculated over comparable areas, following the method in Smith and Bookhagen (2018). The non-seasonal snow and ice pixels were removed when calculating peak seasonal SWE volume, and its fractional areal coverage within a given elevation band is computed to assess the relative elevational contributions to total seasonal SWE volume.

3.3.3.1 Seasonal peak SWE climatology

When examining the SWE climatology over the full HMA domain (Figure 3.10), the seasonal pixel-wise peak SWE volume was found to be largest at mid elevations (3000 - 4000 m), with peak SWE values occurring at elevations around 3500 m (Figure 3.10a and Figure 3.10b, top row). The large increase in SWE from lower to mid-elevations is indicative of orographic enhancement, where the decrease at higher elevations is indicative of moisture limitations on orographic effects and/or increasing amounts of non-seasonal snow and ice. The presence of non-seasonal snow and ice becomes evident at elevations above 3500 m, and it increases dramatically above 5000 m with a value up to 35% (Figure 3.10c, top row). When assessing the cumulative fraction of SWE volume as a function of elevation, it was found that over 50% of HMA-wide seasonal SWE volume is stored at elevations above 3500 m, and less than 10% of seasonal SWE volume is stored at elevations below 2000 m (Figure 3.10d, top row).

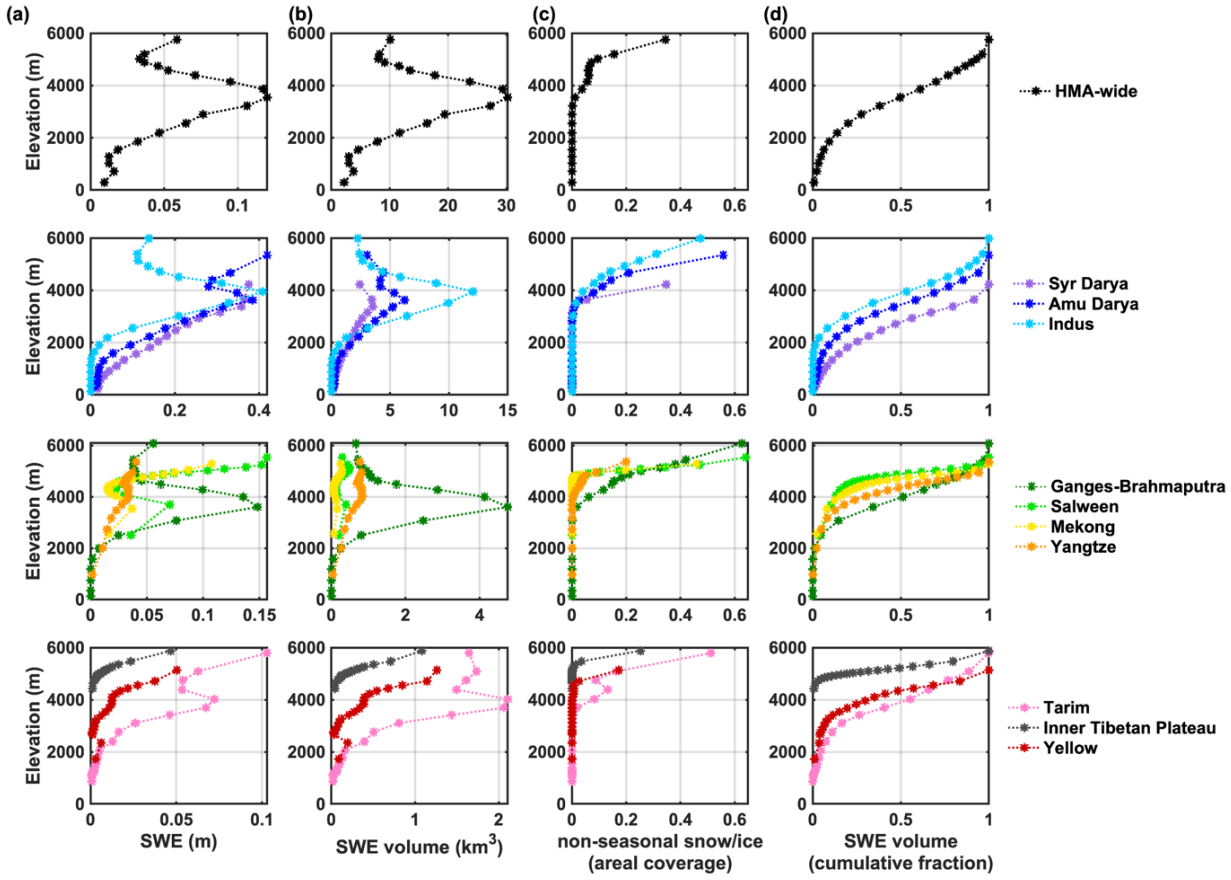

Figure 3.10: Pixel-wise peak seasonal (a) SWE climatology, (b) SWE volume climatology, (c) fractional areal coverage of non-seasonal snow and ice within each elevation band, and (d) cumulative fraction of SWE volume above the specified elevation, within HMA, Northwestern (NW), Southeastern (SE) and Northeastern (NE) basins. Elevation is discretized into 5% percentile bins.

The subregional elevational distribution of pixel-wise peak SWE climatology and its volume vary in each basin, compared to the HMA-wide results (Figure 3.10). Relatively similar characteristics are observed in the NW basins (Syr Darya, Amu Darya and Indus), Tarim in NE, and Ganges-Brahmaputra and Yangtze in SE, where the pixel-wise peak SWE volumes (Figure 3.10b) generally increase with elevation (below ~4000 m) and then decline with elevation (above ~4000 m), reaching their maximum values at mid elevations (3000 - 4000 m). While the SWE distribution

(Figure 3.10a) is generally consistent with the SWE volume distribution (Figure 3.10b) within these basins, the SWE values at high elevations (e.g. ~6000 m) are large, contributing to a non-negligible amount of seasonal SWE volume at high elevations, despite the relatively high coverage of non-seasonal snow and ice (up to 60%; Figure 3.10c) above 4000 m in these basins. Moreover, for the cumulative fraction of SWE volumes above a specified elevation (Figure 3.10d), unique median values are found within each basin, e.g ~4000 m (Indus, Ganges-Brahmaputra, Tarim), ~3500 m (Amu Darya), or ~2800 m (Syr Darya).

Other basins in SE (Salween, Mekong) and NE (Yellow, Inner Tibetan Plateau) generally show monotonically increasing SWE and SWE volumes against elevation (Figure 3.10a, Figure 3.10b). These basins feature relatively small SWE volumes, and low coverage of non-seasonal snow and ice coverage (mostly under 25%; Figure 3.10c) at high elevations. For the cumulative fraction of SWE volumes above a specified elevation (Figure 3.10d), the median values are found at higher elevations for SE and NE (between 4000 - 5200 m) basins.

3.3.3.2 Variations under different climate conditions

The elevational distribution of peak SWE was also examined under different climate conditions (e.g. warm vs. cool years, wet vs. dry years) relative to normal conditions. Such analysis identifies whether different climate conditions affect the overall snow storage distribution across different elevations. For categorizing the different climate conditions, the HMA-wide winter precipitation and (near-surface) air temperature were used (Table 3.2), where winter (DJF) denotes the period from December 1st to March 1st. A “k-means” clustering analysis method (Lloyd, 1982) was used to seek classification of different climate conditions, based on the normalized winter precipitation and air temperature (subtracting the mean values and dividing by the standard deviations). The number of clusters to be classified is an input to the method; five clusters were specified in an

attempt to group annual realizations into ‘normal’, ‘wet’, ‘dry’, ‘warm’ and ‘cool’ categories. The classified clusters are displayed in Figure 3.11, where the five clusters are logically grouped and interpreted as the categories mentioned above. It should be noted that there is a slight correlation (correlation coefficient of 0.29 with a p-value of 0.25) between annual realizations of precipitation and air temperature, indicating warmer years tend to be wetter years (but statistically insignificant due to the limited number of years).

Table 3.2: HMA pixel-wise peak SWE volume, winter precipitation volume and winter air temperature, with each year categorized as dry/normal/wet/warm/cool based on clustering classification.

WY	Peak SWE volume pixel-wise (km^3)	Winter		Clustering Category
		Precipitation volume (km^3)	Air temperature (K)	
2000	214.08	251.51	261.65	dry
2001	187.97	204.28	262.21	dry
2002	240.66	309.23	262.60	normal
2003	266.22	330.72	262.71	normal
2004	235.36	313.29	262.31	normal
2005	355.55	422.90	262.14	wet
2006	254.80	318.94	263.04	warm
2007	224.51	303.16	262.43	normal
2008	249.79	316.56	260.73	cool
2009	294.83	339.96	263.19	warm
2010	313.81	331.18	262.53	normal
2011	237.69	294.65	261.54	cool
2012	283.24	282.77	260.77	cool
2013	263.14	337.68	262.01	normal
2014	273.41	292.81	262.19	normal
2015	266.62	330.90	262.71	normal
2016	226.62	258.84	262.48	dry
2017	306.40	351.42	263.68	warm

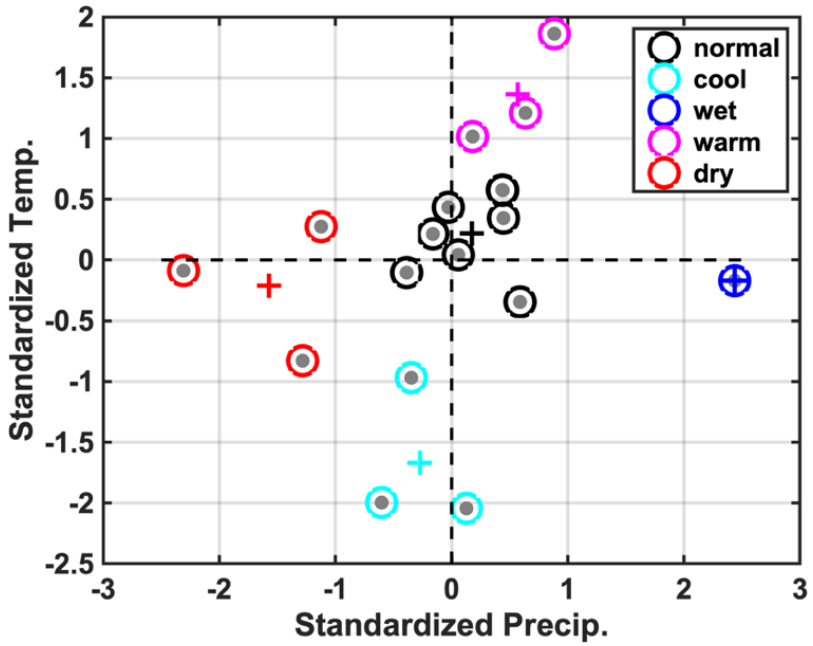

Figure 3.11: Category of different climate conditions from clustering analysis, based on the normalized winter precipitation and winter air temperature. Five clusters were identified as normal, wet, dry warm and cool conditions, with the centroid of each cluster marked with the '+' symbol.

Based on these clusters, the average pixel-wise peak SWE volumes under the same climate conditions are computed. The cluster-averaged peak SWE volume under dry, normal, and wet years are 209.6 km^3, 260.5 km^3, and 355.6 km^3 respectively. As shown in Figure 3.12a, as expected, in spanning from dry to wet years there are marked increases in peak SWE volume over all elevations, particularly over the mid to low elevations (e.g. below 4000 m). In drier years, while Figure 3.12a shows less SWE volumes across all elevations, the fractional SWE volumes are not always smallest, as shown in Figure 3.12b. It can be observed that the fractional SWE volumes in dry years are smaller than those in normal years, in the low-to-mid elevations (~1500 - 3600 m). At mid-to-high elevations (~3600 - 5500 m), the dry years show greater fractional SWE volumes, compared to normal years. On the contrary, wet years show larger fractional SWE volumes below ~ 3000 m, and smaller fractional SWE volumes above ~3000 m, when compared to normal years.

Such differences in the fractional SWE volumes may be due to two potential factors: 1) the dry conditions generally have less humid air, which may have accelerated evaporation and snow sublimation at lower elevations prior to peak timing; and 2) a slight shift in snowfall/precipitation towards higher elevations during drier years due to orographic effects, i.e. precipitation tends to occur at higher elevations where the moist and less humid air is cold enough to reach condensation. Note that the cluster-averaged air temperature is quite consistent under wet/dry/normal conditions, which should minimize the effect of air temperature differences on snow distribution in Figure 3.12a and Figure 3.12b.

Similarly, the pixel-wise peak SWE distribution under warm, normal, and cool years are examined. The cluster-averaged peak SWE volumes under warm, normal and cool years are 285.34 km^3, 260.47 km^3, and 256.91 km^3, respectively, with cluster-averaged air temperatures of 263.30 K, 262.44 K, and 261.01 K. It should be noted that, the warm year cluster has greater peak SWE volumes (by ~25 km^3) than the normal and cool years, which is reflected by the slightly higher precipitation in the warm year cluster (Figure 3.11). Therefore, we put more emphasis on the fractional peak SWE distribution (Figure 3.12d) here, to eliminate the effect of overall snow volume on snow distribution. The results indicate that warm and normal years have very consistent distributions, when the fractional SWE volumes are examined (Figure 3.12d). It is most notable that cool years have higher fractions of snow stored at lower elevations (e.g. below 3000 m), and smaller fractions of snow stored at mid elevations (3000 - 4000 m), compared to normal and warm years (Figure 3.12d dotted lines). As the difference in air temperature between normal and cool years is ~1.5 K, this may indicate that the low elevation snow storage tends to shift towards higher elevations (e.g. to mid elevations) with 1.5 K of warming (from cool to normal conditions), when the overall snow storage is the same.

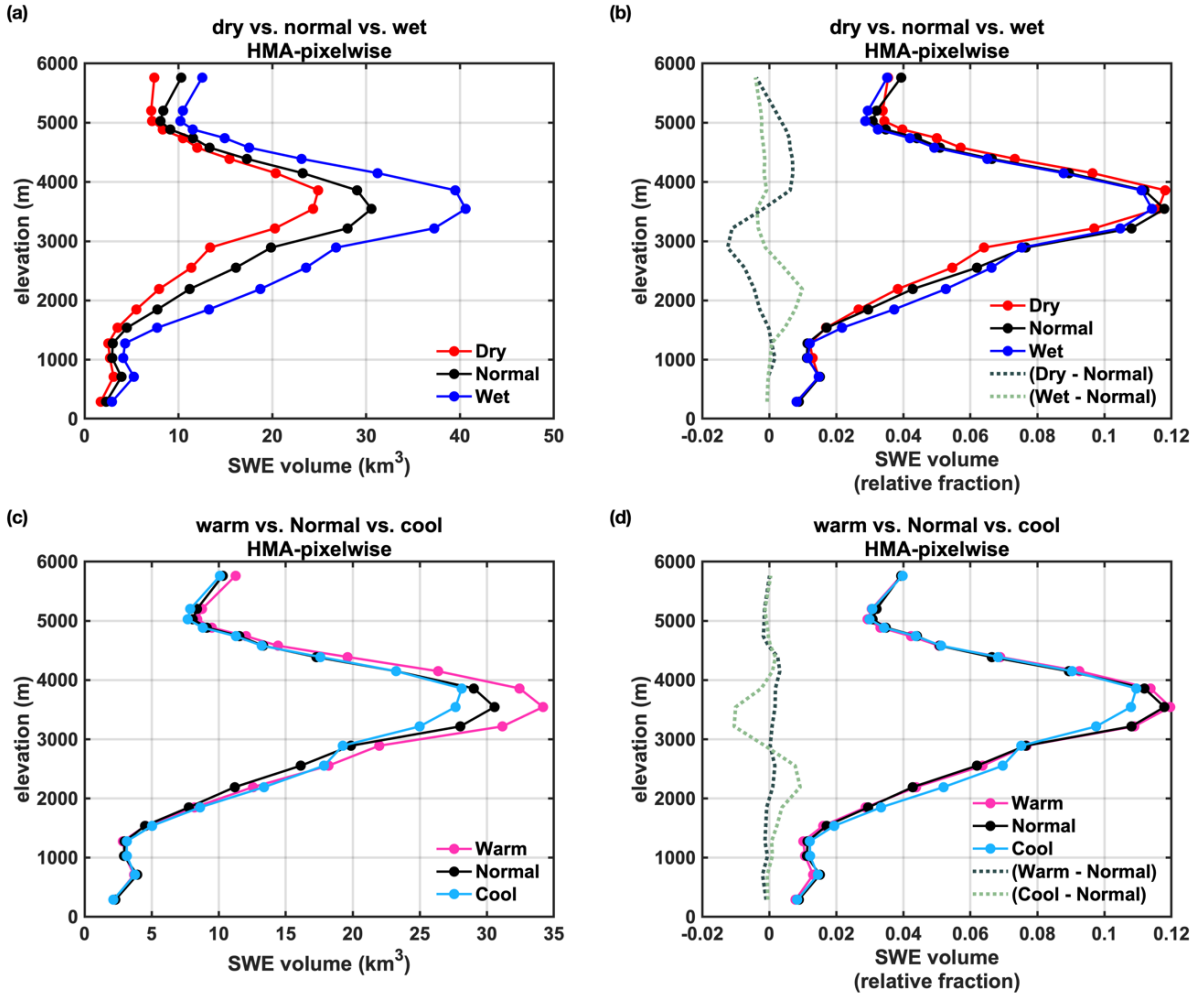

Figure 3.12: Cluster-averaged pixel-wise peak SWE volume (and its relative fraction, i.e. normalized with total SWE volume) distribution vs. elevation under different climate conditions in HMA. Here (a) and (b) show the distribution under dry, normal, and wet conditions; (c) and (d) show the distribution under warm, normal, and cool conditions. Difference curves with reference to the normal condition are also provided in (b) and (d) as shown with dashed lines.

3.4 Conclusions

A first-order spatiotemporal analysis of seasonal SWE over the HMA region is presented in this paper, using a new 18-year snow reanalysis dataset (HMASR; Liu et al., 2021). This HMASR dataset is derived based on a previously developed snow reanalysis scheme (Margulis et al., 2019)

that jointly assimilates fSCA observations from both Landsat and MODSCAG products, which has daily outputs of SWE and other snow variables, with a spatial resolution of 16 arc-second (~500 m), over the joint period of Landsat and MODIS from WYs 2000 to 2017.

This work herein used the new HMASR dataset to address scientific questions aimed at characterizing how seasonal SWE and snow storage is distributed spatially, temporally and elevationally across and within HMA. In terms of the spatial distribution, seasonal snow is most abundant in the NW, with over 1 m of peak SWE observed over the mountain ranges. Seasonal snow is also significant in the SE, where both relatively deep snowpacks (with peak SWE values up to 1 m or above) and shallow snowpacks (with peak SWE up to 0.2 m) are found. Seasonal snow is less abundant in the NE where most areas are snow free, or only covered by shallow snowpacks (with peak SWE values below 0.2 m). The domain-wide median date of peak SWE is estimated to be March 18th with significant heterogeneity across this region, linked with climatological drivers and topography.

When aggregating the total SWE volumes across the full HMA domain and its basins, the climatological peak seasonal SWE volume was found to be 163 km^3, with NW basins accounting for around 66% of that volume, followed by SE (~18%) and NE (~9%) basins. The seasonal cycle of HMA-wide SWE is depicted by snow accumulating through October to March and April, typically peaking around April and depleting in July-October. When examined at basin-scales, similar seasonality is observed in the westerly-affected basins (e.g. in NW), while different SWE seasonality is observed in monsoon-affected basins (in SE and NE). Interannual variations in HMA-wide or basin-scale SWE are also evident, with peak SWE volumes ranging from 114 km^3 to 227 km^3 and peak dates ranging from late February (DOWY 146) to mid April (DOWY 195), when examined over the HMA-scale. The basin-scale SWE is more different from the HMA-wide

SWE, where peak SWE may occur as early as October and as late as July, and are divergent across basins and across WYs.

The climatology of HMA-wide seasonal peak SWE is found to be most abundant at mid-elevations (3000 - 4000 m), with over 50% of the seasonal SWE volume stored at elevations above 3500 m. When comparing wet, normal, and dry years, we found that years with above-average amounts of precipitation causes significant overall increase in SWE volumes across all elevations. Meanwhile, a slight increase in air temperature (e.g. ~ 1.5 K) from cooler to normal years, mainly leads to an redistribution in snow storage from lower elevations to mid elevations, when the overall snow volume is the same.

This HMASR dataset is presented to augment the spatiotemporal gaps in previous SWE datasets and provide better characterization of spatiotemporal patterns in seasonal snowpack over the HMA region, especially over the mountainous areas with complex terrain where existing products tend to underestimate SWE and present large uncertainties (Wrzesien et al., 2019; Kim et al., 2021). It should prove useful in providing more insight into the role of seasonal snowpack in the regional hydrological cycle, as a verification dataset for atmospheric and other models, and in other applications where a space-time continuous snow dataset constrained by remote sensing data is needed.

It should be noted that the reanalysis method is generally expected to work best for seasonal snow where there is a strong signature between snow disappearance and measured fSCA. Hence an important caveat is that non-seasonal snow pixels are likely to be more erroneous than the seasonal snow pixels. The use of a non-seasonal vs. seasonal snow mask is used in this paper to highlight the part of snow storage that is deemed seasonal snow. In the raw dataset, all pixels are provided and so users are free to take advantage of the non-seasonal snow estimates (with the caveat

mentioned above). For the purposes of highlighting a new estimate of seasonal snow climatology in this paper, we focus on seasonal snow alone.

It is also acknowledged that the reanalysis method is best designed for non-ephemeral snow where there is a strong seasonal cycle and signal between snow disappearance and measured fSCA that can be captured at the frequency of the fSCA measurements. Hence ephemeral snow (i.e. shallow and intermittent) may not be fully captured. Finally, the accuracy of fSCA retrievals are likely not as high in the monsoon dominated parts of HMA, which in our case excludes many more Landsat/MODSCAG measurements, resulting in higher uncertainty in SWE estimation over affected sub-regions like the Himalayas. Other remote-sensing approaches (e.g., active microwave measurements) that could penetrate clouds may potentially aid in reducing the uncertainties for SWE estimation over those areas. More research can be done to address such issues and improve the accuracy of SWE estimates for those regions in the future.

3.5 Bibliography

Ahmad, J. A., Forman, B. A., & Kwon, Y. (2019). Analyzing Machine Learning Predictions of Passive Microwave Brightness Temperature Spectral Difference Over Snow-Covered Terrain in High Mountain Asia. Frontiers in Earth Science, 7, 212. https://doi.org/10.3389/feart.2019.00212

Armstrong, R. L., Rittger, K., Brodzik, M. J., Racoviteanu, A., Barrett, A. P., Khalsa, S.-J. S., Raup, B., Hill, A. F., Khan, A. L., Wilson, A. M., Kayastha, R. B., Fetterer, F., & Armstrong, B. (2019). Runoff from glacier ice and seasonal snow in High Asia: Separating melt water sources in river flow. Regional Environmental Change, 19(5), 1249–1261. https://doi.org/10.1007/s10113-018-1429-0

Bair, E. H., Abreu Calfa, A., Rittger, K., & Dozier, J. (2018). Using machine learning for real-time estimates of snow water equivalent in the watersheds of Afghanistan. The Cryosphere, 12(5), 1579–1594. https://doi.org/10.5194/tc-12-1579-2018

Bair, E. H., Rittger, K., Ahmad, J. A., & Chabot, D. (2020). Comparison of modeled snow properties in Afghanistan, Pakistan, and Tajikistan. The Cryosphere, 14(1), 331–347. https://doi.org/10.5194/tc-14-331-2020

Bair, E. H., Stillinger, T., Rittger, K., & Skiles, M. (2021). COVID-19 lockdowns show reduced pollution on snow and ice in the Indus River Basin. Proceedings of the National Academy of Sciences, 118(18), e2101174118. https://doi.org/10.1073/pnas.2101174118

Barnett, T. P., Adam, J. C., & Lettenmaier, D. P. (2005). Potential impacts of a warming climate on water availability in snow-dominated regions. Nature, 438(7066), 303–309. https://doi.org/10.1038/nature04141

Basang, D., Barthel, K., & Olseth, J. A. (2017). Satellite and Ground Observations of Snow Cover in Tibet during 2001–2015. Remote Sensing, 9(11). https://doi.org/10.3390/rs9111201

Bian, Q., Xu, Z., Zhao, L., Zhang, Y.-F., Zheng, H., Shi, C., Zhang, S., Xie, C., & Yang, Z.-L. (2019). Evaluation and Intercomparison of Multiple Snow Water Equivalent Products over the Tibetan Plateau. Journal of Hydrometeorology, 20(10), 2043–2055. https://doi.org/10.1175/JHM-D-19-0011.1

Bolch, T., Kulkarni, A., Kääb, A., Huggel, C., Paul, F., Cogley, J. G., Frey, H., Kargel, J. S., Fujita, K., Scheel, M., Bajracharya, S., & Stoffel, M. (2012). The State and Fate of Himalayan Glaciers. Science, 336(6079), 310. https://doi.org/10.1126/science.1215828

Bolch, T., Shea, J. M., Liu, S., Azam, F. M., Gao, Y., Gruber, S., Immerzeel, W. W., Kulkarni, A., Li, H., Tahir, A. A., Zhang, G., & Zhang, Y. (2019). Status and Change of the Cryosphere

in the Extended Hindu Kush Himalaya Region. In P. Wester, A. Mishra, A. Mukherji, & A. B. Shrestha (Eds.), The Hindu Kush Himalaya Assessment: Mountains, Climate Change, Sustainability and People (pp. 209–255). Springer International Publishing. https://doi.org/10.1007/978-3-319-92288-1_7

Bookhagen, B., & Burbank, D. W. (2010). Toward a complete Himalayan hydrological budget: Spatiotemporal distribution of snowmelt and rainfall and their impact on river discharge. Journal of Geophysical Research: Earth Surface, 115(F3). https://doi.org/10.1029/2009JF001426

Bormann, K. J., Brown, R. D., Derksen, C., & Painter, T. H. (2018). Estimating snow-cover trends from space. Nature Climate Change, 8(11), 924–928. https://doi.org/10.1038/s41558-018-0318-3

Chang, A. T. C., Foster, J. L., & Hall, D. K. (1987). Nimbus-7 SMMR Derived Global Snow Cover Parameters. Annals of Glaciology, 9, 39–44. Cambridge Core. https://doi.org/10.3189/S0260305500200736

Che, T., Li, X., Jin, R., Armstrong, R., & Zhang, T. (2008). Snow depth derived from passive microwave remote-sensing data in China. Annals of Glaciology, 49, 145–154. Cambridge Core. https://doi.org/10.3189/172756408787814690

Cortés, G., Girotto, M., & Margulis, S. A. (2014). Analysis of sub-pixel snow and ice extent over the extratropical Andes using spectral unmixing of historical Landsat imagery. Remote Sensing of Environment, 141, 64–78. https://doi.org/10.1016/j.rse.2013.10.023

Cortés, G., & Margulis, S. (2017). Impacts of El Niño and La Niña on interannual snow accumulation in the Andes: Results from a high-resolution 31 year reanalysis. Geophysical Research Letters, 44(13), 6859–6867. https://doi.org/10.1002/2017GL073826

Dahe, Q., Shiyin, L., & Peiji, L. (2006). Snow Cover Distribution, Variability, and Response to Climate Change in Western China. Journal of Climate, 19(9), 1820–1833. https://doi.org/10.1175/JCLI3694.1

Dai, L., Che, T., Ding, Y., & Hao, X. (2017). Evaluation of snow cover and snow depth on the Qinghai–Tibetan Plateau derived from passive microwave remote sensing. The Cryosphere, 11(4), 1933–1948. https://doi.org/10.5194/tc-11-1933-2017

Dee, D. P., Uppala, S. M., Simmons, A. J., Berrisford, P., Poli, P., Kobayashi, S., Andrae, U., Balmaseda, M. A., Balsamo, G., Bauer, P., Bechtold, P., Beljaars, A. C. M., van de Berg, L., Bidlot, J., Bormann, N., Delsol, C., Dragani, R., Fuentes, M., Geer, A. J., … Vitart, F. (2011). The ERA-Interim reanalysis: Configuration and performance of the data assimilation system. Quarterly Journal of the Royal Meteorological Society, 137(656), 553–597. https://doi.org/10.1002/qj.828

Dozier, J. (1989). Spectral signature of alpine snow cover from the landsat thematic mapper. Remote Sensing of Environment, 28, 9–22. https://doi.org/10.1016/0034-4257(89)90101-6

Dozier, J., Bair, E. H., & Davis, R. E. (2016). Estimating the spatial distribution of snow water equivalent in the world's mountains. WIREs Water, 3(3), 461–474. https://doi.org/10.1002/wat2.1140

Durand, M., Molotch, N. P., & Margulis, S. A. (2008). A Bayesian approach to snow water equivalent reconstruction. Journal of Geophysical Research: Atmospheres, 113(D20). https://doi.org/10.1029/2008JD009894

Gelaro, R., McCarty, W., Suárez, M. J., Todling, R., Molod, A., Takacs, L., Randles, C. A., Darmenov, A., Bosilovich, M. G., Reichle, R., Wargan, K., Coy, L., Cullather, R., Draper,

C., Akella, S., Buchard, V., Conaty, A., da Silva, A. M., Gu, W., … Zhao, B. (2017). The Modern-Era Retrospective Analysis for Research and Applications, Version 2 (MERRA-2). Journal of Climate, 30(14), 5419–5454. https://doi.org/10.1175/JCLI-D-16-0758.1

Girotto, M., Margulis, S. A., & Durand, M. (2014). Probabilistic SWE reanalysis as a generalization of deterministic SWE reconstruction techniques. Hydrological Processes, 28(12), 3875–3895. https://doi.org/10.1002/hyp.9887

Hall, D. K., Riggs, G. A., Salomonson, V. V., DiGirolamo, N. E., & Bayr, K. J. (2002). MODIS snow-cover products. The Moderate Resolution Imaging Spectroradiometer (MODIS): A New Generation of Land Surface Monitoring, 83(1), 181–194. https://doi.org/10.1016/S0034-4257(02)00095-0

Hansen, M. C., Defries, R. S., Townshend, J. R. G., & Sohlberg, R. (2000). Global land cover classification at 1 km spatial resolution using a classification tree approach. International Journal of Remote Sensing, 21(6–7), 1331–1364. https://doi.org/10.1080/014311600210209

Hersbach, H., Bell, B., Berrisford, P., Hirahara, S., Horányi, A., Muñoz-Sabater, J., Nicolas, J., Peubey, C., Radu, R., Schepers, D., Simmons, A., Soci, C., Abdalla, S., Abellan, X., Balsamo, G., Bechtold, P., Biavati, G., Bidlot, J., Bonavita, M., … Thépaut, J.-N. (2020). The ERA5 global reanalysis. Quarterly Journal of the Royal Meteorological Society, 146(730), 1999–2049. https://doi.org/10.1002/qj.3803

Immerzeel, W. W., & Bierkens, M. F. P. (2012). Asia's water balance. Nature Geoscience, 5(12), 841–842. https://doi.org/10.1038/ngeo1643

Immerzeel, W. W., Droogers, P., de Jong, S. M., & Bierkens, M. F. P. (2009). Large-scale monitoring of snow cover and runoff simulation in Himalayan river basins using remote

sensing. Remote Sensing of Environment, 113(1), 40–49. https://doi.org/10.1016/j.rse.2008.08.010

Immerzeel, W. W., Lutz, A. F., Andrade, M., Bahl, A., Biemans, H., Bolch, T., Hyde, S., Brumby, S., Davies, B. J., Elmore, A. C., Emmer, A., Feng, M., Fernández, A., Haritashya, U., Kargel, J. S., Koppes, M., Kraaijenbrink, P. D. A., Kulkarni, A. V., Mayewski, P. A., … Baillie, J. E. M. (2020). Importance and vulnerability of the world's water towers. Nature, 577(7790), 364–369. https://doi.org/10.1038/s41586-019-1822-y

Immerzeel, W. W., van Beek, L. P. H., & Bierkens, M. F. P. (2010). Climate Change Will Affect the Asian Water Towers. Science, 328(5984), 1382. https://doi.org/10.1126/science.1183188

Kääb, A., Berthier, E., Nuth, C., Gardelle, J., & Arnaud, Y. (2012). Contrasting patterns of early twenty-first-century glacier mass change in the Himalayas. Nature, 488(7412), 495–498. https://doi.org/10.1038/nature11324

Kim, R. S., Kumar, S., Vuyovich, C., Houser, P., Lundquist, J., Mudryk, L., Durand, M., Barros, A., Kim, E. J., Forman, B. A., Gutmann, E. D., Wrzesien, M. L., Garnaud, C., Sandells, M., Marshall, H.-P., Cristea, N., Pflug, J. M., Johnston, J., Cao, Y., … Wang, S. (2021). Snow Ensemble Uncertainty Project (SEUP): Quantification of snow water equivalent uncertainty across North America via ensemble land surface modeling. The Cryosphere, 15(2), 771–791. https://doi.org/10.5194/tc-15-771-2021

Kirkham, J. D., Koch, I., Saloranta, T. M., Litt, M., Stigter, E. E., Møen, K., Thapa, A., Melvold, K., & Immerzeel, W. W. (2019). Near Real-Time Measurement of Snow Water Equivalent in the Nepal Himalayas. Frontiers in Earth Science, 7, 177. https://doi.org/10.3389/feart.2019.00177

KOBAYASHI, S., OTA, Y., HARADA, Y., EBITA, A., MORIYA, M., ONODA, H., ONOGI, K., KAMAHORI, H., KOBAYASHI, C., ENDO, H., MIYAOKA, K., & TAKAHASHI, K. (2015). The JRA-55 Reanalysis: General Specifications and Basic Characteristics. Journal of the Meteorological Society of Japan. Ser. II, 93(1), 5–48. https://doi.org/10.2151/jmsj.2015-001

Largeron, C., Dumont, M., Morin, S., Boone, A., Lafaysse, M., Metref, S., Cosme, E., Jonas, T., Winstral, A., & Margulis, S. A. (2020). Toward Snow Cover Estimation in Mountainous Areas Using Modern Data Assimilation Methods: A Review. Frontiers in Earth Science, 8, 325. https://doi.org/10.3389/feart.2020.00325

Lettenmaier, D. P., Alsdorf, D., Dozier, J., Huffman, G. J., Pan, M., & Wood, E. F. (2015). Inroads of remote sensing into hydrologic science during the WRR era. Water Resources Research, 51(9), 7309–7342. https://doi.org/10.1002/2015WR017616

Lievens, H., Demuzere, M., Marshall, H.-P., Reichle, R. H., Brucker, L., Brangers, I., de Rosnay, P., Dumont, M., Girotto, M., Immerzeel, W. W., Jonas, T., Kim, E. J., Koch, I., Marty, C., Saloranta, T., Schöber, J., & De Lannoy, G. J. M. (2019). Snow depth variability in the Northern Hemisphere mountains observed from space. Nature Communications, 10(1), 4629. https://doi.org/10.1038/s41467-019-12566-y

Liston, G. E. (2004). Representing Subgrid Snow Cover Heterogeneities in Regional and Global Models. Journal of Climate, 17(6), 1381–1397. https://doi.org/10.1175/1520-0442(2004)017<1381:RSSCHI>2.0.CO;2

Liu, Y., & Margulis, S. A. (2019). Deriving Bias and Uncertainty in MERRA-2 Snowfall Precipitation Over High Mountain Asia. Frontiers in Earth Science, 7, 280. https://doi.org/10.3389/feart.2019.00280

Liu, Y., Fang, Y., & Margulis, S.A. (2021): High Mountain Asia UCLA Daily Snow Reanalysis, Version 1. Boulder, Colorado USA, NASA Snow and Ice Data Center Distributed Active Archive Center, doi:10.5067/HNAUGJQXSCVU

Lloyd, S. (1982). Least squares quantization in PCM. IEEE Transactions on Information Theory, 28(2), 129–137. https://doi.org/10.1109/TIT.1982.1056489

Lutz, A. F., Immerzeel, W. W., Shrestha, A. B., & Bierkens, M. F. P. (2014). Consistent increase in High Asia's runoff due to increasing glacier melt and precipitation. Nature Climate Change, 4(7), 587–592. https://doi.org/10.1038/nclimate2237

Margulis, S. A., Cortés, G., Girotto, M., & Durand, M. (2016). A Landsat-Era Sierra Nevada Snow Reanalysis (1985–2015). Journal of Hydrometeorology, 17(4), 1203–1221. https://doi.org/10.1175/JHM-D-15-0177.1

Margulis, S. A., Girotto, M., Cortés, G., & Durand, M. (2015). A Particle Batch Smoother Approach to Snow Water Equivalent Estimation. Journal of Hydrometeorology, 16(4), 1752–1772. https://doi.org/10.1175/JHM-D-14-0177.1

Margulis, S. A., Liu, Y., & Baldo, E. (2019). A Joint Landsat- and MODIS-Based Reanalysis Approach for Midlatitude Montane Seasonal Snow Characterization. Frontiers in Earth Science, 7, 272. https://doi.org/10.3389/feart.2019.00272

Maussion, F., Scherer, D., Finkelnburg, R., Richters, J., Yang, W., & Yao, T. (2011). WRF simulation of a precipitation event over the Tibetan Plateau, China – an assessment using remote sensing and ground observations. Hydrology and Earth System Sciences, 15(6), 1795–1817. https://doi.org/10.5194/hess-15-1795-2011

Maussion, F., Scherer, D., Mölg, T., Collier, E., Curio, J., & Finkelnburg, R. (2014). Precipitation Seasonality and Variability over the Tibetan Plateau as Resolved by the High Asia

Reanalysis. Journal of Climate, 27(5), 1910–1927. https://doi.org/10.1175/JCLI-D-13-00282.1

Mortimer, C., Mudryk, L., Derksen, C., Luojus, K., Brown, R., Kelly, R., & Tedesco, M. (2020). Evaluation of long-term Northern Hemisphere snow water equivalent products. The Cryosphere, 14(5), 1579–1594. https://doi.org/10.5194/tc-14-1579-2020

Mudryk, L. R., Derksen, C., Kushner, P. J., & Brown, R. (2015). Characterization of Northern Hemisphere Snow Water Equivalent Datasets, 1981–2010. Journal of Climate, 28(20), 8037–8051. https://doi.org/10.1175/JCLI-D-15-0229.1

Notarnicola, C. (2020). Observing Snow Cover and Water Resource Changes in the High Mountain Asia Region in Comparison with Global Mountain Trends over 2000–2018. Remote Sensing, 12(23). https://doi.org/10.3390/rs12233913

Orsolini, Y., Wegmann, M., Dutra, E., Liu, B., Balsamo, G., Yang, K., de Rosnay, P., Zhu, C., Wang, W., Senan, R., & Arduini, G. (2019). Evaluation of snow depth and snow cover over the Tibetan Plateau in global reanalyses using in situ and satellite remote sensing observations. The Cryosphere, 13(8), 2221–2239. https://doi.org/10.5194/tc-13-2221-2019

Osmanoglu, B., Painter, T. H., Shean, D., Arendt, A., Kargel, J., & Margulis, S. A. (2017). Remote sensing of the cryosphere in high mountain ASIA. 2017 IEEE International Geoscience and Remote Sensing Symposium (IGARSS), 2813–2816. https://doi.org/10.1109/IGARSS.2017.8127583

Painter, T. H., Brodzik, M. J., Racoviteanu, A., & Armstrong, R. (2012). Automated mapping of Earth's annual minimum exposed snow and ice with MODIS. Geophysical Research Letters, 39(20). https://doi.org/10.1029/2012GL053340

Painter, T. H., Dozier, J., Roberts, D. A., Davis, R. E., & Green, R. O. (2003). Retrieval of subpixel snow-covered area and grain size from imaging spectrometer data. Remote Sensing of Environment, 85(1), 64–77. https://doi.org/10.1016/S0034-4257(02)00187-6

Painter, T. H., Rittger, K., McKenzie, C., Slaughter, P., Davis, R. E., & Dozier, J. (2009). Retrieval of subpixel snow covered area, grain size, and albedo from MODIS. Remote Sensing of Environment, 113(4), 868–879. https://doi.org/10.1016/j.rse.2009.01.001

Palazzi, E., von Hardenberg, J., & Provenzale, A. (2013). Precipitation in the Hindu-Kush Karakoram Himalaya: Observations and future scenarios. Journal of Geophysical Research: Atmospheres, 118(1), 85–100. https://doi.org/10.1029/2012JD018697

Pfeffer, W. T., Arendt, A. A., Bliss, A., Bolch, T., Cogley, J. G., Gardner, A. S., Hagen, J.-O., Hock, R., Kaser, G., Kienholz, C., Miles, E. S., Moholdt, G., Mölg, N., Paul, F., Radić, V., Rastner, P., Raup, B. H., Rich, J., & Sharp, M. J. (2014). The Randolph Glacier Inventory: A globally complete inventory of glaciers. Journal of Glaciology, 60(221), 537–552. Cambridge Core. https://doi.org/10.3189/2014JoG13J176

Pu, Z., Xu, L., & Salomonson, V. V. (2007). MODIS/Terra observed seasonal variations of snow cover over the Tibetan Plateau. Geophysical Research Letters, 34(6). https://doi.org/10.1029/2007GL029262

Pulliainen, J., Luojus, K., Derksen, C., Mudryk, L., Lemmetyinen, J., Salminen, M., Ikonen, J., Takala, M., Cohen, J., Smolander, T., & Norberg, J. (2020). Patterns and trends of Northern Hemisphere snow mass from 1980 to 2018. Nature, 581(7808), 294–298. https://doi.org/10.1038/s41586-020-2258-0

Raup, B., Racoviteanu, A., Khalsa, S. J. S., Helm, C., Armstrong, R., & Arnaud, Y. (2007). The GLIMS geospatial glacier database: A new tool for studying glacier change. Climate

Change Impacts on Mountain Glaciers and Permafrost, 56(1), 101–110. https://doi.org/10.1016/j.gloplacha.2006.07.018

RGI Consortium. (2017). Randolph Glacier Inventory (RGI) – A Dataset of Global Glacier Outlines: Version 6.0. Technical Report, Global Land Ice Measurements from Space, Boulder, Colorado, USA. Digital Media. DOI: https://doi.org/10.7265/N5-RGI-60

Rienecker, M. M., Suarez, M. J., Gelaro, R., Todling, R., Bacmeister, J., Liu, E., Bosilovich, M. G., Schubert, S. D., Takacs, L., Kim, G.-K., Bloom, S., Chen, J., Collins, D., Conaty, A., da Silva, A., Gu, W., Joiner, J., Koster, R. D., Lucchesi, R., … Woollen, J. (2011). MERRA: NASA's Modern-Era Retrospective Analysis for Research and Applications. Journal of Climate, 24(14), 3624–3648. https://doi.org/10.1175/JCLI-D-11-00015.1

Rodell, M., Houser, P. R., Jambor, U., Gottschalck, J., Mitchell, K., Meng, C.-J., Arsenault, K., Cosgrove, B., Radakovich, J., Bosilovich, M., Entin, J. K., Walker, J. P., Lohmann, D., & Toll, D. (2004). The Global Land Data Assimilation System. Bulletin of the American Meteorological Society, 85(3), 381–394. https://doi.org/10.1175/BAMS-85-3-381

Rounce, D. R., Hock, R., & Shean, D. E. (2020). Glacier Mass Change in High Mountain Asia Through 2100 Using the Open-Source Python Glacier Evolution Model (PyGEM). Frontiers in Earth Science, 7, 331. https://doi.org/10.3389/feart.2019.00331

Scott, C. A., Zhang, F., Mukherji, A., Immerzeel, W., Mustafa, D., & Bharati, L. (2019). Water in the Hindu Kush Himalaya. In P. Wester, A. Mishra, A. Mukherji, & A. B. Shrestha (Eds.), The Hindu Kush Himalaya Assessment: Mountains, Climate Change, Sustainability and People (pp. 257–299). Springer International Publishing. https://doi.org/10.1007/978-3-319-92288-1_8

Sexton, J. O., Song, X.-P., Feng, M., Noojipady, P., Anand, A., Huang, C., Kim, D.-H., Collins, K. M., Channan, S., DiMiceli, C., & Townshend, J. R. (2013). Global, 30-m resolution continuous fields of tree cover: Landsat-based rescaling of MODIS vegetation continuous fields with lidar-based estimates of error. International Journal of Digital Earth, 6(5), 427–448. https://doi.org/10.1080/17538947.2013.786146

Shean, D. E., Bhushan, S., Montesano, P., Rounce, D. R., Arendt, A., & Osmanoglu, B. (2020). A Systematic, Regional Assessment of High Mountain Asia Glacier Mass Balance. Frontiers in Earth Science, 7, 363. https://doi.org/10.3389/feart.2019.00363

Smith, T., & Bookhagen, B. (2016). Assessing uncertainty and sensor biases in passive microwave data across High Mountain Asia. Remote Sensing of Environment, 181, 174–185. https://doi.org/10.1016/j.rse.2016.03.037

Smith, T., & Bookhagen, B. (2018). Changes in seasonal snow water equivalent distribution in High Mountain Asia (1987 to 2009). Science Advances, 4(1), e1701550. https://doi.org/10.1126/sciadv.1701550

Smith, T., & Bookhagen, B. (2020). Assessing Multi-Temporal Snow-Volume Trends in High Mountain Asia From 1987 to 2016 Using High-Resolution Passive Microwave Data. Frontiers in Earth Science, 8, 392. https://doi.org/10.3389/feart.2020.559175

Sorg, A., Bolch, T., Stoffel, M., Solomina, O., & Beniston, M. (2012). Climate change impacts on glaciers and runoff in Tien Shan (Central Asia). Nature Climate Change, 2(10), 725–731. https://doi.org/10.1038/nclimate1592

Stigter, E. E., Wanders, N., Saloranta, T. M., Shea, J. M., Bierkens, M. F. P., & Immerzeel, W. W. (2017). Assimilation of snow cover and snow depth into a snow model to estimate snow

water equivalent and snowmelt runoff in a Himalayan catchment. The Cryosphere, 11(4), 1647–1664. https://doi.org/10.5194/tc-11-1647-2017

Sun, S., & Xue, Y. (2001). Implementing a new snow scheme in Simplified Simple Biosphere Model. Advances in Atmospheric Sciences, 18(3), 335–354. https://doi.org/10.1007/BF02919314

Tahir, A. A., Chevallier, P., Arnaud, Y., & Ahmad, B. (2011). Snow cover dynamics and hydrological regime of the Hunza River basin, Karakoram Range, Northern Pakistan. Hydrology and Earth System Sciences, 15(7), 2275–2290. https://doi.org/10.5194/hess-15-2275-2011

Takala, M., Luojus, K., Pulliainen, J., Derksen, C., Lemmetyinen, J., Kärnä, J.-P., Koskinen, J., & Bojkov, B. (2011). Estimating northern hemisphere snow water equivalent for climate research through assimilation of space-borne radiometer data and ground-based measurements. Remote Sensing of Environment, 115(12), 3517–3529. https://doi.org/10.1016/j.rse.2011.08.014

Terzago, S., von Hardenberg, J., Palazzi, E., & Provenzale, A. (2014). Snowpack Changes in the Hindu Kush–Karakoram–Himalaya from CMIP5 Global Climate Models. Journal of Hydrometeorology, 15(6), 2293–2313. https://doi.org/10.1175/JHM-D-13-0196.1

Wang, X., Wu, C., Wang, H., Gonsamo, A., & Liu, Z. (2017). No evidence of widespread decline of snow cover on the Tibetan Plateau over 2000–2015. Scientific Reports, 7(1), 14645. https://doi.org/10.1038/s41598-017-15208-9

Winiger, M., Gumpert, M., & Yamout, H. (2005). Karakorum–Hindukush–western Himalaya: Assessing high-altitude water resources. Hydrological Processes, 19(12), 2329–2338. https://doi.org/10.1002/hyp.5887

Wrzesien, M. L., Pavelsky, T. M., Durand, M. T., Dozier, J., & Lundquist, J. D. (2019). Characterizing Biases in Mountain Snow Accumulation From Global Data Sets. Water Resources Research, 55(11), 9873–9891. https://doi.org/10.1029/2019WR025350

Xue, Y., Houser, P. R., Maggioni, V., Mei, Y., Kumar, S. V., & Yoon, Y. (2019). Assimilation of Satellite-Based Snow Cover and Freeze/Thaw Observations Over High Mountain Asia. Frontiers in Earth Science, 7, 115. https://doi.org/10.3389/feart.2019.00115

Xue, Y., Sun, S., Kahan, D., & Jiao, Y. (2003). Impact of parameterizations in snow physics and interface processes on the simulation of snow cover and runoff at several cold region sites. Journal of Geophysical Research, 108. https://doi.org/10.1029/2002JD003174

Yao, T., Thompson, L., Yang, W., Yu, W., Gao, Y., Guo, X., Yang, X., Duan, K., Zhao, H., Xu, B., Pu, J., Lu, A., Xiang, Y., Kattel, D. B., & Joswiak, D. (2012). Different glacier status with atmospheric circulations in Tibetan Plateau and surroundings. Nature Climate Change, 2(9), 663–667. https://doi.org/10.1038/nclimate1580

CHAPTER 4

How well do we know seasonal snow storage in HMA?:

An intercomparison with a new snow reanalysis

Accurate knowledge of peak snow water storage is essential to water supply for regions reliant on snowmelt-driven runoff. However, our knowledge in data-sparse regions such as High Mountain Asia (HMA) is still limited. In this work, eight globally available snow products were examined over HMA, using a newly developed High Mountain Asia Snow Reanalysis (HMASR) dataset as a reference.

The analysis focused on peak accumulation season storage since it is a first-order determinant of warm-season water availability. The results suggest an HMA-wide peak snow storage estimate, across global snow products, of 161 km^3 ± 102 km^3 indicating a large uncertainty, with an average underestimate of 33% compared to HMASR (239 km^3). The errors and uncertainty vary across watersheds, with estimates of seasonal (110 km^3 ± 74 km^3) vs. intermittent (51 km^3 ± 28 km^3) snow regimes, showing 33% less and 70% more peak snow storage compared to HMASR, respectively.

Large inter-product variability is found in cumulative snowfall and ablation during the accumulation season leading up to peak snow storage. The accumulation season snowfall is quantified as 335 km^3 ± 148 km^3 over the entire HMA, where a significant fraction (51% ± 9%) of the snowfall is lost to ablation during the accumulation season. The fraction varies when considering snow regime with 37% ± 13% for seasonal snow and 67% ± 7% for intermittent snow. The results show that inter-product snowfall variability explains most of the peak snow storage uncertainty (over 80%) during the accumulation season, partly because of the wide range of

uncertainty in precipitation (and snowfall), while ablation explains more variation when considering subsets of snow products.

4.1 Introduction:

Seasonal snow from global mountain "water towers" provides a virtual reservoir during the cold season that can ultimately supply water in the warm season through snowmelt-driven runoff (Viviroli et al., 2007). In High Mountain Asia (HMA), snowmelt feeds the major river basins in their headwaters (Bookhagen and Burbank, 2010; Armstrong et al., 2019), with significant contributions to overall runoff (Khanal et al., 2021; Kraaijenbrink et al., 2021), and is critical for meeting the human water demands in spring and summer. Snow storage in seasonal snowpack and the timing of snowmelt are highly sensitive to a warming climate, which is likely to alter the frequency of snow droughts (Huning and AghaKouchak, 2020), and pose risks to the water security for natural and human use (Immerzeel et al., 2020; Qin et al., 2020; Kraaijenbrink et al., 2021).

Peak snow storage at a given location in the landscape (when snow water equivalent (SWE) reaches its peak at the end of the accumulation season before starting to melt) is the key metric of available water for warm-season runoff. Accurately estimating peak snow storage (and its spatial distribution) is a first-order requirement for assessing snow-derived water availability for downstream use. Despite its importance, quantification of snow mass over the world's mountains is still poorly constrained (Mudryk et al., 2015; Wrzesien et al., 2019), primarily due to the difficulties in the direct measurements of SWE, which is not available over large scales from either dense enough in situ networks or satellite-based remote sensing platforms (Palazzi et al., 2013; Dozier et al., 2016; Bormann et al., 2018). Alternative estimates of snow mass can be provided through modeling approaches, e.g. from atmospheric reanalysis, land data assimilation, GCMs and

RCMs. Nevertheless, previous intercomparison studies suggest large discrepancies in snow mass estimation, when examining different models and products over the entire northern hemisphere (Mudryk et al., 2015; Mortimer et al., 2020; Xiao et al., 2020), North America (McCrary and Mearns, 2019; Wrzesien et al., 2019; Xu et al., 2019; Kim et al., 2021), Hindu Kush-Karakoram-Himalaya (Terzago et al., 2014), and the Tibetan Plateau (Bian et al., 2019; Orsolini et al., 2019). Despite the large uncertainties seen in multi-dataset snow mass comparisons, often a single dataset is used when assessing the links between snowpack storage, regional water availability and climate change (e.g. Mankin et al., 2015; Huning and AghaKouchak, 2020; Immerzeel et al., 2020; Qin et al., 2020). Without improved characterization of seasonal snow storage in regions that depend heavily on snow-derived water (e.g. HMA), our confidence in estimates of available water resources and how they are changing will remain compromised, thus impacting our ability to effectively adapt to ongoing changes.

The scarcity of ground observations and the lack of reference datasets has limited a thorough evaluation of snow mass estimates over the broad HMA domain. In this study, the newly developed High Mountain Asia Snow Reanalysis (HMASR; Liu et al., 2021) is employed as a reference SWE dataset for examining the peak snow storage estimates from eight global atmospheric reanalysis and land data assimilation products in this region. The focus herein is understanding peak SWE estimates during the accumulation season (and not melt season processes) due to its first-order determination of available water supply. The rationale for this focus is that accurately characterizing peak storage is a necessary condition for ultimately accurately representing ablation season processes. The following science questions are addressed in this research:

1. What is the uncertainty in peak seasonal snow water storage over High Mountain Asia and its watersheds?

2. How much of the uncertainty in peak snow storage is explained by accumulation season snowfall and ablation variability, respectively?

4.2 Data

Herein the reference SWE dataset (HMASR) and the eight atmospheric and land data assimilation reanalysis datasets (chosen as representative community-based global products that span most of the period of HMASR (1999-2017)) are examined. The global products include: ERA5 and ERA5-land (European Centre for Medium-Range Weather Forecasts (ECMWF) Re-Analysis products, 5th generation), MERRA2 (Modern-Era Retrospective analysis for Research and Applications, version 2), JRA55 (Japanese 55-year Reanalysis) and GLDAS-2.1 (Global Land Data Assimilation System version 2.1 at several resolutions and with different land surface models). A summary of these datasets is given in Table 4.1, with details in the subsections below. The intercomparison study period is chosen as Water Years (WYs) 2001 to 2017, which has the maximum overlap between all datasets (as GLDAS datasets start in calendar year 2000 and HMASR ends in WY2017). The WY convention used is that, for example, WY 2001 spans from October 1, 2000 to September 30, 2001. Hereafter, to distinguish between the globally-available datasets and the reference dataset, we use “snow products” and “HMASR” respectively.

Table 4.1: Characteristics of datasets used in this study, including the spatial-temporal extent and resolution, land surface model, and whether assimilating any snow observations. For the globally-available snow products, in addition to SWE, other forcing variables such as precipitation (*P*), air temperature (T_a) and snowfall (*S*) are also used. [1] Liu et al., 2021; [2] Muñoz-Sabater et al., 2021; [3] Hersbach et al., 2020; [4] Rodell et al., 2004; [5] Gelaro et al., 2017; [6] Kobayashi et al., 2015

Dataset	Spatial resolution	Temporal coverage	Temporal resolution	Land Surface Model	Assimilated snow observations	Available variables used in analysis
HMASR[1] (reference)	1/255° x 1/255°	1999/10 - 2017/09	Daily	SSiB3	Fractional snow-covered area from Landsat and MODSCAG	SWE
ERA5-Land[2]	0.1° x 0.1°	1950 - present	Hourly	H-TESSEL	-	SWE, *P, T_a, S*
ERA5[3]	0.25° x 0.25°	1950 - present	Hourly	H-TESSEL	In situ snow depth; IMS snow cover (binary)	SWE, *P, T_a, S*
GLDAS-Noah (0.25°)[4]	0.25° x 0.25°	2000/01 - present	3 hours	Noah	-	SWE*, P, T_a, S*
MERRA2[5]	0.625° x 0.5°	1979 - present	Hourly	Catchment	-	SWE, *P, T_a, S*
JRA-55[6]	0.5625° x 0.5616°	1958 - present	3 or 6 hours	SiB	In-situ snow depth, SSM/I, SSMIS snow cover (binary)	SWE, *P, T_a, S*
GLDAS-Noah (1°) GLDAS-VIC (1°) GLDAS-CLSM (1°)	1° x 1°	2000/01 - present	3 hours	Noah VIC Catchment	-	SWE, *P, T_a, S*

All nine datasets provide SWE estimates which are used to evaluate the metric of seasonal water storage up to peak SWE, with the use of HMASR SWE as the reference in the intercomparison. Other meteorological forcings (precipitation, *P*; air temperature, T_a; and snowfall, *S*) are obtained from the global snow products. HMASR (which does not output snowfall) provides only SWE for comparison. The meteorological forcing variables are obtained at their raw spatial and temporal resolution as listed in Table 4.1, and further aggregated into daily total values (for *P* and *S*) or daily

averaged values (for T_a) in each snow product. Spatial aggregation is also performed for SWE and meteorological forcings, which is further described in Sections 4.3.2 and 4.3.3.

4.2.1 HMASR

HMASR (Liu et al., 2021) is a novel snow-specific reanalysis dataset, providing estimates of daily SWE at 1/255° (~500 m) resolution, available from WYs 2000 to 2017. Among all datasets examined in this work, HMASR is unique in that it was specifically designed for seasonal snow estimation in the HMA region, leveraging remotely sensed fractional snow-covered area (fSCA) and an advanced ensemble-based data assimilation framework. It is directly constrained by snow observations and offers the potential of SWE evaluation at high elevations and over complex terrain, where in-situ stations are non-existent.

HMASR uses the SSiB3 snow and land surface model (Sun and Xue, 2001; Xue et al., 2003) coupled with the Liston snow depletion curve (Liston, 2004). A snow reanalysis scheme (Margulis et al. 2019) is employed to jointly assimilate the batch of satellite-derived fractional snow-covered area (fSCA) from Landsat and the MODIS Snow Covered-Area and Grain size retrieval (MOSCAG; Painter et al., 2009) over a given WY. The MERRA2 forcing variables (e.g. raw precipitation, air temperature, etc.) are used as the baseline forcing inputs in HMASR, with appropriate uncertainty and topographic downscaling and bias-correction (Margulis et al., 2019; Liu and Margulis, 2019). In particular, a priori precipitation is considered highly uncertain and then implicitly corrected as part of the assimilation framework (Margulis et al. 2019; Liu et al., 2021).

4.2.2 ERA5 and ERA5-land

ERA5 (Hersbach et al., 2020) is the 5th generation product of ECMWF atmospheric reanalyses that provides hourly estimates from 1950 to present, at a spatial resolution of 0.25°. The Tiled

ECMWF Scheme for Surface Exchanges over Land incorporating land surface hydrology (H-TESSEL) is used as the LSM to obtain the ERA5 estimates. Both in-situ snow depth observations and snow cover data (binary) from the Interactive Multi-Sensor Snow and Ice Mapping System (IMS) are used in its snow data assimilation system with an Optimal Interpolation (OI) method. It is worthwhile to note that the IMS data was not applied to elevations above 1500 m in the ERA5 snow scheme (Bian et al., 2019), and the available snow depth stations are relatively limited over the HMA region.

In addition to the ERA5 product itself, the ERA5-land (Muñoz-Sabater et al., 2021) dataset at finer resolution (0.1°) is derived by ECMWF. The downscaled ERA5 forcing variables (e.g. air temperature and humidity, with lapse rate correction) are used as inputs, with the same LSM (H-TESSEL) used in the ERA5-land simulation. No data assimilation is used to derive the ERA5-land product, and hourly estimates are available from 1950 to present.

4.2.3 MERRA2

MERRA2 (Gelaro et al., 2017) is the 2nd version of NASA's Global Modeling and Assimilation Office (GMAO) reanalysis product, that provides hourly estimates from 1979 to present at a spatial resolution of 0.625° x 0.5°. The LSM used is the Catchment model (CLSM) and no snow data assimilation is performed. Note that a bias-corrected precipitation (PRECTOTCORR) field is what MERRA2 uses as the precipitation inputs (Reichle et al., 2017) to derive its land surface state estimates including SWE.

4.2.4 JRA55

JRA55 (Kobayashi et al., 2015) is the latest version of the Japan Meteorology Agency (JMA) reanalysis product that provides sub-daily (e.g. 3 hours for snowfall and 6 hours for SWE and air temperature) estimates for a 55-year period (from 1958 to present). The dataset contains outputs

at a few spatial resolutions where the highest so-called modeling resolution (~0.5625° x 0.5616°) is used herein. JRA55 uses the Simple Biosphere (SiB) model as the LSM in deriving its estimates. Station observed snow depth and satellite retrieved (binary) snow cover from the Special Sensor Microwave/Imager (SSM/I) and Special Sensor Microwave Imager Sounder (SSMIS) are used to update snow depth through data assimilation, using an OI method. Snow mass (SWE) estimates are converted from snow depth estimates by assuming a constant snow density (200 kg/m^3; Onogi et al., 2007). Note that the JRA55 product assimilates snow depth stations over the Tibetan Plateau, while ERA5 does not (Onogi et al., 2007; Bian et al., 2019; Orsolini et al., 2019).

4.2.5 GLDAS-2.1

GLDAS-2.1 (Rodell et al., 2004) is a global land data assimilation product generated by the NASA Goddard Space Flight Center (GSFC), providing estimates at sub-daily (3 hours) and 0.25° or 1° resolution, available from January 2000 to present. It contains four datasets: two Noah model driven datasets at 0.25° and 1° resolution, one Variable Infiltration Capacity (VIC) model driven dataset at 1° resolution, and one Catchment (CLSM) model driven dataset at 1° resolution, denoted as GLDAS-Noah (0.25°), GLDAS-Noah (1°), GLDAS-VIC (1°) and GLDAS-CLSM (1°) hereafter. All of the GLDAS-2.1 products are generated using the same set of meteorological forcing inputs, without any snow data assimilation.

4.3 Study region and Methods

4.3.1 Study domain and classification of seasonal, intermittent, and persistent snow regions

The HMA region (Figure 4.1a; bounded by 27°N to 45°N and from 60°N to 105°N) includes key mountain ranges (e.g. Tien Shan, Pamir, Karakoram, Himalayas, etc.) and the Tibetan Plateau, providing sources of water for the largest river basins (e.g. Indus, Ganges, Yangtze, Yellow, etc.) in Asia. This region is significantly covered by snow and ice, with westerlies dominating winter

precipitation in the northwest and the Indian and East Asia monsoons dominating summer precipitation in the southeast (Yao et al., 2012). Melt water from seasonal snow and glaciers greatly contributes to the downstream water supply (Bookhagen and Burbank, 2010; Armstrong et al., 2019).

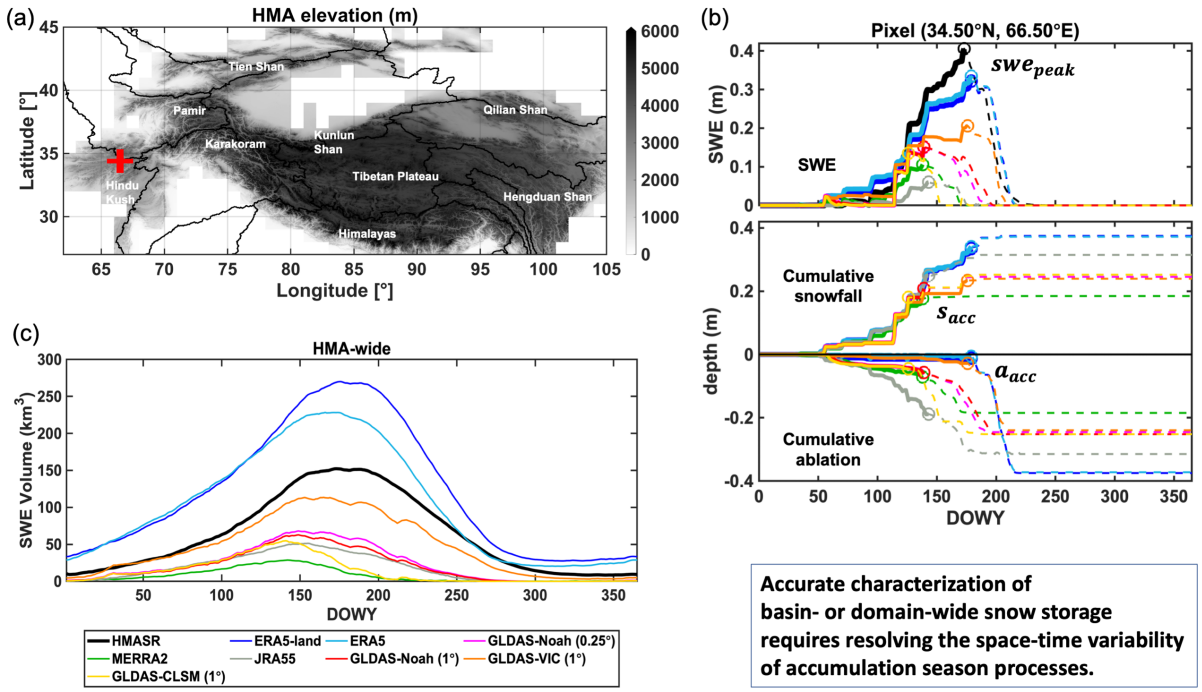

Figure 4.1: a) map of HMASR domain elevation with major watershed boundaries (DEM derived from SRTM as described in Margulis et al. (2019) where the red '+' symbol indicates the location of the pixel shown in (b); b) illustrative example of seasonal cycle of SWE, cumulative snowfall and ablation at a representative pixel (34.5°N, 66.5°E) in WY2017 where the solid lines represent processes leading up to peak SWE (the focus of the work described herein) and the dashed lines are the processes after peak SWE, with the 'o' symbols indicate peak SWE; c) the 17-year climatology of seasonal cycle in HMA-wide SWE volume illustrating how pixel-scale uncertainty across datasets propagate to the full domain seasonal cycle.

As in Liu et al. (2021), the HMASR dataset can be used to derive masks for persistent snow/ice, seasonal snow, and intermittent snow (Figure S1; with intermittent snow defined as pixels with climatological peak SWE below 0.05 m). The persistent snow mask (derived in Liu et al., 2021) is used to remove areas that are likely glacierized or with significant carry-over snow storage from one WY to the next. The focus of this study is on the seasonal and intermittent snow regions, where the distinction is made due to expected differences in accumulation season characteristics. For consistency, we applied the three HMASR masks to all other datasets, by aggregating them from the original HMASR resolution (~500 m) to the coarser resolution grids (Figure S1). The masked areas were carefully examined to make sure they are comparable across datasets (Table S1). In general, the derived seasonal snow area is almost three times as large as the persistent snow/ice area, but only ~35% as large as the intermittent snow area. Most of the seasonal snow is in the northwestern mountain regions (dominated by winter westerlies), while intermittent snow mainly covers the vast area in the central and eastern regions (dominated by summer monsoons).

4.3.2 Accumulation season snow mass balance at the pixel-scale

Snowpack evolution can be characterized as snow mass gain (via solid precipitation, i.e. snowfall) and snow mass loss (via ablation, e.g. snowmelt, sublimation, wind drifting, etc.), which can be represented in terms of mass and energy balance (Liston and Elder, 2006; McCrary and Mearns, 2019). By definition, peak snow storage is associated with snow mass balance processes during the accumulation season, therefore only the accumulation season snow mass gain and loss are examined in this study.

Snow mass balance at the model pixel scale can be described as the relationship between SWE (denoted as *swe* in m), snowfall (*s*, in m/day) and ablation (*a*, in m/day), all expressed in equivalent water depth:

$$\frac{d}{dt} swe = s - a \quad (1)$$

The snow accumulation season is defined at the pixel scale, from DOWY 1 (t_0) up to pixel-wise peak SWE DOWY (t_{peak}; Figure S2) given by:

$$\int_{t_0}^{t_{peak}} \left[\frac{d}{dt} swe\right] dt = \int_{t_0}^{t_{peak}} [s - a] dt \quad (2)$$

$$swe_{peak} = s_{acc} - a_{acc} \quad (3)$$

where swe_{peak} characterizes the net added SWE within the accumulation season at a specific pixel. The s_{acc} and a_{acc} terms denote the cumulative snowfall integrated over the accumulation season, with units of m, respectively. The variables swe_{peak} and s_{acc} are directly obtained from each snow product. Since different LSMs across products include and handle ablation processes differently, a_{acc} is obtained as the residual (similar to Xu et al., 2019):

$$a_{acc} = s_{acc} - swe_{peak} \quad (4)$$

Defining these quantities at the pixel-scale isolates accumulation season processes, where doing so at the basin or larger scale inevitably mixes accumulation season and melt season processes due to elevational gradients within the region examined. Spatial variations in t_{peak} are indicative of seasonal and elevational patterns in climatology, but are also a function of model-specific inputs and process representation (Figure S2).

Figure 4.1b provides an illustrative example of accumulation season mass balance showing the seasonal cycle of SWE, cumulative snowfall and ablation, at a representative pixel (34.5°N, 66.5°E) in WY2017. In this pixel-WY, HMASR has the highest swe_{peak}, with a value of ~0.4 m and a corresponding value for t_{peak} of ~DOWY 180. In comparison, the snow products have swe_{peak} values ranging from ~0.1-0.32 m and t_{peak} values ranging from ~DOWY 125-180. The inter-product uncertainty in swe_{peak} is the result of variability in both snowfall and ablation, with s_{acc}

ranging from ~0.2-0.4 m and a_{acc} ranging from ~ 0.02-0.2 m. Note that this comparison is primarily for illustration due to the large grid size differences among datasets. This is why spatial integration is used (as described below in Section 4.3.3) for the formal intercomparison.

It should also be noted that while most snow products showed consistency between integrated positive SWE increments and snowfall (Figure 4.1b), JRA55 consistently exhibits SWE changes lower than expected relative to snowfall (i.e. data assimilation increments appear to be mostly negative). For this reason, "ablation" (defined herein as the residual between swe_{peak} and s_{acc}) for JRA55 is likely a mix of model-specific ablation processes and non-negligible data assimilation corrections. This explains why JRA55 has among the higher snowfall estimates, but among the lower SWE estimates in Figure 4.1b.

4.3.3 Spatial integration

The focus of this study is to quantitatively compare the seasonal snow storage estimates over the HMA domain as well subregional scales. Due to the disparity in native spatial resolutions from the eight snow products and HMASR, this is mainly achieved through integrating pixel-scale quantities into basin-scale or HMA-scale volumes. Seasonal, intermittent, and persistent snow masks (Figure S1) are applied prior to the integration.

For the three quantities (swe_{peak}, s_{acc} and a_{acc}) in equation (3), the spatially integrated quantities are denoted herein as SWE_{peak}, S_{acc} and A_{acc} (in units of km^3), with the same relationship as characterized as:

$$SWE_{peak} = S_{acc} - A_{acc} \tag{5}$$

It should be noted that A_{acc} is essentially calculated as the residual between S_{acc} and SWE_{peak} based on equation (4) in this work:

$$A_{acc} = S_{acc} - SWE_{peak} \tag{6}$$

The analysis below consists of examining SWE_{peak} across all datasets (including using HMASR as a reference) and additionally S_{acc} and A_{acc} across all snow products.

In addition, the spatially integrated precipitation is noted as P_{acc}, and the spatially average air temperature is noted as T_{acc}, during accumulation season (up until t_{peak}) over the HMA-scale or basin scales. Herein the 10 largest watersheds in HMA are examined, which are delineated based on HydroSHEDS (Lehner et al., 2008) and shown in Figure 4.1a.

Spatial integration over elevation bands is also performed in this work. The DEM for each dataset (at the native resolution) is shown for a representative tile 34°N, 66°E in Figure S3a. The hypsometry over the whole domain (Figure S3b) shows how the areal distribution of elevation varies across datasets. For elevational distributions of variables (e.g. SWE_{peak} and S_{acc}), the native DEMs for each dataset were used to integrate into volumes by discretizing elevation bands using intervals of 1000 m (centered on 1500, 2500, 3500, 4500, and 5500 m) . Relative to HMASR, all snow product DEMs seem to have less area below 2000 m or above 3500 m, and more area in between (2000 – 3500 m). The hypsometry is generally consistent above 3500 m, and most different around 2500 m across snow products, with GLDAS (1°) product showing the highest area, followed by JRA55 and MERRA2, while ERA5 and GLDAS (0.25°) show the least area (yet slightly higher than HMASR).

4.3.4 Linear regression

As shown in many previous studies, precipitation (snowfall) is often regarded as the key variable affecting peak SWE estimation (Clark et al., 2011; Magnusson et al., 2015; Xu et al., 2019). Along these lines, we use a simple linear regression to examine the relationship between SWE_{peak} and S_{acc}:

$$SWE_{peak} = \beta * S_{acc} + \varepsilon \quad (7)$$

where SWE_{peak} and S_{acc} are available for each snow product and each WY. In the analysis below, the regression is used to examine both global (i.e. across all snow products and WYs) and local (i.e. for a single snow product across all WYs) variations.

The β term is the regression coefficient (slope), and is derived either (β_{global}) or locally (β_i). The slope physically represents the fraction of cumulative snowfall that remains in the snowpack at t_{peak}. In the limit of no ablation the slope would be ~1, while the occurrence of accumulation season ablation will generally lead to values < 1. The ε term is the random noise, which is assumed to be independent of the predictor (S_{acc}). To avoid collinearity, A_{acc} is not explicitly included as a predictor in the linear regression, as it is simply computed as the residual between the other two variables (Equation (6)). The coefficient of determination (R^2) is often used to measure the goodness of fit for the linear model, and its value can be interpreted as the fraction of the explained variance. The above approach provides a mechanism to determine the relative role of snowfall vs. ablation in contributing to peak snow storage (through the slope) as well as explain the variation in peak storage relative to snowfall. Note that JRA55 and HMASR data were excluded in the linear regression, since their snowfall data is either not available (HMASR) or inconsistent with SWE (JRA55 due to significant data assimilation increments in SWE).

4.4 Results and Discussion:

The results are organized as follows: Section 4.4.1 presents the uncertainty in peak seasonal snow water storage over HMA and its watersheds; Section 4.4.2 examines the driver of peak SWE uncertainty from accumulation season snowfall and ablation variations.

4.4.1 Uncertainty in peak seasonal snow storage over HMA and its watersheds

4.4.1.1 HMA-scale

Characterizing pixel-wise peak SWE and its timing (Figure 4.1b) is important because any uncertainties propagate to basin or domain-averaged snow storage quantities. To first illustrate the domain-wide impacts, Figure 4.1c shows the climatological (17-year average) integrated SWE volume time series over HMA, where the peak storage varies from 29 km^3 (MERRA2) to 270 km^3 (ERA5-land), and peak timing varies from DOWY 141 (GLDAS-CLSM) to DOWY 176 (ERA5-land). In terms of the magnitude, ERA5-land and ERA5 show the highest seasonal storage followed by HMASR, while GLDAS products show lower seasonal storage (with an order, from highest to lowest, of GLDAS-VIC, GLDAS-Noah (0.25°), GLDAS-Noah (1°) and GLDAS-CLSM). JRA55 and MERRA2 show the least seasonal storage. Since peak snow storage and its timing are direct indicators of snow-derived water availability, the results suggest large uncertainty across snow products. However, this domain-wide integral time series is the result of pixel-scale accumulation processes (e.g., Figure 4.1b) with spatially varying accumulation seasons (Figure S2). Hence to fully understand the uncertainty, all results to follow focus on the pixel-wise peak snow storage (SWE_{peak}) and the processes leading to that storage (S_{acc} and A_{acc}).

The estimates of SWE_{peak} across all datasets are shown in Table 4.2, which corresponds to an overall estimate of: 161 $km^3 \pm 102$ km^3 (excluding HMASR as a standalone dataset for evaluation) illustrating the very large uncertainty across snow products. When partitioned into seasonal and intermittent snow the estimates are: 110 $km^3 \pm 74$ km^3 and 51 $km^3 \pm 28$ km^3, respectively. The ERA5-land and ERA5 snow products, with volumes of 341 km^3 and 288 km^3, exhibit larger values than HMASR (239 km^3), corresponding to 43% and 20% more snow respectively. The remaining snow products exhibit less snow storage than HMASR. The GLDAS estimates range from 25-59%

less snow than HMASR with GLDAS-VIC (179 km^3), GLDAS-Noah, (120 km^3 and 114 km^3 for 0.25° and 1° respectively), and GLDAS-CLSM (98 km^3) in order of highest to lowest estimates. The JRA55 and MERRA2 products exhibit the least amount of SWE_{peak} with 93 km^3 (61% less than HMASR) and 54 km^3 (77% less than HMASR), respectively. When the snow products are compared collectively to HMASR over the full HMA domain, the mean difference (MD) in SWE_{peak} is -33% with a root mean square difference (RMSD) of 52%. In seasonal snow regimes, there is a MD of -47% and RMSD of 58%. In intermittent snow regimes, there is a MD of 70% and RMSD of 113%. This highlights the qualitative differences in snow regime (underestimate in seasonal vs. overestimate in intermittent) that are somewhat cancelled out when considered together.

Table 4.2: 17-year climatology of SWE_{peak} and the percent difference compared to HMASR, over the full HMA domain and over seasonal and intermittent snow regimes.

	HMA		Seasonal		Intermittent	
Dataset	SWE_{peak} (km^3)	% difference with HMASR	SWE_{peak} (km^3)	% difference with HMASR	SWE_{peak} (km^3)	% difference with HMASR
HMASR	239	-	210	-	30	-
ERA5-land	341	43%	249	19%	93	210%
ERA5	288	20%	198	-5%	90	200%
GLDAS-Noah (0.25°)	120	-50%	84	-60%	36	20%
MERRA2	54	-77%	35	-83%	18	-38%
JRA55	93	-61%	64	-69%	29	-3%
GLDAS-Noah (1°)	114	-53%	76	-64%	37	25%
GLDAS-VIC (1°)	179	-25%	113	-46%	65	119%
GLDAS-CLSM (1°)	98	-59%	61	-71%	38	26%
Mean (excluding HMASR)	161	-	110	-	51	-
Standard Deviation (excluding HMASR)	102	-	74	-	28	-
MD	-	-33%	-	-47%	-	70%
RMSD	-	52%	-	58%	-	113%

4.4.1.2 Basin-scale

Figure 4.2 depicts the climatology of the spatial distribution of swe_{peak} for each dataset. All datasets exhibit coherent spatial patterns with the highest amount of snow estimated in the seasonal snow regimes and shallow or negligible amounts in the intermittent snow regimes; these patterns are consistent with previous studies (Terzago et al., 2014; Bian et al., 2019; Orsolini et al., 2019). Despite the consistency in spatial patterns across datasets, there are large differences in magnitude. This becomes clear when integrated across different basins (Figure 4.3). By comparing to the seasonal/intermittent snow classification (Figure S1), we categorize the ten basins into seasonal snow dominated basins (Syr Darya, Amu Darya, Tarim and Indus), mixed basins (Ganges-Brahmaputra) and intermittent snow dominated basins (e.g. Inner Tibetan Plateau, Salween, Mekong, Yangtze and Yellow).

In general, at the basin scale, relative estimates of SWE_{peak} across snow products are qualitatively consistent with the HMA-wide results. ERA5/ERA5-land products show more SWE_{peak} compared to HMASR, with the least overestimation (up to 25%) in seasonal snow basins, moderate overestimation (~60%) in mixed basins, and the most overestimation (~100%) in intermittent snow basins. In contrast, GLDAS products generally exhibit less SWE_{peak} than HMASR, with the most underestimation in the seasonal snow and mixed basins (up to 60% and ~75%, respectively), and the least underestimation (up to ~25%) in the intermittent snow basins, with the exception that it overestimates SWE_{peak} (by 82%) in the Inner Tibetan Plateau. MERRA2 and JRA55 consistently show less SWE_{peak} (both between 50% to 80% underestimation) than HMASR. The variations within the ERA5/ERA5-land products are found to be larger in seasonal snow basins than intermittent snow basins, while the GLDAS group shows the opposite.

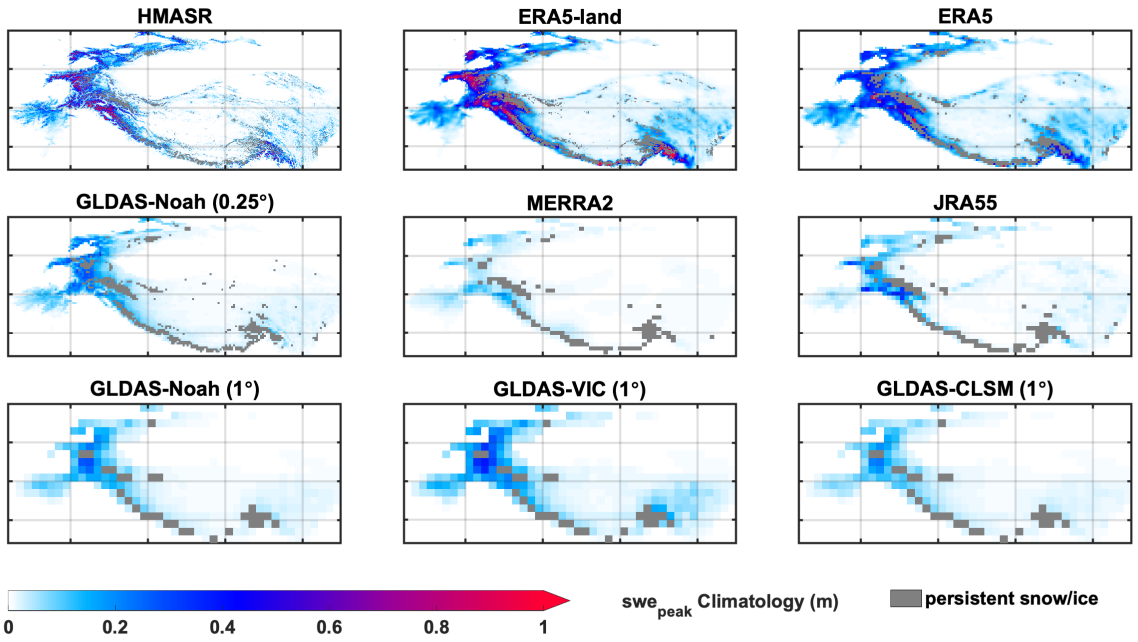

Figure 4.2: The 17-year climatology of pixel-wise peak SWE (swe_{peak}), with persistent snow/ice pixels masked out (grey).

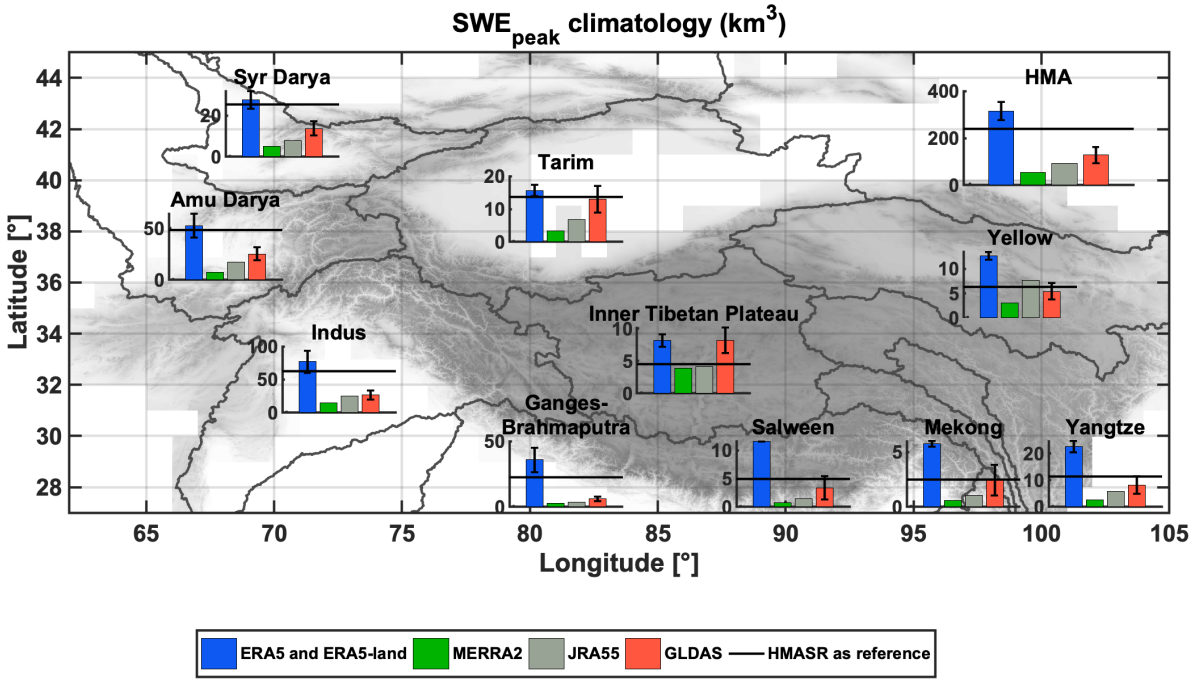

Figure 4.3: The 17-year climatology of peak SWE volume (SWE_{peak}) in each basin (with HMASR SWE shown with horizontal black line). The snow products are grouped into 4 main sets (ERA5 and ERA5-land, MERRA2, JRA55 and GLDAS), with the average SWE_{peak} (bar plot) and the standard deviation (error bars) shown for the ERA5 and GLDAS groups.

4.4.2 Drivers of peak SWE and their variation across snow products

4.4.2.1 Variations in accumulation season snowfall and ablation

As described in Equation (5), SWE_{peak} is the result of cumulative snowfall and ablation through the accumulation season (S_{acc} and A_{acc}). The variability in S_{acc} and A_{acc} climatology between snow products is characterized in Figure 4.4 to illustrate their relative influence on SWE_{peak} variability. Overall, there exists large variations in S_{acc} and A_{acc} estimates across the existing snow products. S_{acc} is generally largest in ERA5/ERA5-land products, and smallest in MERRA2/GLDAS products, with the mean and uncertainty characterized by 335 km^3 $\pm$ 148 km^3 in the entire HMA, 178 km^3 $\pm$ 83 km^3 in seasonal snow regimes and 157 km^3 $\pm$ 67 km^3 in

intermittent snow regimes. A_{acc} is also quite variable (and a significant fraction of S_{acc}) across snow products, indicating that ablation during the accumulation season is a non-negligible factor in determining the SWE_{peak}. Specifically, between 40% (ERA5-land) and 65% (MERRA2) of snowfall is lost to ablation during the accumulation season, with the uncertainty characterized by $51\% \pm 9\%$. The snowfall loss to ablation is less in seasonal snow regimes, but the ratio still varies significantly across products (from 17% in ERA5-land to 55% in MERRA2, or $37\% \pm 13\%$ across snow products). In intermittent snow regimes, the snowfall loss to ablation is large but more consistent across snow products (from 58% in GLDAS-VIC to 76% in MERRA2; $67\% \pm 7\%$), during the accumulation season.

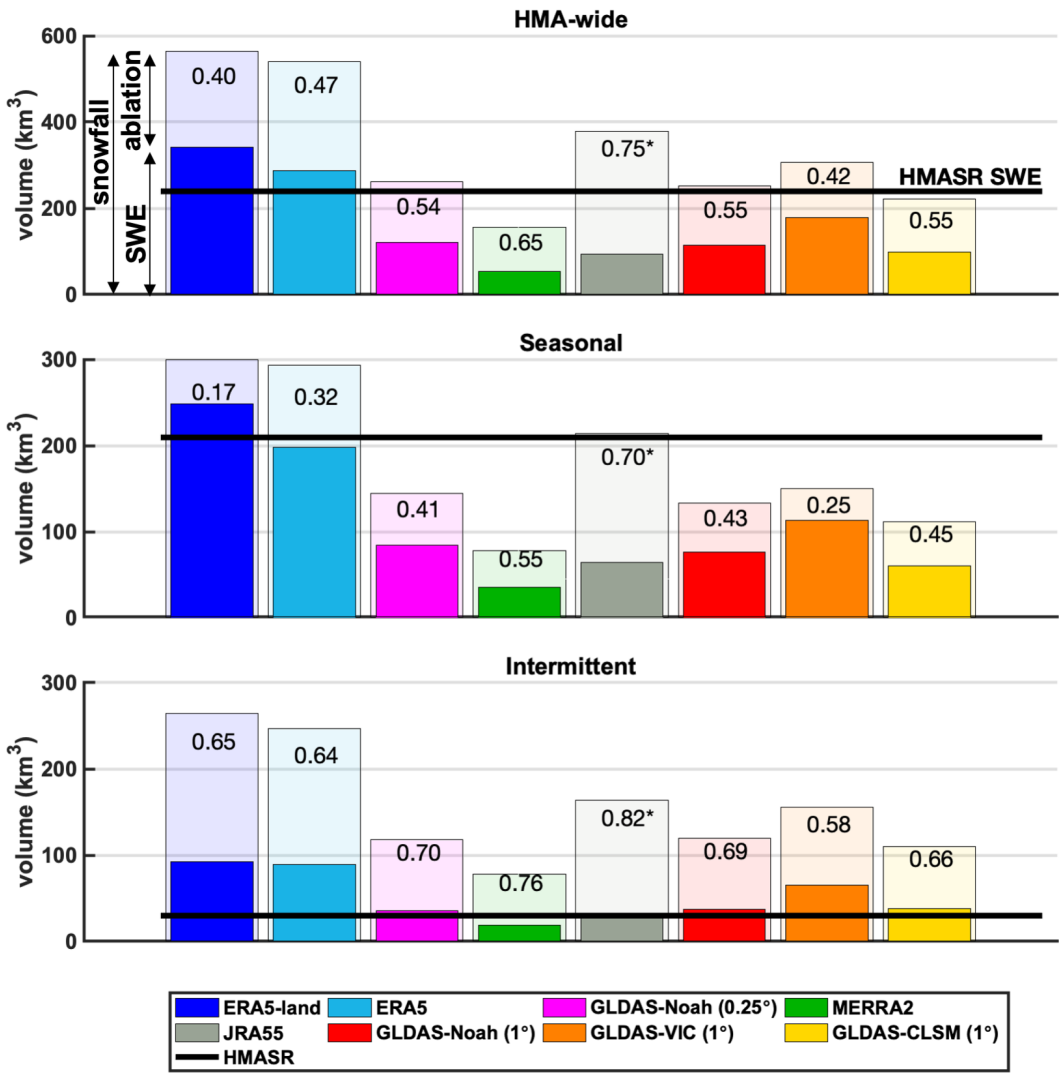

Figure 4.4: The 17-year climatology of peak SWE volume (SWE_{peak}, solid bars), and accumulation season snowfall volume (S_{acc}, shaded bars), integrated over HMA (top panel) as well as over seasonal (middle panel) and intermittent snow (bottom panel) regimes. HMASR SWE is provided as a reference (solid black horizontal line). The text labels in each bar plot indicate the fraction of cumulative snowfall lost to ablation. JRA55 ablation fraction is displayed here but not included in the discussion due to its 'ablation' being overestimated because it includes the effect of snow data assimilation updates.

The elevational distribution of S_{acc}, A_{acc} and SWE_{peak} climatology over the full HMA domain are depicted in Figure 4.5, with volumes normalized by total S_{acc} to present the volumetric fraction. Given the significant differences in snowfall across snow products, the normalization reflects how, for the same amount of snowfall, each snow product distributes snowfall across elevation and how that fraction is partitioned into A_{acc} and SWE_{peak}. The elevational distribution over the full HMA domain is presented here, with a generally consistent pattern in the elevation distribution over seasonal and intermittent snow regimes. For convenience, we define the elevation bands centered on 2500 m, 3500 m and 4500 m as lower, mid and higher elevations herein.

The fractional S_{acc} distribution over elevation is generally consistent across snow products, except that MERRA2 exhibits a slightly higher fraction at lower elevations and a lower fraction at higher elevations. ERA5 and ERA5-land exhibit higher S_{acc} fractions at mid elevations (5% more than MERRA2) and lower fractions at higher elevations (comparable to MERRA2). The GLDAS products exhibits the lowest fractions at lower elevations (~ 5-8% less than MERRA2) but the highest fractions at higher elevations (~8% more than MERRA2).

The fractional A_{acc} distribution is significantly more distinct across snow products. At lower and mid elevations, both ERA5-land and GLDAS-VIC stand out as showing the lowest fractions, where ERA5 and the other GLDAS products shows moderate fractions (8% more than ERA5-land), and MERRA2 shows the highest fraction (20% more than ERA5-land). At higher elevations, ERA5-land and GLDAS-VIC still show the least fractional A_{acc}, but ERA5 exhibits a comparable fraction compared to ERA5-land, and the other GLDAS products and MERRA2 shows the highest fractions (8% more than ERA5-land). The extremely low ablation in ERA5-land and ERA5 at higher elevations is described in Hersbach et al. (2020) and attributed to its single layer snow model not producing enough melt. The three GLDAS products only exhibit minor difference with

~2% less fractional A_{acc} in GLDAS-Noah (0.25°) and 1% less fractional A_{acc} in GLDAS-Noah (1°) compared to GLDAS-CLSM at lower elevations.

The elevational distribution of fractional SWE_{peak} is a direct result of fractional S_{acc} and A_{acc}. In general, ERA5-land exhibit the highest fractional SWE_{peak}, with MERRA2 showing the lowest fraction, primarily because MERRA2 consistently has higher fractional A_{acc} than ERA5-land. Their differences are largest (13%) at mid elevations where MERRA2 exhibits less fractional S_{acc}, and smallest (5%) at low elevations where MERRA2 exhibits more fractional S_{acc}. Compared to ERA5-land, GLDAS-VIC shows ~7% less fractional SWE_{peak} at mid elevations, but ~6% more at high elevations, primarily because the difference in fractional S_{acc} distribution. Again, the other three GLDAS products exhibit a relatively consistent distribution in fractional SWE_{peak}, except that the 0.25° product shows a slightly higher fraction (~3%) at mid elevations due to the fractional S_{acc} difference compared to other products. GLDAS also exhibits more fractional SWE_{peak} than MERRA2, with the difference largest (8%) at high elevations where GLDAS obtains more fractional S_{acc} but equivalent fractional A_{acc}, and smallest (<1%) where GLDAS obtains less fractional S_{acc} and less fractional A_{acc}. These highlight the important role of ablation in removing snowfall differently with elevation over the accumulation season, leading to a distinct distribution in fractional SWE_{peak} rather than just reproducing the fractional S_{acc} distribution.

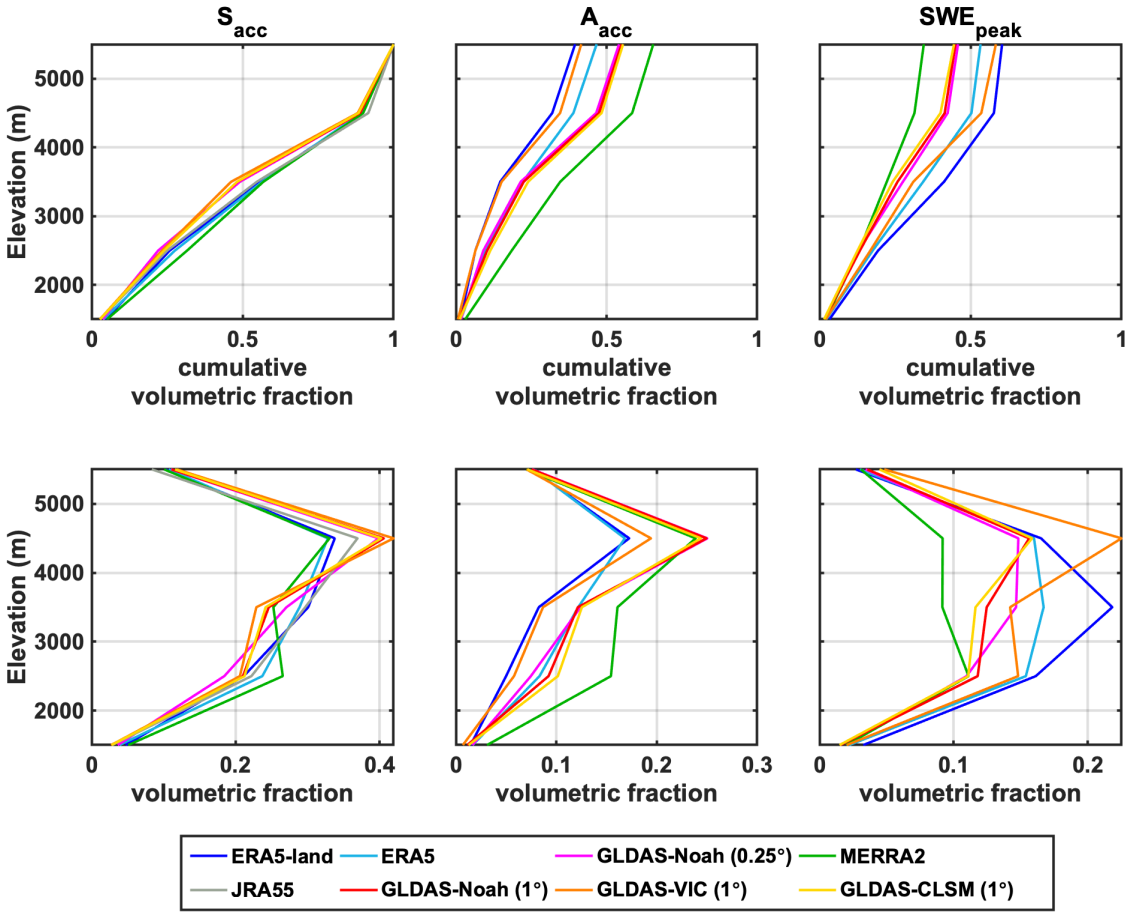

Figure 4.5: Volumetric fraction of accumulation season snowfall (S_{acc}), ablation (A_{acc}) and peak SWE (SWE_{peak}), integrated over 1000-m elevation bins (centered on 1500, 2500, 3500, 4500, and 5500 m) over the full HMA domain. The fractional distribution is obtained for each snow product by normalizing the distribution by the product-specific total S_{acc} across all elevations. The top panel displays the cumulative volumetric fraction across elevation bins, and the bottom panel displays the absolute volumetric fraction within elevation bins. Note that the fractional ablation and SWE in JRA55 are not displayed here, due to its 'ablation' being overestimated because it includes the effect of snow data assimilation updates.

4.4.2.2 Explaining peak SWE variation from accumulation season snowfall/ablation

To explain peak SWE variations across and within snow products, linear regression (as described in Section 4.3.4) was applied across snow products and/or WYs. Over the full HMA domain, a strong linear dependence between the interannual SWE_{peak} and S_{acc} is clearly illustrated in Figure 4.6. A large range of S_{acc} values are observed (ranging from 100 – 700 km^3), with a notable gap between GLDAS (ranging from 200 – 400 km^3) and ERA5/ERA5-land (ranging from 500 – 700 km^3). The global regression slope (β_{global}) is 0.54, indicating that, during the accumulation season, ~54% of snowfall goes into the SWE_{peak}, while the other 46% is lost through ablation. This partitioning is higher in seasonal snow regimes, where ~71% of snowfall goes into peak SWE and 29% instead is lost via ablation. In intermittent snow regimes ~35% of snowfall goes into peak SWE and 65% instead is lost via ablation. These diagnosed fractions from multi-WY and multi-product analysis (Figure 4.6) are consistent with those derived from the climatology (Figure 4.4).

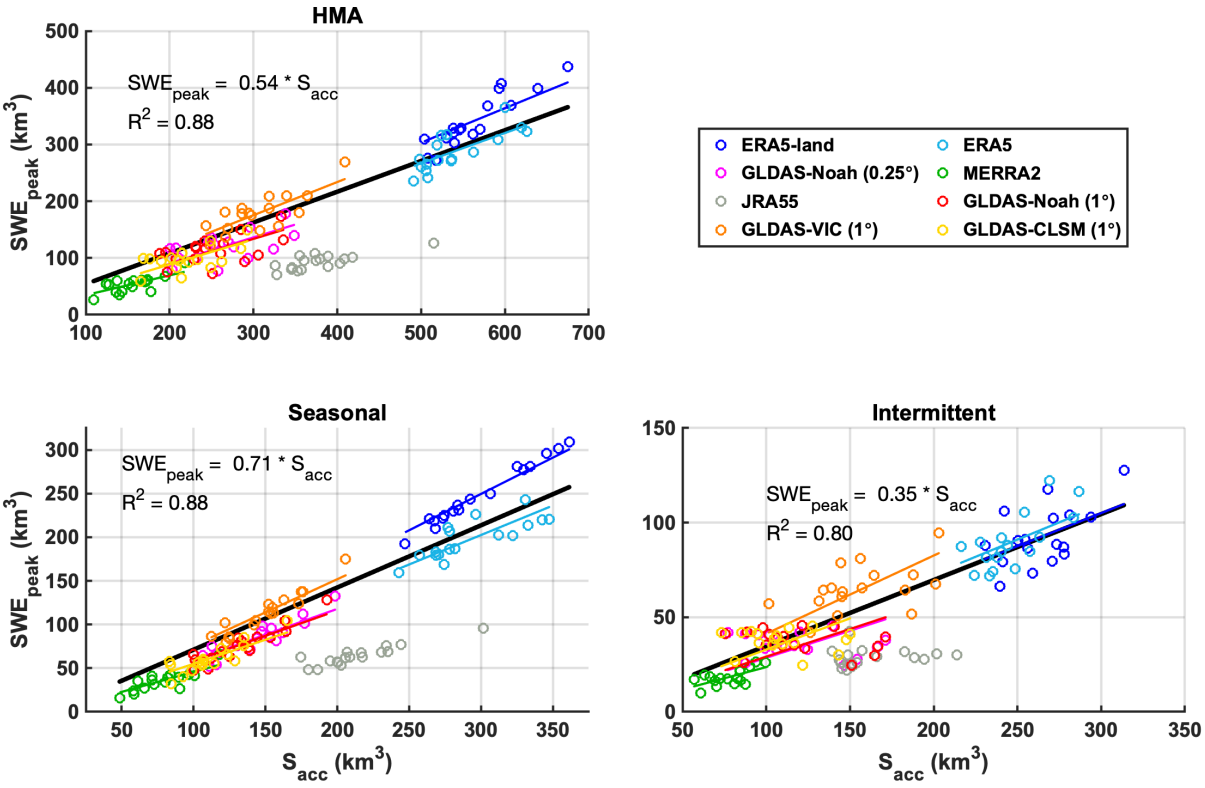

Figure 4.6: Regression of peak SWE volume (SWE_{peak}) and accumulation season snowfall (S_{acc}) across WYs (WY 2001-2017), with volumes integrated over the full HMA domain, as well as the seasonal and intermittent snow regimes, respectively. Note that JRA55 is displayed here but not included in the global linear regression due to its 'ablation' being overestimated because it includes the effect of snow data assimilation updates.

The coefficient of determination (R^2) is 0.88, 0.88 and 0.80 for the full HMA domain, seasonal snow regime and intermittent snow regime, respectively (Figure 4.6). Such values are informative in 1) revealing the strong linear dependence of SWE_{peak} and S_{acc} across all datasets and all WYs, and 2) that over 80% of SWE_{peak} uncertainty is explained by S_{acc} variability, where the other 20% or less is explained by A_{acc} variations.

Besides viewing all datasets as a large sample, we also evaluated the interannual variability within each snow product and examined product-specific linear regression results. The individual regression slopes are also distinct, as illustrated in Figure 4.6 (and tabulated in Table S2). Compared to the global slope values, ERA5-land and GLDAS-VIC exhibit higher slopes, while MERRA2 and the other GLDAS products exhibit lower slopes. It is worthwhile to note that the linear dependence of SWE_{peak} and S_{acc} are very strong in seasonal snow (with R^2 ranging from 0.62 to 0.94), and much weaker in intermittent snow (with R^2 ranging from 0.25 to 0.48), when examining individual snow product as tabulated in Table S2. This can be attributed to intermittent snow being more influenced by ablation, which introduces additional noise into the snowfall-peak SWE relationship.

Given the large range in S_{acc} across snow products, including the noticeable gap between ERA5/ERA5-Land and the other snow products (GLDAS and MERRA2), we also separately regressed SWE_{peak} vs. S_{acc} for these two groups of snow products Figure S4). In doing so, the R^2 values drop to 58% and 43% respectively (from the global value of 0.88). These lower R^2 values may reveal that A_{acc} is a more important source of uncertainty (explaining 42% and 57% of SWE_{peak} uncertainty, respectively), when examined in certain subsets of products, even though S_{acc} is the most dominant factor in explaining the wide range of SWE_{peak} across all products.

The results above indicate (not surprisingly) that S_{acc} variations are the primary factor in explaining SWE_{peak} variations, with ablation playing a secondary (but important) role. To decipher the degree to which those variations are explained by precipitation vs. rain-snow partitioning across snow products, the accumulation season snowfall volume (S_{acc}) was regressed against precipitation volume (P_{acc}) (Figure S5). It is found that S_{acc} shows very high linear

dependence on P_{acc} (R^2 up to 0.96), and there is relatively minor difference when adding accumulation season air temperature into the regression (R^2 slightly increased to ~0.98).

4.5 Conclusion:

Accurate knowledge of peak snow water storage is a necessary condition for predicting available water in warm-season runoff. Results in this study confirm that our current state of knowledge of this basic parameter in HMA is highly uncertain. Eight globally available snow products were examined over HMA, with the use of HMASR as a reference, to specifically analyze accumulation season processes. The key findings are:

1) The SWE_{peak} climatology across global snow products was found to be 161 km^3 $\pm$ 102 km^3, with varying uncertainty levels for seasonal (110 km^3 $\pm$ 74 km^3) vs. intermittent (51 km^3 $\pm$ 28 km^3) snow regimes. Compared to HMASR, the other snow products on average underestimate SWE_{peak} by 33% (MD) with a RMSD of 52% over the entire HMA. The error and uncertainty vary across different watersheds, where on average, the snow products underestimate seasonal snow (by 47%) and overestimate intermittent snow (by 70%), compared to HMASR.
2) There exists large variability in the S_{acc} and A_{acc} climatology. S_{acc} climatology was found to be 335 km^3 $\pm$ 148 km^3. The fraction of cumulative snowfall loss via ablation leading up to SWE_{peak} is 51% $\pm$ 9%. The fraction differs between seasonal (37% $\pm$ 13%) and intermittent (67% $\pm$ 7%) snow regimes. Both S_{acc} and A_{acc} play an important role in determining SWE_{peak} distribution both spatially and over different elevation ranges.
3) Uncertainty in inter-product peak snow storage estimates across all snow products is primarily explained by S_{acc} (88%) with 88% and 80% in seasonal and intermittent snow regimes respectively. Across years and snow products, 54% of S_{acc} goes into the SWE_{peak}

and ~46% is lost through ablation on average, during the accumulation season. In seasonal snow regimes, ~71% of S_{acc} goes into SWE_{peak} and ~29% instead is lost via A_{acc}. In intermittent snow regimes, ~35% of snowfall goes into SWE_{peak} and ~65% instead is lost via A_{acc}.

The factors affecting S_{acc} are examined in this work, where precipitation (and not temperature) is found to play the dominant role when considering inter-product differences. As indicated in many previous studies (e.g. Xu et al., 2019; Xiao et al., 2021), land surface model and meteorological forcings (e.g. air temperature and shortwave radiation) could be additional key sources contributing to the variability in snow ablation. The main drivers for snow ablation variability during the accumulation season are not explored in this work, as they are typically intertwined with individual model physics, but should be investigated in future work.

We also provide the caveat that the relative importance of S_{acc} in explaining SWE_{peak} uncertainty is also sensitive to the ensemble of datasets chosen. The explanatory power of accumulation season snowfall in SWE_{peak} across all product-WYs is partly a function of the wide range (large uncertainty) of precipitation (and snowfall). A_{acc} was found to explain more SWE_{peak} variation when the snowfall uncertainty was reduced by considering subsets of snow products.

To reduce the uncertainty in estimates of snow storage over HMA will require improved characterization of both snowfall and ablation processes and/or better measurements of SWE to constrain models during the accumulation season. Reducing accumulation season uncertainty is key to also better understanding and constraining (i.e. by providing the proper initial condition of stored snow) melt season processes that control snowmelt rates, infiltration, and runoff that are likely also highly uncertain, but the melt season uncertainties are, in part, masked by the significant uncertainty in peak SWE estimates.

4.6 Supporting information

This section serves as an appendix containing supporting information figures and tables for Chapter 4. The numbering system used is sequential within this section, but using a prefix "S" to indicate that these figures and tables constitute supporting information.

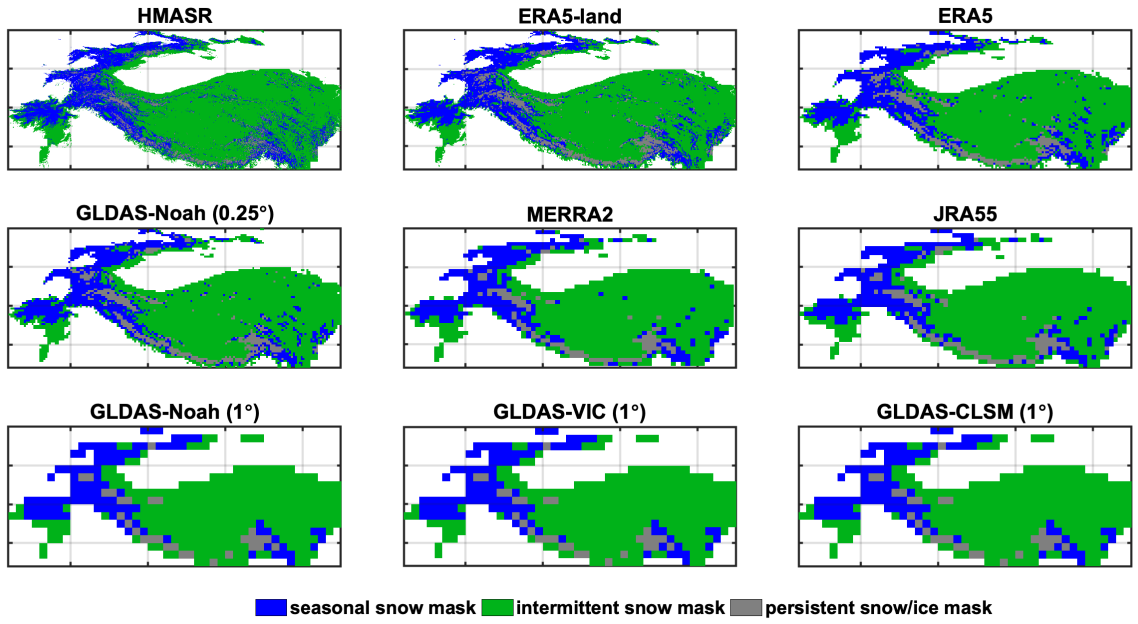

Figure S1: The derived seasonal snow, intermittent snow, and persistent snow/ice masks shown at the native resolution of each dataset.

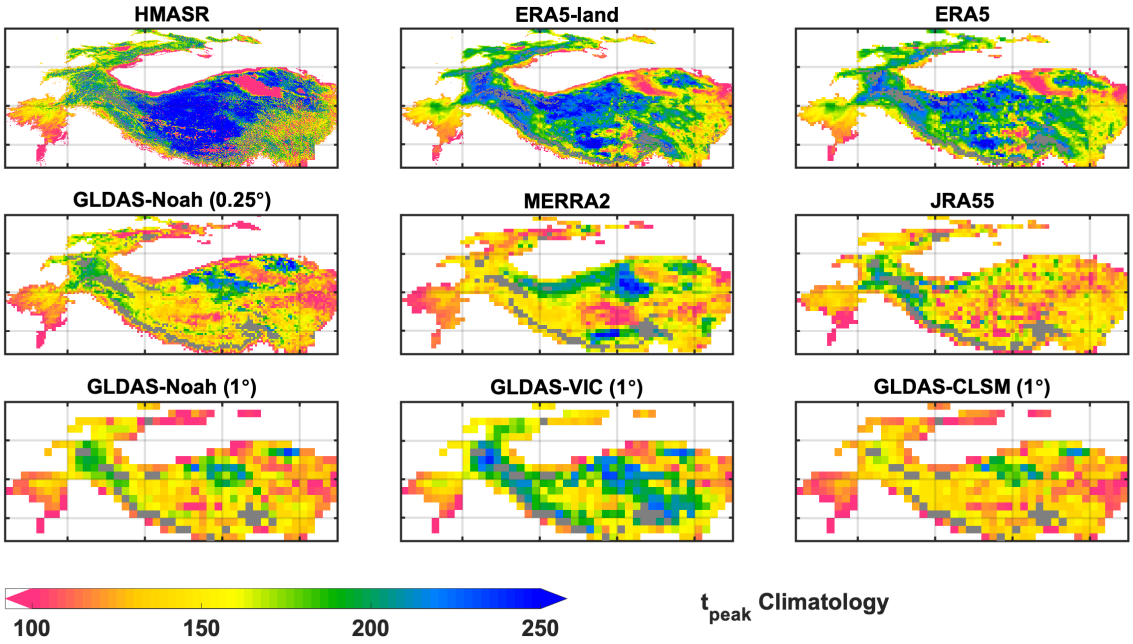

Figure S2: Maps of the 17-year climatology of pixel-wise peak SWE DOWY (t_{peak}) for each dataset.

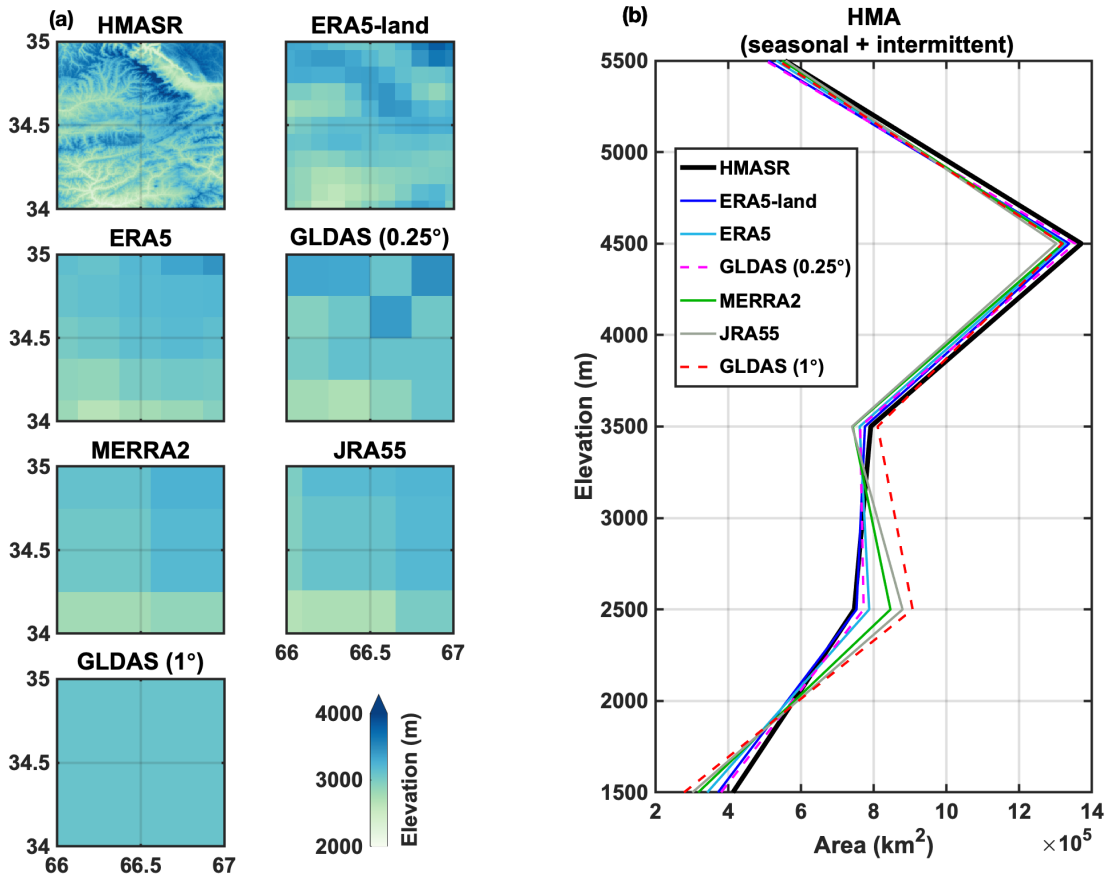

Figure S3: Illustration of dataset-specific a) DEMs for a representative tile (34°N, 66°E) at the native resolution and b) hypsometry over the HMA (masked with seasonal and intermittent snow areas shown in Figure S1), integrated over 1000-m elevation bins (centered on 1500, 2500, 3500, 4500, and 5500 m).

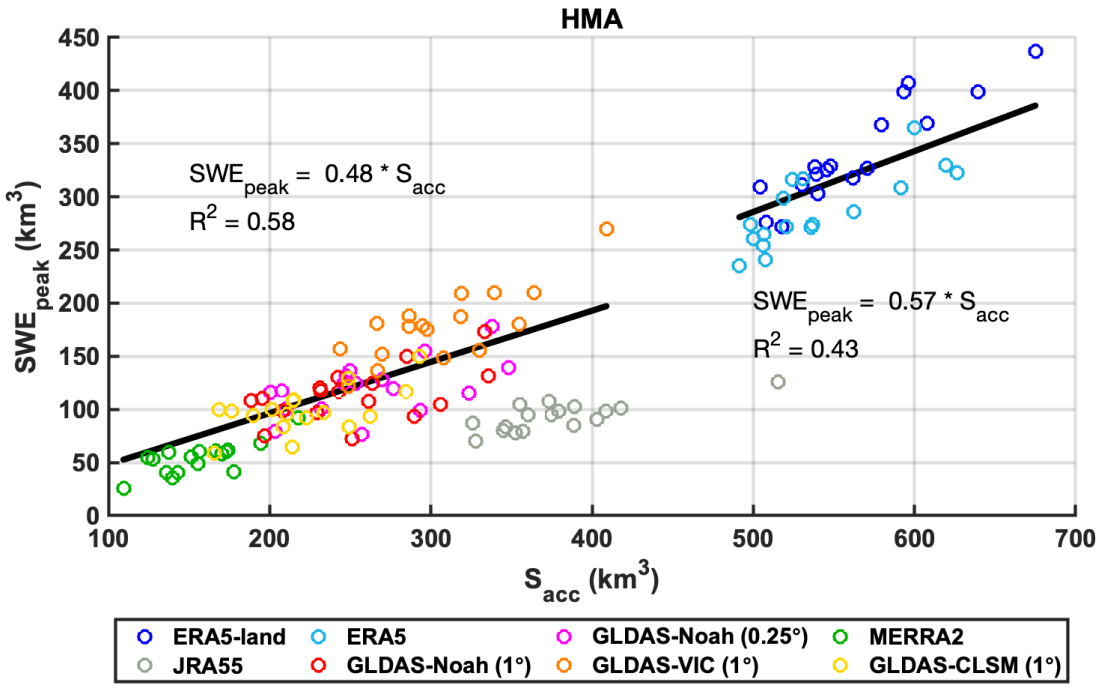

Figure S4: Regression of peak SWE volume (SWE_{peak}) and accumulation season snowfall (S_{acc}) across WYs (WY 2001-2017), with volumes integrated over the full HMA domain. Regression is performed over two subsets of datasets (subset 1: GLDAS products and MERRA2, subset 2: ERA5 and ERA5-land).

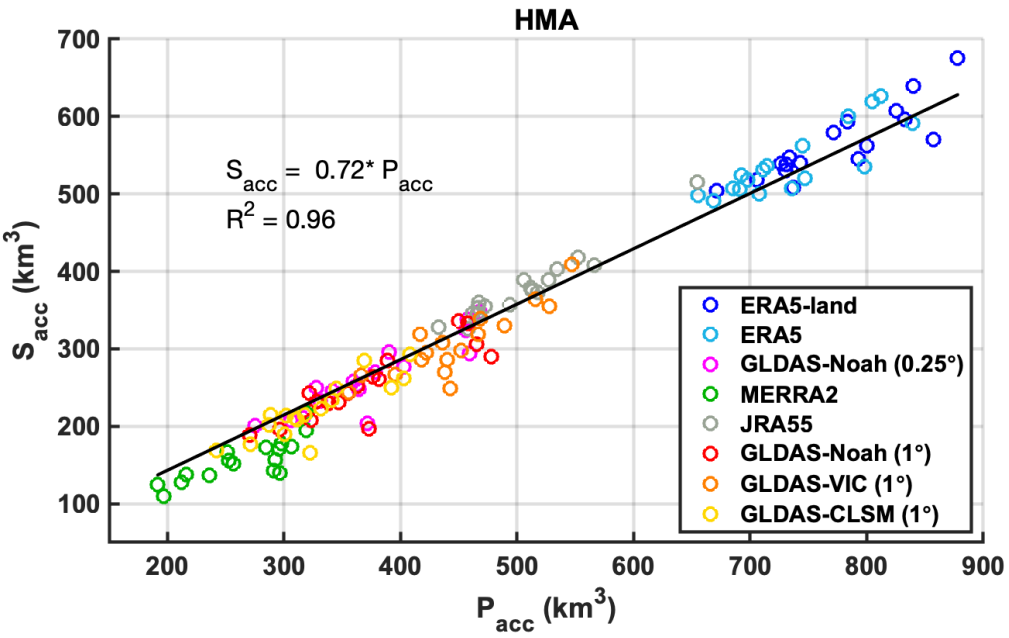

Figure S5: Regression of accumulation season snowfall (S_{acc}) vs. precipitation (P_{acc}) across WYs (WY 2001-2017), with volumes integrated over the full HMA domain.

Table S1: Total masked domain area and areas of seasonal snow, intermittent snow, and persistent snow/ice in all datasets.

Dataset	Total masked domain area (10^6 km^2)	Seasonal Snow Area (10^6 km^2)	Intermittent Snow Area (10^6 km^2)	Persistent snow/ice area (10^6 km^2)
HMASR	4.14	1.00	2.88	0.26
ERA5-land	4.13	0.97	2.78	0.38
ERA5	4.11	0.98	2.77	0.36
GLDAS-Noah (0.25°)	4.14	0.87	2.90	0.37
MERRA2	4.10	0.88	2.90	0.32
JRA55	4.14	0.97	2.81	0.35
GLDAS-Noah (1°)	4.15	0.95	2.90	0.30
GLDAS-VIC (1°)	4.15	1.01	2.84	0.30
GLDAS-CLSM (1°)	4.15	1.06	2.79	0.30

Table S2: Linear regression statistics of slope (β) and R^2, from global and snow product specific regressions. Note that JRA55 results are only displayed here but not included in the global linear regression due to its 'ablation' being overestimated because it includes the effect of snow data assimilation updates.

	Slope (β)			R^2		
	HMA-wide	Seasonal	Intermittent	HMA-wide	Seasonal	Intermittent
Global	**0.54**	**0.71**	**0.35**	**0.88**	**0.88**	**0.80**
ERA5-land	0.61	0.83	0.35	0.58	0.94	0.25
ERA5	0.53	0.67	0.36	0.53	0.70	0.32
GLDAS-Noah (0.25°)	0.45	0.59	0.29	0.48	0.76	0.36
MERRA2	0.35	0.46	0.24	0.48	0.62	0.42
JRA55	0.25	0.30	0.17	0.61	0.77	0.33
GLDAS-Noah (1°)	0.45	0.58	0.29	0.46	0.76	0.35
GLDAS-VIC (1°)	0.58	0.76	0.41	0.60	0.83	0.48
GLDAS-CLSM (1°)	0.44	0.55	0.33	0.46	0.66	0.37

4.7 Bibliography

Armstrong, R. L., Rittger, K., Brodzik, M. J., Racoviteanu, A., Barrett, A. P., Khalsa, S.-J. S., Raup, B., Hill, A. F., Khan, A. L., Wilson, A. M., Kayastha, R. B., Fetterer, F., & Armstrong, B. (2019). Runoff from glacier ice and seasonal snow in High Asia: Separating melt water sources in river flow. *Regional Environmental Change*, *19*(5), 1249–1261. https://doi.org/10.1007/s10113-018-1429-0

Bian, Q., Xu, Z., Zhao, L., Zhang, Y.-F., Zheng, H., Shi, C., Zhang, S., Xie, C., & Yang, Z.-L. (2019). Evaluation and Intercomparison of Multiple Snow Water Equivalent Products over the Tibetan Plateau. *Journal of Hydrometeorology*, *20*(10), 2043–2055. https://doi.org/10.1175/JHM-D-19-0011.1

Bookhagen, B., & Burbank, D. W. (2010). Toward a complete Himalayan hydrological budget: Spatiotemporal distribution of snowmelt and rainfall and their impact on river discharge. *Journal of Geophysical Research: Earth Surface*, *115*(F3). https://doi.org/10.1029/2009JF001426

Bormann, K. J., Brown, R. D., Derksen, C., & Painter, T. H. (2018). Estimating snow-cover trends from space. *Nature Climate Change*, *8*(11), 924–928. https://doi.org/10.1038/s41558-018-0318-3

Dozier, J., Bair, E. H., & Davis, R. E. (2016). Estimating the spatial distribution of snow water equivalent in the world's mountains. *WIREs Water*, *3*(3), 461–474. https://doi.org/10.1002/wat2.1140

Gelaro, R., McCarty, W., Suárez, M. J., Todling, R., Molod, A., Takacs, L., Randles, C. A., Darmenov, A., Bosilovich, M. G., Reichle, R., Wargan, K., Coy, L., Cullather, R., Draper, C., Akella, S., Buchard, V., Conaty, A., da Silva, A. M., Gu, W., … Zhao, B. (2017). The

Modern-Era Retrospective Analysis for Research and Applications, Version 2 (MERRA-2). *Journal of Climate*, *30*(14), 5419–5454. https://doi.org/10.1175/JCLI-D-16-0758.1

Hersbach, H., Bell, B., Berrisford, P., Hirahara, S., Horányi, A., Muñoz-Sabater, J., Nicolas, J., Peubey, C., Radu, R., Schepers, D., Simmons, A., Soci, C., Abdalla, S., Abellan, X., Balsamo, G., Bechtold, P., Biavati, G., Bidlot, J., Bonavita, M., … Thépaut, J.-N. (2020). The ERA5 global reanalysis. *Quarterly Journal of the Royal Meteorological Society*, *146*(730), 1999–2049. https://doi.org/10.1002/qj.3803

Huning, L. S., & AghaKouchak, A. (2020). Global snow drought hot spots and characteristics. *Proceedings of the National Academy of Sciences*, *117*(33), 19753. https://doi.org/10.1073/pnas.1915921117

Immerzeel, W. W., Lutz, A. F., Andrade, M., Bahl, A., Biemans, H., Bolch, T., Hyde, S., Brumby, S., Davies, B. J., Elmore, A. C., Emmer, A., Feng, M., Fernández, A., Haritashya, U., Kargel, J. S., Koppes, M., Kraaijenbrink, P. D. A., Kulkarni, A. V., Mayewski, P. A., … Baillie, J. E. M. (2020). Importance and vulnerability of the world's water towers. *Nature*, *577*(7790), 364–369. https://doi.org/10.1038/s41586-019-1822-y

Khanal, S., Lutz, A. F., Kraaijenbrink, P. D. A., van den Hurk, B., Yao, T., & Immerzeel, W. W. (2021). Variable 21st Century Climate Change Response for Rivers in High Mountain Asia at Seasonal to Decadal Time Scales. *Water Resources Research*, *57*(5), e2020WR029266. https://doi.org/10.1029/2020WR029266

Kim, R. S., Kumar, S., Vuyovich, C., Houser, P., Lundquist, J., Mudryk, L., Durand, M., Barros, A., Kim, E. J., Forman, B. A., Gutmann, E. D., Wrzesien, M. L., Garnaud, C., Sandells, M., Marshall, H.-P., Cristea, N., Pflug, J. M., Johnston, J., Cao, Y., … Wang, S. (2021). Snow Ensemble Uncertainty Project (SEUP): Quantification of snow water equivalent

uncertainty across North America via ensemble land surface modeling. *The Cryosphere*, *15*(2), 771–791. https://doi.org/10.5194/tc-15-771-2021

KOBAYASHI, S., OTA, Y., HARADA, Y., EBITA, A., MORIYA, M., ONODA, H., ONOGI, K., KAMAHORI, H., KOBAYASHI, C., ENDO, H., MIYAOKA, K., & TAKAHASHI, K. (2015). The JRA-55 Reanalysis: General Specifications and Basic Characteristics. *Journal of the Meteorological Society of Japan. Ser. II*, *93*(1), 5–48. https://doi.org/10.2151/jmsj.2015-001

Kraaijenbrink, P. D. A., Stigter, E. E., Yao, T., & Immerzeel, W. W. (2021). Climate change decisive for Asia's snow meltwater supply. *Nature Climate Change*, *11*(7), 591–597. https://doi.org/10.1038/s41558-021-01074-x

Lehner, B., Verdin, K., & Jarvis, A. (2008). New Global Hydrography Derived From Spaceborne Elevation Data. *Eos, Transactions American Geophysical Union*, *89*(10), 93–94. https://doi.org/10.1029/2008EO100001

Liston, G. E. (2004). Representing Subgrid Snow Cover Heterogeneities in Regional and Global Models. *Journal of Climate*, *17*(6), 1381–1397. https://doi.org/10.1175/1520-0442(2004)017<1381:RSSCHI>2.0.CO;2

Liston, G. E., & Elder, K. (2006). A Distributed Snow-Evolution Modeling System (SnowModel). *Journal of Hydrometeorology*, *7*(6), 1259–1276. https://doi.org/10.1175/JHM548.1

Liu, Y., & Margulis, S. A. (2019). Deriving Bias and Uncertainty in MERRA-2 Snowfall Precipitation Over High Mountain Asia. *Frontiers in Earth Science*, *7*, 280. https://doi.org/10.3389/feart.2019.00280

Liu, Y., Fang, Y., & Margulis, S. A. (2021). High Mountain Asia UCLA Daily Snow Reanalysis, Version 1. Boulder, Colorado USA. NASA National Snow and Ice Data Center Distributed Active Archive Center. doi: https://doi.org/10.5067/HNAUGJQXSCVU.

Liu, Y., Fang, Y., & Margulis, S. A. (2021). Spatiotemporal distribution of seasonal snow water equivalent in High Mountain Asia from an 18-year \hack\break Landsat–MODIS era snow reanalysis dataset. *The Cryosphere*, *15*(11), 5261–5280. https://doi.org/10.5194/tc-15-5261-2021

Mankin, J. S., Viviroli, D., Singh, D., Hoekstra, A. Y., & Diffenbaugh, N. S. (2015). The potential for snow to supply human water demand in the present and future. *Environmental Research Letters*, *10*(11), 114016. https://doi.org/10.1088/1748-9326/10/11/114016

Margulis, S. A., Liu, Y., & Baldo, E. (2019). A Joint Landsat- and MODIS-Based Reanalysis Approach for Midlatitude Montane Seasonal Snow Characterization. *Frontiers in Earth Science*, *7*, 272. https://doi.org/10.3389/feart.2019.00272

McCrary, R. R., & Mearns, L. O. (2019). Quantifying and Diagnosing Sources of Uncertainty in Midcentury Changes in North American Snowpack from NARCCAP. *Journal of Hydrometeorology*, *20*(11), 2229–2252. https://doi.org/10.1175/JHM-D-18-0248.1

Mortimer, C., Mudryk, L., Derksen, C., Luojus, K., Brown, R., Kelly, R., & Tedesco, M. (2020). Evaluation of long-term Northern Hemisphere snow water equivalent products. *The Cryosphere*, *14*(5), 1579–1594. https://doi.org/10.5194/tc-14-1579-2020

Mudryk, L. R., Derksen, C., Kushner, P. J., & Brown, R. (2015). Characterization of Northern Hemisphere Snow Water Equivalent Datasets, 1981–2010. *Journal of Climate*, *28*(20), 8037–8051. https://doi.org/10.1175/JCLI-D-15-0229.1

Muñoz-Sabater, J., Dutra, E., Agustí-Panareda, A., Albergel, C., Arduini, G., Balsamo, G., Boussetta, S., Choulga, M., Harrigan, S., Hersbach, H., Martens, B., Miralles, D. G., Piles, M., Rodríguez-Fernández, N. J., Zsoter, E., Buontempo, C., & Thépaut, J.-N. (2021). ERA5-Land: A state-of-the-art global reanalysis dataset for land applications. *Earth System Science Data*, *13*(9), 4349–4383. https://doi.org/10.5194/essd-13-4349-2021

ONOGI, K., TSUTSUI, J., KOIDE, H., SAKAMOTO, M., KOBAYASHI, S., HATSUSHIKA, H., MATSUMOTO, T., YAMAZAKI, N., KAMAHORI, H., TAKAHASHI, K., KADOKURA, S., WADA, K., KATO, K., OYAMA, R., OSE, T., MANNOJI, N., & TAIRA, R. (2007). The JRA-25 Reanalysis. *気象集誌. 第 2 輯*, *85*(3), 369–432. https://doi.org/10.2151/jmsj.85.369

Orsolini, Y., Wegmann, M., Dutra, E., Liu, B., Balsamo, G., Yang, K., de Rosnay, P., Zhu, C., Wang, W., Senan, R., & Arduini, G. (2019). Evaluation of snow depth and snow cover over the Tibetan Plateau in global reanalyses using in situ and satellite remote sensing observations. *The Cryosphere*, *13*(8), 2221–2239. https://doi.org/10.5194/tc-13-2221-2019

Painter, T. H., Rittger, K., McKenzie, C., Slaughter, P., Davis, R. E., & Dozier, J. (2009). Retrieval of subpixel snow covered area, grain size, and albedo from MODIS. *Remote Sensing of Environment*, *113*(4), 868–879. https://doi.org/10.1016/j.rse.2009.01.001

Palazzi, E., von Hardenberg, J., & Provenzale, A. (2013). Precipitation in the Hindu-Kush Karakoram Himalaya: Observations and future scenarios. *Journal of Geophysical Research: Atmospheres*, *118*(1), 85–100. https://doi.org/10.1029/2012JD018697

Qin, Y., Abatzoglou, J. T., Siebert, S., Huning, L. S., AghaKouchak, A., Mankin, J. S., Hong, C., Tong, D., Davis, S. J., & Mueller, N. D. (2020). Agricultural risks from changing snowmelt. *Nature Climate Change*, *10*(5), 459–465. https://doi.org/10.1038/s41558-020-0746-8

Reichle, R. H., Draper, C. S., Liu, Q., Girotto, M., Mahanama, S. P. P., Koster, R. D., & De Lannoy, G. J. M. (2017). Assessment of MERRA-2 Land Surface Hydrology Estimates. *Journal of Climate*, *30*(8), 2937–2960. https://doi.org/10.1175/JCLI-D-16-0720.1

Rodell, M., Houser, P. R., Jambor, U., Gottschalck, J., Mitchell, K., Meng, C.-J., Arsenault, K., Cosgrove, B., Radakovich, J., Bosilovich, M., Entin, J. K., Walker, J. P., Lohmann, D., & Toll, D. (2004). The Global Land Data Assimilation System. *Bulletin of the American Meteorological Society*, *85*(3), 381–394. https://doi.org/10.1175/BAMS-85-3-381

Stigter, E. E., Litt, M., Steiner, J. F., Bonekamp, P. N. J., Shea, J. M., Bierkens, M. F. P., & Immerzeel, W. W. (2018). The Importance of Snow Sublimation on a Himalayan Glacier. *Frontiers in Earth Science*, *6*. https://www.frontiersin.org/article/10.3389/feart.2018.00108

Sun, S., & Xue, Y. (2001). Implementing a new snow scheme in Simplified Simple Biosphere Model. *Advances in Atmospheric Sciences*, *18*(3), 335–354. https://doi.org/10.1007/BF02919314

Terzago, S., von Hardenberg, J., Palazzi, E., & Provenzale, A. (2014). Snowpack Changes in the Hindu Kush–Karakoram–Himalaya from CMIP5 Global Climate Models. *Journal of Hydrometeorology*, *15*(6), 2293–2313. https://doi.org/10.1175/JHM-D-13-0196.1

Viviroli, D., Dürr, H. H., Messerli, B., Meybeck, M., & Weingartner, R. (2007). Mountains of the world, water towers for humanity: Typology, mapping, and global significance. *Water Resources Research*, *43*(7). https://doi.org/10.1029/2006WR005653

Wang, X., Tolksdorf, V., Otto, M., & Scherer, D. (2021). WRF-based dynamical downscaling of ERA5 reanalysis data for High Mountain Asia: Towards a new version of the High Asia

Refined analysis. *International Journal of Climatology*, *41*(1), 743–762. https://doi.org/10.1002/joc.6686

Wrzesien, M. L., Pavelsky, T. M., Durand, M. T., Dozier, J., & Lundquist, J. D. (2019). Characterizing Biases in Mountain Snow Accumulation From Global Data Sets. *Water Resources Research*, *55*(11), 9873–9891. https://doi.org/10.1029/2019WR025350

Xiao, L., Che, T., & Dai, L. (2020). Evaluation of Remote Sensing and Reanalysis Snow Depth Datasets over the Northern Hemisphere during 1980–2016. *Remote Sensing*, *12*(19). https://doi.org/10.3390/rs12193253

Xiao, M., Mahanama, S. P., Xue, Y., Chen, F., & Lettenmaier, D. P. (2021). Modeling Snow Ablation over the Mountains of the Western United States: Patterns and Controlling Factors. *Journal of Hydrometeorology*, *22*(2), 297–311. https://doi.org/10.1175/JHM-D-19-0198.1

Xu, Y., Jones, A., & Rhoades, A. (2019). A quantitative method to decompose SWE differences between regional climate models and reanalysis datasets. *Scientific Reports*, *9*(1), 16520. https://doi.org/10.1038/s41598-019-52880-5

Xue, Y., Sun, S., Kahan, D., & Jiao, Y. (2003). Impact of parameterizations in snow physics and interface processes on the simulation of snow cover and runoff at several cold region sites. *Journal of Geophysical Research*, *108*. https://doi.org/10.1029/2002JD003174

Yao, T., Thompson, L., Yang, W., Yu, W., Gao, Y., Guo, X., Yang, X., Duan, K., Zhao, H., Xu, B., Pu, J., Lu, A., Xiang, Y., Kattel, D. B., & Joswiak, D. (2012). Different glacier status with atmospheric circulations in Tibetan Plateau and surroundings. *Nature Climate Change*, *2*(9), 663–667. https://doi.org/10.1038/nclimate1580

CHAPTER 5

Conclusions

5.1 Summary and original contributions:

Using a newly developed snow reanalysis method and a novel HMASR dataset, the spatiotemporal distribution in seasonal snowpack and its snow storage are examined in this dissertation.

The bias and uncertainties in snowfall precipitation from existing datasets (e.g. MERRA2) are first evaluated in Chapter 2, with the key conclusions summarized as below:

1) The results indicate that snowfall precipitation is underestimated in most precipitation products (e.g. by ~50% in MERRA2) with sizable uncertainty.
2) The biases are higher in the gauge-based precipitation product (e.g. ~234% in APHRODITE2).
3) This study shows the potential for using satellite snow observations as a constraint on models to infer biases and uncertainties in snowfall precipitation in remote regions and complex terrain where in-situ stations are very scarce.

The uncertainty parameters derived in Chapter 2 are applied as a priori information in the development of HMASR dataset. Through analyzing the dataset, the spatiotemporal distribution in seasonal snowpack and its snow storage are quantified in Chapter 3, with the key conclusions as:

1) Peak seasonal SWE is most abundant in the western HMA and occurs with a median date of March 18th across the domain.
2) The peak seasonal snow storage is quantified as 163 km^3 when aggregated across the full HMA domain and averaged across WYs 2000-2017, with notable interannual variations between 114 km^3 and 227 km^3.

3) Peak snow storage is found most abundant at mid elevations (3000 – 4000 m), and over 50% of this storage is found above 3500 m on average, with variations under different climate conditions.

The HMASR datasets facilitates a thorough evaluation of existing global snow products over HMA as described in detail in Chapter 4. With the focus on accumulation season processes leading to the (pixel-wise) peak snow storage, the conclusions are:

1) The climatology in (pixel-wise) peak snow storage was found to be 161 km3 $\pm$ 102 km3 within the global snow products, with varying uncertainty levels for seasonal (110 km3 $\pm$ 74 km3) vs. intermittent (51 km3 $\pm$ 28 km3) snow regimes. Compared to HMASR, the other snow products on average underestimate peak snow storage by 33% $\pm$ 52% over the entire HMA.
2) Overall, there exist large variabilities in cumulative snowfall and ablation over the accumulation season. The accumulation snowfall climatology is found as 335 km3 $\pm$ 148 km3, and the cumulative snowfall loss into ablation is found as 51% $\pm$ 9% over HMA (with variations as 37% $\pm$ 13% in seasonal snow regimes, and as 67% $\pm$ 7% in intermittent snow regimes).
3) Uncertainty in peak snow storage estimates is primarily explained by accumulation season snowfall (88%) over HMA, partly due to a wide range (uncertainty) in precipitation (snowfall). Accumulation season ablation is found to explain more uncertainty in peak snow storage when the snowfall uncertainty was reduced by considering subsets of snow products.

5.2 Potential for future work.

The potential areas for future work are listed as follows:

Regarding snowfall in HMA:

1) Snowfall precipitation is a key input in snow modeling and a significant source of uncertainty. The current HMASR dataset did not output snowfall but can be provided in future versions for a thorough evaluation over this region.
2) The posterior scaling factors for snowfall precipitation is generated as a by-product of the snow reanalysis. Its climatology and variations under different climate or physiographic conditions can be further investigated over this region to guide future versions of the reanalysis.

Regarding snow data assimilation in HMA:

1) The quantity and quality of assimilated fSCA measurements are highly sensitive to cloud cover, especially over the monsoon areas in HMA. Future work should investigate the potential of assimilating other remote-sensing measurements (e.g. from active microwave that can penetrate clouds) in reducing the uncertainties for SWE estimation over those areas.
2) The current snow reanalysis scheme used in this dissertation is particularly designed for estimating seasonal snow (with a clear signal of snow accumulation and depletion observed in fSCA). The method is less well suited to estimating intermittent snow (only lasting within a short period). Future versions can investigate how to improve the characterization of intermittent snow using the existing snow reanalysis framework.

Regarding snow modeling in HMA:

1) Both accumulation season snowfall and ablation affect uncertainty in peak snow storage. To reduce the uncertainty in peak snow storage over HMA, improved characterization in both snowfall and ablation processes are needed. More specifically, the large variation (uncertainty) seen in existing snow products over HMA points out the urgent need of reducing snowfall uncertainties in this region.
2) The main drivers for snow ablation variability during the accumulation season are not explored in this work but can be investigated in future work. To be more specific, sensitivity tests for the key variables affecting ablation (e.g. air temperature, wind speed, radiation, etc.) can be performed to evaluate the relative importance on accumulation season ablation. Or using the same set of meteorological forcing but altering the land surface model to evaluate their impact on accumulation season processes.

Regarding the impact of snowpack in the regional water cycle and climate in HMA:

1) The derived HMASR datasets provides quantified seasonal snow storage constrained by satellite remote sensing, which offers the potential of evaluating the role of seasonal snowpack in regional hydrology. For example, both the timing and magnitude of snowmelt can be assessed to identify the relative contribution to total runoff.
2) The response of seasonal snowpack to climate variability has not been explored in this work, due to the short length of the dataset (18 Water Years). Future work may extend the dataset for a more thorough evaluation on this topic.